Spring 1-1-2013

Numerical Modeling and Optimization of Mechanically Active Electrochemical Systems

Christopher Michael DeLuca
University of Colorado at Boulder, delucac@colorado.edu

Numerical Modeling and Optimization of Mechanically Active Electrochemical Systems

by

Christopher DeLuca

BA, Mathematics

BS, Mechanical Engineering

University of Colorado at Boulder, 2008

MS, Mechanical Engineering

University of Colorado at Boulder, 2009

A thesis submitted to the

Faculty of the Graduate School of the

University of Colorado Department of Aerospace Engineering

2013

This thesis entitled:
Numerical Modeling and Optimization of Mechanically Active Electrochemical Systems
written by Christopher DeLuca
has been approved for the Department of Aerospace Engineering

Dr. Kurt Maute

Dr. Carlos Felippa

Date

This thesis has been examined by the signatories, and we find that both the content and the form meet acceptable presentation standards of scholarly work in the above mentioned discipline.

DeLuca, Christopher

Numerical Modeling and Optimization of Mechanically Active Electrochemical Systems

Supervised by Dr. Kurt Maute and Dr. Carlos Felippa

This work is primarily motivated by the hope that Silicon (Si) can be utilized in Lithium (Li) ion batteries to enable an order of magnitude capacity increase if Li-Si systems can be better understood. In order to create a valuable tool that could be used to study a wide range of problem, pertinent physical models were implemented in an extended finite element method (XFEM) framework written in c++. One of the major contribution of this work goes to the battery modeling community, by generalizing several existing electrochemical-mechanical models which use a small deformation approximations so they can accommodate finite deformation. A general theory which can be used to guide the development of new finite element models is presented in detail. This work also contributes new finite element modeling tools with novel predictive capabilities to the battery modeling community, which will hopefully facilitate the design and optimization of next generation battery micro-structures. Studies within demonstrate that small deformation approximation models can produce incorrect predictions about the behavior of Li-Si systems, supporting the case for using finite deformation models. The developed tools are used to demonstrate that arbitrary geometries can easily be simulated on a the same fixed grid, facilitating automated geometry studies including parameter sweeping and topology optimization.

Acknowledgements

Thanks to the Department of Aerospace Engineering Sciences, University of Colorado, Boulder, for selecting me for a GAANN fellowship and to the U.S. Department of Education for funding the program. Thanks for the support from the Air Force Office of Scientific Research MURI; contract/grant number: F9550-06-1-0326. The opinions and conclusions presented in this thesis are those of the author and do not necessarily reflect the views of the sponsoring organizations. Thanks to my advisor Professor Kurt Maute for all his insight, patience, and support. Thanks to all of the past and current members of the CAS for all of their support and good beer. I like beer. Thanks to Ann Brookover, the Aerospace Engineering Sciences Graduate Advisor, for all the help with my transfer into the department and with the GAANN application process, and thanks to the Graduate committee for making my transfer as smooth as possible. Thanks for all the support from the faculty and staff in the Mechanical Engineering department during six of the twelve years I spent studying at CU. Thanks to Dr. Victor Bright for providing me with the opportunity to join the Graduate Engineering program and providing support through my first couple years in the program. Thanks to Dr. Bradley Darren Davidson for all the encouragement and help during my extended stay at the University of Colorado, Boulder. Thanks to all my family and friends for believing in me. Thanks to my wonderful girlfriend for all of her love and support through this strenuous process. Finally, thanks to Dr. Martin L. Dunn, Dr. Carlos Felippa, Dr. Alireza Doostan, and Dr. Se-Hee Lee for being on my committee.

Contents

Chapter

Tables

Table

Figures

Figure

Chapter 1

Introduction

1.1 Motivation

In the world markets there is an ever increasing demand for higher capacity batteries. This is due to the proliferation of portable electronic devices, such as cell phones, laptops, iPods, electric cars, and toys to name a few. In order to facilitate the development of higher energy density batteries, the physics involved in charging/discharging batteries must be well understood. The scientific community has been developing and using electrochemical models to understand and predict the behavior of battery systems for decades, but mechanical effects have only been seriously considered in the last ten years. Linear elasticity has since been employed in numerous studies in efforts to understand the mechanisms that cause capacity fade and electrode particle fracture. However, for systems that experience large deformations (e.g. $\mathrm{Li}_x\mathrm{Si}y$ systems), linear elasticity cannot adequately model the mechanics. Instead finite deformation models must be used. Recently a few finite deformation models have been published for use in simulating electrode particles [61], dielectrics [49], and full lithium ion half cells [9]. Due to the promise of better battery performance and the increasing sophistication and availability of micro-fabrication techniques, micro-structured electrodes are receiving an increasing amount of attention in both numerical studies [20, 19, 57, 56, 55] as well as experimental studies [10, 46, 35, 37, 53].

In order to characterize and better understand the behavior of micro-structured

electrodes, highly coupled mechanics-transport models have been developed and implemented in a finite element framework. A small deformation diffusive transport model coupled with a linear elastic mechanics model with swelling was employed to study the influence of electrode particle morphology on stress generation during insertion/extraction [22]. The study provided some interesting insight into how electrode particle sizes can influence the mechanical behavior of battery electrodes during operation, but the study concluded that more sophisticated tools are needed to facilitate accurate and efficient studies on optimal electrode particle shapes. It was decided that the small deformation approximations should not be used because our primary interest was in modeling Li-Si systems which are known to experience significant swelling. In order to facilitate automated geometry studies such as topology optimization new finite element models were wrapped into an extended finite element method (XFEM) framework.

The primary goal of the of this work was to develop more accurate and versatile modeling tools which can be used by both designers and scientists to efficiently determine optimal electrode designs and develop more intuitive understandings into the behaviors of batteries and other electrochemical systems during operation. Most previous modeling work either neglected deformation effects or assumed small deformation to simplify model development and implementation. Small deformation approximations are inadequate for our needs, so we chose to generalize previous models to accommodate finite deformation effects. However, other complicated mechanical behaviors such as fracture and plasticity were ignored.

With standard finite element methods (FEM) it is difficult to study varying geometries because body fitted meshes must be used. Mesh generation usually requires user input, so geometry studies must be performed manually. In cases when little in known about geometric effects, attempts to identify optimal geometries can be very time consuming and often inconclusive as was demonstrated in [22]. To remove the

requirement for having body fitted meshes it was decided to implement various electrochemical models in an XFEM framework. In our XFEM implementation arbitrary geometries can be modeled on a fixed grid, removing the need for body fitted meshes or sophisticated meshing software. With finite deformation electrochemical models implemented in a three dimensional XFEM framework a very powerful tool for modeling batteries and electrochemical systems has been created.

1.2 Document Organization

Chapter 2 is concerned with developing models to facilitate simulations of electrochemical mechanical systems. The phenomena experienced by typical batteries during operation are discussed, followed by detailed presentations of the mathematical models used to describe the pertinent physics involved in battery operation. First governing equations for the various systems of interest are detailed in Section 2.1. Constitutive relations are described in the following Section 2.2. The chapter is concluded with a section discussing which governing and constitutive relations should be paired in order to simulate the various systems of interest.

The following chapter, 3, describes the finite element models that have been implemented. In our implementation a physical model is a pairing of an "element" with a "material". "Elements" are responsible for evaluating gauss point state variables, their spatial gradients, and the derivatives of gauss point state variables and their spatial gradients with respect to nodal variables. "Elements" are also responsible for integrating state equations. "Materials" are responsible for evaluating constitutive relations provided with gauss point state quantities computed by an "element". Such a modular setup facilitates the use of various different constitutive relations with the same element just by switching the "material". The "elements" described in Section 3.1 are presented in terms of the quantities they are responsible for computing and the weak forms of the state equations they are responsible for integrating. The "materials" described in

Section 3.1 are responsible for evaluating constitutive relations and their derivatives with respect to nodal state variables.

Chapter 4 is focused on addressing geometric considerations in our model development. Geometric assumptions that can be made to reduce the complexity are discussed in Section 4.1. Then there is a discussion on the methods used for satisfying interface conditions in our XFEM formulation in Section 5.3. The complete details of our XFEM implementation are discussed in [36] and will not be discussed within.

After detail discussions of model development and implementation Chapter 5 discusses efforts that have been made to verify the implementations. The first section (5.1) is concerned with verifying the small deformation formulations. Next a number of finite deformation model verification studies are presented in Section 5.2. In the final Section 5.3 XFEM verification studies are presented.

In Chapter 6 the implemented models are employed to investigate the behavior of Li-Si systems. Section 6.1 compares results generated with the small deformation models with equivalent results generated with the finite deformation models. The chapter is concluded with a presentation of novel XFEM simulation results (6.2).

A significant amount of work has been done to develop new modeling capabilities and help advance the field of electrochemical-mechanical modeling, but a significant ammount of work remains to be done by future researchers. Chapter 7 is concerned with wrapping up the document. Section 7.1 focuses on some work that could be done as a direct extension of the work documented within. Then the discussion portion of the document ends with a short presentation of some conclusions that can be drawn from the work completed in Section 7.2.

The appendix is broken up into four sections. The first Section (8.1) lists some useful transformation rules. The next section (8.2) lists the various non-linear elastic constitutive models that have been implemented in our finite element code. The following section (8.3) lists the various chemical potential functions that have been im-

plemented in our finite element code. Finally the last section (8.4) in the paper has tables defining all symbols used within.

Chapter 2

Modeling Electrochemical Mechanical Systems

Electrochemistry can be used to describe a wide variety of physical systems and devices. Everything from corrosion of metals in oxygen rich environments, to fuel cells can, at least in part, be characterized by electrochemistry. Species diffusion and mechanics have been studied in many different contexts for decades, but coupled analyses for electrochemical insertion electrodes has only recently become prevalent [18, 17, 60, 59, 27, 29, 11, 13, 12, 23, 9, 61]. The development of the models presented within was motivated by a need to characterize electrochemistry and mechanics involved in lithium ion battery technologies, most notably silicon lithium systems because of the significant deformation experienced by silicon during lithium insertion. Typical batteries are composed of five different regions: a positive current collector, a cathode region, a separator region, an anode region, and a negative current collector. In typical cylindrical batteries, e.g. AAs, the five regions are constructed as films then laid together and rolled up. The construction of the five regions is referred to as a cell. Figure 2.1 depicts a cell.

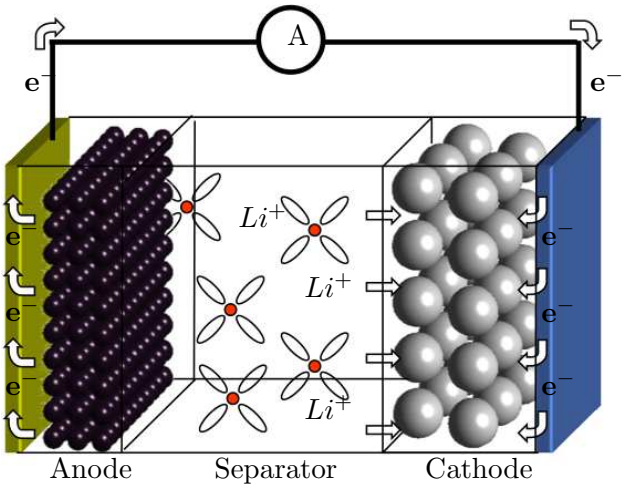

Figure 2.1: Cell layout [28]

The positive and negative current collectors are represented by the blue and green plates on either side of the construction respectively. The current collectors only transport electrons, and can be adequately modeled with boundary conditions at the anode and cathode current collector interfaces. The electrodes are typically a mix of species transport material and an electrically conductive binder material impregnated by an electrolyte material. In the following discussions the combination of the species transport material and the conductive binder material are referred to as electrode particle material. The separator region is often purely comprised of a single electrolyte material.

The discharge of a cell can be described as follows. The two electrodes are at different potentials when saturated with the transport species. At the beginning of the discharge cycle all of the transport species is contained in the Anode at lower electric potential than the empty Cathode. By making an electrical contact between the electrodes, electrons are allowed to travel through the external circuit to the cathode. The removal of electrons from the Anode causes an oxidation reaction to occur at the anode electrolyte interface, releasing ions into the electrolyte. The ions then diffuse through the separator to the Cathode electrolyte interface. Similarly to the Anode, the addition of electrons to the Cathode causes a reduction reaction at the Cathode

electrolyte interface, creating a neutral species at the interface. The redox reactions result in concentration gradients of the transport species at the electrolyte interfaces of the electrodes, which trigger diffusion of the transport species through the electrode particles. To charge a cell an electric potential is applied across the electrodes reversing the whole process.

The whole process involves three different types of physical phenomena: species/ion transport, electrochemical reactions, and mechanical deformation. The transport phenomena include transport of a neutral species through the electrode particles, transport of ions through the electrolyte, and transport of electrons through the electrode particles. Both the species and ion transport phenomena are treated as diffusive process but the potentials that drive them are quite different. It is assumed that the electrons move much faster than the diffusing species, so electron transport is modeled with electrostatics. To simplify the full model of a cell it is assumed that the only reactions that occur during discharging are the redox reaction mentioned in the previous paragraph. Although it is know that other side reactions do occur [41, 4], we neglect them in the studies presented within. Although mechanics can play a significant role in the behavior of batteries, it is frequently ignored or greatly simplified by in modeling efforts. Electrode particles are known to swell, some by as much as 300% [10, 4], as they absorb transport species. It is assumed that the mechanical response to the swelling is much faster than diffusion, so the various regions of an electrode are assumed to always be in a state of static equilibrium.

In the following sections models for each of the above physical phenomena are presented. First governing equations are presented for the different classes of physical systems in Section 2.1. Then constitutive relations are developed for various different uncoupled and coupled chemical-mechanical systems in Section 2.2. In the final section of this chapter (2.3) there is discussion on how to use the governing and constitutive relations together to model the coupled transport-mechanics phenomena in the electrode

host and electrolyte regions.

2.1 Governing Equations

The governing equations for the four different physical phenomena of interest are developed in this section. First the governing equations for mechanical equilibrium are discussed, because mechanical deformation is an important consideration in the following sections. Governing equations for diffusive transport are presented in the next section (2.1.2). Then, the governing equations for electrostatics are presented (2.1.3). The final subsection (2.1.4) a model for the redox reactions which occur at the electrode-electrolyte is discussed.

2.1.1 Mechanical Equilibrium

It is assumed that the mechanical response is much faster than species transport. We can, therefore, neglect inertia and damping, and use a force balance to model the mechanics. Mechanical equilibrium expressed with Newton's second law in a continuum is

$$\nabla \cdot \boldsymbol{\sigma} = 0 \tag{2.1}$$

where $\boldsymbol{\sigma}$ is the true, or cauchy, stress tensor, and ∇ is the gradient operator with respect to the deformed body. In a three dimensional cartesian coordinate system the gradient operator is written as

$$\nabla = \hat{\mathbf{i}}\frac{\partial}{\partial \mathrm{x}} + \hat{\mathbf{j}}\frac{\partial}{\partial \mathrm{y}} + \hat{\mathbf{k}}\frac{\partial}{\partial \mathrm{z}} \tag{2.2}$$

$\hat{\mathbf{i}}$, $\hat{\mathbf{j}}$, and $\hat{\mathbf{k}}$ are the unit basis vectors in the Cartesian coordinate frame.

Equation (2.1) represents mechanical equilibrium in the current deformed reference frame. While Equation (2.1) is a nice compact way to represent the force balance in a continuum, in practice the force balance is usually transformed to the undeformed reference configuration when finite deformation is a concern. Integrating over the de-

formed body and applying the divergence theorem

$$\int_{\Omega} \nabla \cdot \boldsymbol{\sigma} d\Omega = \int_{\Gamma} \boldsymbol{\sigma} \cdot \mathbf{n} d\Gamma \tag{2.3}$$

The following integral transformation is used to transform the surface integral in Equation (2.3) into an integral with respect the undeformed body [8]

$$\mathbf{n} d\Gamma = J \mathbf{F}^{-T} \mathbf{n}_0 d\Gamma_0 \tag{2.4}$$

where Γ and $\mathbf{n}$ represent the surface and it's normal in the deformed configuration, Γ_0 and $\mathbf{n_0}$ represent the surface and it's normal in the reference configuration, $\mathbf{F}$ is the deformation gradient, and J is the determinant of $\mathbf{F}$. The deformation gradient is defined as

$$\mathbf{F} = \frac{\partial \mathbf{x}}{\partial \mathbf{X}} = \frac{\partial \mathrm{x}_i}{\partial \mathrm{X}_j} = \mathrm{F}_{ij} \tag{2.5}$$

$\mathbf{x}$ is the coordinate vector in the deformed frame and $\mathbf{X}$ is the coordinate vector in the undeformed frame. The second equality represents $\mathbf{F}$ in index notation but is only valid for Cartesian coordinate frames where $\mathbf{x}$ and $\mathbf{X}$ have the following definitions.

$$\mathbf{x} = \begin{bmatrix} \mathrm{x} \\ \mathrm{y} \\ \mathrm{z} \end{bmatrix} \quad \mathbf{X} = \begin{bmatrix} \mathrm{X} \\ \mathrm{Y} \\ \mathrm{Z} \end{bmatrix} \tag{2.6}$$

Applying the surface integral transformation rule (2.4)

$$\int_{\Gamma} \boldsymbol{\sigma} \cdot \mathbf{n} d\Gamma = \int_{\Gamma_0} J \boldsymbol{\sigma} \mathbf{F}^{-T} \cdot \mathbf{n}_0 d\Gamma_0 = \int_{\Gamma_0} \mathbf{P} \cdot \mathbf{n}_0 d\Gamma_0 \tag{2.7}$$

where $\mathbf{P}$ in called the nominal stress tensor. Applying the divergence theorem to get to a volume integral with respect to the undeformed body

$$\int_{\Gamma_0} \mathbf{P} \cdot \mathbf{n}_0 d\Gamma_0 = \int_{\Omega_0} \nabla^0 \cdot \mathbf{P} d\Omega_0 \tag{2.8}$$

the force balance with respect to the undeformed body can be written as

$$\nabla^0 \cdot \mathbf{P} = \mathbf{0} \tag{2.9}$$

∇^0 is the gradient operator with respect to the undeformed body. In a three dimensional cartesian coordinate system this gradient operator is written as

$$\nabla^0 = \hat{\mathbf{i}}\frac{\partial}{\partial \mathrm{X}} + \hat{\mathbf{j}}\frac{\partial}{\partial \mathrm{Y}} + \hat{\mathbf{k}}\frac{\partial}{\partial \mathrm{Z}} \tag{2.10}$$

Using the above definition of ∇^0 and the relation between coordinates in the deformed and undeformed frames ($\mathbf{x} = \mathbf{u} + \mathbf{X}$), the deformation gradient can be written as

$$\mathbf{F} = \frac{\partial \mathbf{u}}{\partial \mathbf{X}} + \frac{\partial \mathbf{X}}{\partial \mathbf{X}} = \nabla^0 \mathbf{u} + \mathbf{I} = \mathbf{H} + \mathbf{I} \tag{2.11}$$

where $\mathbf{u}$ is the displacement vector, $\mathbf{H}$ is called the displacement gradient, and $\mathbf{I}$ is the second order identity tensor.

In Belytchko's works the mechanical equilibrium in the reference configuration is written as

$$\nabla^0 \cdot \mathbf{P_B^T} = \mathbf{0} \tag{2.12}$$

where $\mathbf{P_B}$ is the nominal stress tensor defined by Belytchko as

$$\mathbf{P}_B = J\mathbf{F}^{-1}\boldsymbol{\sigma} \tag{2.13}$$

but in the works within the nominal stress is defined as

$$\mathbf{P} = J\boldsymbol{\sigma}\mathbf{F}^{-T} = J\mathbf{F}^{-1}\boldsymbol{\sigma}^T = J\mathbf{F}^{-1}\boldsymbol{\sigma} = \mathbf{P}_B^T \tag{2.14}$$

The third equality results from the symmetry in the Cauchy stress tensor. Our formulation is therefore consistent with Belytchko et al. [8]. We adopted the above definition of the nominal stress tensor because it simplifies some of the following derivation and it is consistent with other relevant works [33, 58, 34]. In the case of small deformation all stress measures are nearly equivalent and $\nabla \approx \nabla^0$. Therefore, in the case of small deformation we can write.

$$\nabla \cdot \boldsymbol{\sigma} \approx \nabla^0 \cdot \mathbf{P} \tag{2.15}$$

Constitutive relation for stresses will be discussed in Section2.2.

2.1.2 Diffusive Transport

The governing equations for diffusion are based on conservation of mass. The mass balance in the deformed volume of an electrode particle is written as

$$\frac{\partial c}{\partial t} + \nabla \cdot \mathbf{j} = \dot{c} + \nabla \cdot \mathbf{j} = r \tag{2.16}$$

c is the true species concentration, $\mathbf{j}$ is the true flux, and r is a sink/source term. Equation (2.16) states that the rate of accumulation of material in a volume must be balanced by flux of material into the volume. The most general equation for species flux is

$$\mathbf{j} = c\mathbf{v} \tag{2.17}$$

where $\mathbf{v}$ is the velocity of the transport species. In diffusive transport processes the species velocity is a function of the gradient of chemical potential. Diffusive flux is expressed with Equation (2.18) [5, 40].

$$\mathbf{j} = -\frac{cD}{R_g T}\nabla\mu_c = -cM\nabla\mu_c \tag{2.18}$$

where $M = \frac{D}{R_g T}$ is the species mobility. Therefore, the species velocity is

$$\mathbf{v} = -M\nabla\mu_c \tag{2.19}$$

When considering finite deformation mechanics as well as diffusive transport, it is advantageous to express concentrations and fluxes in terms of their nominal quantities, so all of the governing equations can be integrated over the un-deformed frame. The following expressions relate nominal concentration (C), species flux ($\mathbf{J}$), and gradient operator (∇^0) to the true concentration (c), species flux ($\mathbf{j}$), and gradient operator (∇) [30].

$$C = Jc \tag{2.20}$$

$$\mathbf{J} = J\mathbf{F}^{-1}\mathbf{j} \tag{2.21}$$

$$\nabla^0 = \mathbf{F}^T \nabla \tag{2.22}$$

Substituting Equations (2.18), (2.20), and (2.22) into Equation (2.21) we arrive at the following equation for nominal species flux.

$$\mathbf{J} = -\frac{CD}{R_g T}\mathbf{F}^{-1}\mathbf{F}^{-T}\nabla^0\mu_c = -\frac{CD}{R_g T}\mathbf{C}^{-1}\nabla^0\mu_c = -C\mathbf{M}\nabla^0\mu_c \tag{2.23}$$

where $\mathbf{C} = \mathbf{F^T F}$ is the right Cauchy-Green deformation tensor, and $\mathbf{M} = \mathbf{C}^{-1}\frac{D}{R_g T}$ is the species nominal mobility tensor. The last equality in the expression matches the form derived by Gurtin et al. [30] in his thermodynamic treatment of species transport in chapter 66. The governing equations in the reference configuration look identical to their counterpart in the deformed configuration with the distinct difference that the concentration and flux are nominal quantities.

$$\frac{\partial C}{\partial t} + \nabla^0 \cdot \mathbf{J} = \dot{C} + \nabla^0 \cdot \mathbf{J} = 0 \tag{2.24}$$

Constitutive relation for chemical potentials will be discussed in Section 2.2.

2.1.3 Electrostatics

It was mentioned above that the electrode particles are partially composed of an electrically conductive binder, so we can treat the electrode particle material as an electrical conductor. As a conductor the electrons are highly mobile, so the rate contribution to the diffusion equations can be neglected. The electron concentration field is therefore governed by the electrostatic equation.

$$\nabla \cdot \mathbf{i} = 0 \tag{2.25}$$

Where $\mathbf{i}$ is the electric field which is a function of the electron concentration gradient and the conductivity of the material, k.

$$\mathbf{i} = -k\nabla\phi \tag{2.26}$$

Mirroring the previous section the governing equation can be expressed in the undeformed configuration with a nominal electric field **I**.

$$\nabla^0 \cdot \mathbf{I} = 0 \tag{2.27}$$

The nominal electric field is then computed as

$$\mathbf{I} = -kJ\mathbf{C}^{-1}\nabla^0\phi \tag{2.28}$$

2.1.4 Redox Surface Reactions

The mechanics and all of the transport phenomena are now defined and all that remains are the redox reactions that occur at the electrode-electrolyte interfaces. The kinetics associated with the surface reaction and intercalation process can be modeled with a Butler-Volmer (BV) equation [5]. The BV equation describes an effective Li/Li+ flux and the associated electron/electric potential flux across the interface provided with an electric potential jump and Li/Li+ concentrations at the interface.

$$\begin{aligned} I_{bv} &= I_0 \left[\exp\left(\tfrac{\alpha_a F}{R_g T} \left(\eta - U'\left(C_s\right) \right) \right) - \exp\left(\tfrac{\alpha_c F}{R_g T} \left(U'\left(C_s\right) - \eta \right) \right) \right] \\ I_0 &= Fk(C_{s\,\max} - C_s)^{\alpha_a} {C_s}^{\alpha_c} {C_l}^{\alpha_a} \\ \eta &= \phi_s - \phi_l \end{aligned} \tag{2.29}$$

where I_{bv} is the effective nominal electric potential flux into the interface of the electrode host, C_s and ϕ_s are the nominal concentration of the neutral transport species and electric potential in the electrode host, C_l and ϕ_l are the nominal concentration of the transport ions and electric potential in the electrolyte, α_a and α_c are the anodic and cathodic transfer coefficients respectively, and k is the surface reaction rate constant. It is not made clear in literature whether true of nominal concentrations should be used in the Butler-Volmer treatment of the double layer. To minimize extra complication nominal concentrations are used, but the implementation would only require minor adjustments to allow true concentrations. Due to conservation of species, we have the

following coupling conditions at the electrode electrolyte interfaces.

$$I_{bv} = \mathbf{I}_s \cdot \mathbf{n}_{s0} = F\left(\mathbf{J}_s \cdot \mathbf{n}_{s0}\right) = -F\left(\mathbf{J}_l \cdot \mathbf{n}_{l0}\right) \tag{2.30}$$

the terms with a subscript s are relative to the electrode particle and the terms with a subscript l are relative to the electrolyte. It should be noted that the normals, $\mathbf{n_0}$, point away from their associated bodies, and thus $\mathbf{n}_s 0$ and $\mathbf{n}_l 0$ point in opposite directions.

2.2 Constitutive Relations

In the previous section governing equations for various phenomena involved in battery operation were developed assuming constitutive relations were given. In this section there is detailed discussion on how constitutive relations are developed for various systems. We begin by describing uncoupled systems; the degree and complexity of coupling progresses throughout the section.

2.2.1 Simple Elasticity

Neglecting plasticity and fracture mechanics a general framework for computing elastic stresses is discussed. First there is a brief discussion of general elasticity, without swelling, followed by a much more detailed discussion on general elasticity with intercalation induced swelling. The variation of the free energy balance for a purely elastic structure which is subjected to only mechanical constraints and loads can be written as [33]

$$\mathbf{P} : \delta\mathbf{F} - \delta W = 0 \tag{2.31}$$

where W is the total free energy density with respect to the un-deformed body. In this simple case where all of the free energy stored is due to elastic deformation we can write $W = \Psi$ where Ψ is the elastic strain energy density. There will not be any discussion on how elastic strain energy density functions are derived because there are numerous mechanics resources that delve very deep into the subject including [8, 33, 1, 2]. Instead

the following discussions assume that elastic strain energy density functions are given; a framework is developed which makes it relatively easy to swap between existing elastic strain energy density functions. Using chain rule on the variation of the free energy density we arrive at

$$\left(\mathbf{P} - \frac{\partial \Psi}{\partial \mathbf{F}}\right) : \delta \mathbf{F} = 0 \tag{2.32}$$

which brings us to the following constitutive equation for determining the nominal stress tensor.

$$\mathbf{P} = \frac{\partial \Psi}{\partial \mathbf{F}} \tag{2.33}$$

The various strain energy density functions which have been implemented in our finite element framework are listed in appendix 8.2. Most strain energy density functions including all the ones discussed within can be written as

$$\Psi = \Psi^{iso}(\mathbf{F}) + \Psi^{vol}(J) \tag{2.34}$$

where Ψ^{vol} is the volumetric component which accounts for the energy stored by forced volume change, and Ψ^{iso} is the isochoric component which accounts for energy stored by the volume preserving portion of deformation. In the above decomposition the volumetric component only influences the strain energy when there is volume change.

In ideally incompressible materials volume must be preserved so the volumetric component of the strain energy is identically zero ($\Psi^{vol} = 0$). Incompressible materials can accommodate infinite pressures without deforming, so the pressure in an incompressible material can not be modeled as a function of the deformation state alone. Therefore, to account for pressure with an incompressible material model, osmotic pressure must be considered as an independent state variable defined as the internal pressure required to preserve volume. For incompressible elastic materials the strain energy density function can be written as

$$\Psi = \Psi^{iso}(\mathbf{F}) + \Psi^{p_o} \tag{2.35}$$

where Ψ^{p_o} is the internal energy required to preserve volume and is defined with the following equation.

$$\Psi^{p_o} = (J-1)\, p_o \tag{2.36}$$

The above equation is the result of using a Lagrange multiplier to satisfy the incompressibility condition ($J = 1$) where p_o is the Lagrange multiplier. Inserting Equation (2.36) into Equation (2.35) And differentiating with respect to the deformation gradient, we arrive at the following equation for the Nominal stress in an incompressible material [33].

$$\mathbf{P} = \frac{\partial \Psi^{iso}}{\partial \mathbf{F}} + \frac{\partial \Psi^{p_o}}{\partial \mathbf{F}} = \frac{\partial \Psi^{iso}}{\partial \mathbf{F}} + p_o J \mathbf{F}^{-T} \tag{2.37}$$

The internal energy required to preserve volume is frequently defined as the negative of the definition above [33, 8]. The only consequence of using the alternative definition in Equation (2.37) is the positive osmotic pressure is tensile instead of compressive, which is consistent with sign convention used with stresses. Since osmotic pressure has been added as a state variable we must add a new governing equation to control the new state variable. The new governing equation for controlling osmotic pressure is written below.

$$J - 1 = 0 \tag{2.38}$$

2.2.2 Simple Diffusion

In general diffusion is driven by chemical potential gradients. Constitutive relations for chemical potentials are derived assuming that a chemical free energy density function (W^C) is provided. In literature W^C is almost never provided; instead chemical potentials are often directly given. There is some discussion on how different assumptions about the origins of chemical potentials affect the model. The variation of the free energy balance for a purely chemical system which is subjected to only concentration

and flux constraints can be written as [34]

$$\mu_c \delta C - \delta W = 0 \tag{2.39}$$

In this simple case where all of the free energy stored is due to species transport we can write $W = W^C$ where W^C is the chemical free energy density. Using chain rule on Equation (2.39) we arrive at the following constitutive relation for the chemical potential.

$$\mu_c = \frac{\partial W^C}{\partial C} \tag{2.40}$$

A number of different chemical potentials are listed in appendix 8.3 for reference.

2.2.3 Coupled Elasticity and Diffusion

Now that general constitutive relations have been devised for uncoupled elasticity and diffusion, relations are devised for coupled elasticity and diffusion. Intercalation induced swelling will continue to be ignored until the next subsection. Summing the free energy balances in Equations (2.31) and (2.39) we end up with the following variational free energy balance for coupled elasticity and diffusion.

$$\mathbf{P} : \delta \mathbf{F} + \mu_c \delta C - \delta W = 0 \tag{2.41}$$

The free energy density (W) of the coupled system is simply the sum of the elastic strain energy density (Ψ) and the chemical free energy density (W^C). Using chain rule on the variation of the free energy density we arrive at

$$\left(\mathbf{P} - \frac{\partial \Psi}{\partial \mathbf{F}} - \frac{\partial W^C}{\partial J} J \mathbf{F}^{-T} \right) : \delta \mathbf{F} + \left(\mu_c - \frac{\partial W^C}{\partial C} - \frac{\partial \Psi}{\partial C} \right) \delta C = 0 \tag{2.42}$$

Therefore, in systems with coupled elasticity and diffusion the nominal stress can be computed as

$$\mathbf{P} = \frac{\partial \Psi}{\partial \mathbf{F}} + \frac{\partial W^C}{\partial J} J \mathbf{F}^{-T} \tag{2.43}$$

and the chemical potential can be computed as

$$\mu_c = \frac{\partial W^C}{\partial C} + \frac{\partial \Psi}{\partial C} \tag{2.44}$$

The equation for nominal stress (2.43) is identical to equation presented in the "Simple Elasticity" Section (2.33) with an additional term added to account for a possible dependence of W^C on the volume change characterized determinant of the deformation gradient (J). As chemical free energy density functions are rarely provided we have found no literature which presents W^C as a function of J. However, the chemical potential which characterizes simple Fickian diffusion is often presented as

$$\mu_c = \mu_{c0} + R_g T \ln(c) = \frac{\partial W^C}{\partial C} \tag{2.45}$$

where c is the true concentration, R_g is the gas constant and T is the absolute temperature. Using the relation between the true and nominal concentration ($c = CJ^{-1}$) and integrating with respect to C we arrive at the following form of W.

$$W^C = C\left(\mu_{c0} + R_g T\left[\ln(C) - \ln(J) - 1\right]\right) \tag{2.46}$$

Therefore, when modeling Fickian diffusion on a finitely deforming body without swelling the second term in Equation (2.43) takes on the following form.

$$\frac{\partial W^C}{\partial J} J\mathbf{F}^{-T} = -CR_g T\mathbf{F}^{-T} \tag{2.47}$$

Inserting Equation (2.47) into Equation (2.43) we arrive at the following constitutive relation for computing the chemical potential.

$$\mathbf{P} = \frac{\partial \Psi}{\partial \mathbf{F}} - CR_g T\mathbf{F}^{-T} \tag{2.48}$$

Because the author has found no literature which discusses this form of coupling the second term in the stress equation is ignored. In order to minimize errors due to incorrect assumptions it would be valuable for future researchers to study the impact of including the additional term.

$$\Rightarrow \mathbf{P} = \frac{\partial \Psi}{\partial \mathbf{F}} \tag{2.49}$$

The equation for determining the chemical potential (2.44) is identical to equation presented in the "Simple Diffusion" Section2.40 with an additional term added to account for a possible dependence of Ψ on the nominal concentration (C). As we are not considering swelling yet, the deformation is not directly dependent on the concentration. However, if elastic constants vary with concentration the ($\frac{\partial \Psi}{\partial C}$) term will be non-zero.

When modeling a nearly incompressible material, any explicit dependence on J is removed with the following identity

$$J = 1 \tag{2.50}$$

and Ψ^{vol} is replaced by Ψ^{p_o} as described in Section 2.2.1, leading us to the following free energy balance.

$$\left(\mathbf{P} - \frac{\partial \Psi^{iso}}{\partial \mathbf{F}} - p_0 J \mathbf{F}^{-T}\right) : \delta \mathbf{F} + \left(\mu_c - \frac{\partial W^C}{\partial C} - \frac{\partial \Psi^{iso}}{\partial C}\right) \delta C + (1 - J)\, \delta p_0 = 0 \tag{2.51}$$

Therefore, we arrive at the following equations for determining the nominal stress tensor ($\mathbf{P}$) and chemical potential (μ).

$$\mathbf{P} = \frac{\partial \Psi}{\partial \mathbf{F}} + p_0 J \mathbf{F}^{-T} \tag{2.52}$$

$$\mu_c = \frac{\partial W^C}{\partial C} + \frac{\partial \Psi}{\partial C} \tag{2.53}$$

As in Section 2.2.1 p_o is added as a state variable governed by Equation (2.38).

2.2.4 Coupled Elasticity and Diffusion with Swelling

Building off of the discussion in Section 2.2.3 we now consider swelling in our coupled transport models. It is assumed that the deformation state can be decomposed into two sequential deformations: a concentration induced swelling and a elastic deformation. The figure below illustrates the deformation decomposition.

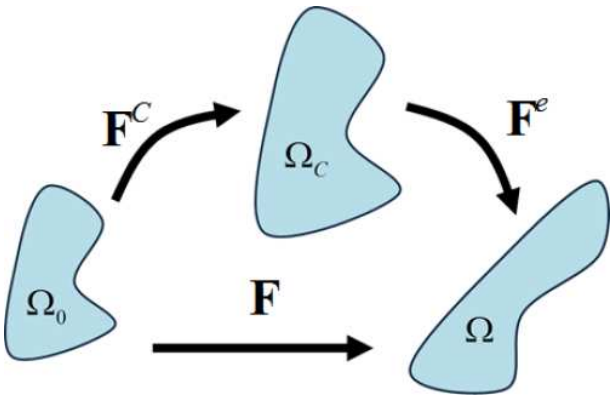

Figure 2.2: Decomposition of deformation state.

Decomposing the deformation in this way is equivalent to representing the deformation gradient as

$$\mathbf{F} = \mathbf{F}^e\mathbf{F}^C \tag{2.54}$$

where $\mathbf{F}^C$ is the concentration induced swelling and $\mathbf{F}^e$ is the elastic deformation that follows. Because the swelling is a result of adding molecules to the electrode particle material, we assume that the volume increase is proportional to the number of moles of species absorbed multiplied by the volume of a mole of the absorbed species. Written mathematically

$$\frac{V}{V_0} = \det\left(\mathbf{F}^C\right) = 1 + \Omega C = J^C \tag{2.55}$$

Anisotropic swelling in a cartesian coordinate frame can be modeled by using a deformation gradient of the following form.

$$\mathbf{F}^C = \begin{bmatrix} \mathrm{f}_{cx} & 0 & 0 \\ 0 & \mathrm{f}_{cy} & 0 \\ 0 & 0 & \mathrm{f}_{cz} \end{bmatrix} (1 + \Omega C)^{1/3} = \mathbf{f}^C(1 + \Omega C)^{1/3} \tag{2.56}$$

where $\det\left(\mathbf{f}^C\right) = 1$. Assuming that the volume expansion is isotropic the swelling contribution to the deformation gradient can be expressed as

$$\mathbf{F}^C = (1 + \Omega C)^{1/3}\boldsymbol{\delta} \tag{2.57}$$

Zhao et al. [61] and Bower et al. [9] use similar decompositions in their treatments of mechanical equilibrium in silicon electrode particles during lithiation. Zhao decomposed the deformation into a stress free inelastic deformation followed by an elastic deformation. Zhao's inelastic deformation is analogous to our concentration induced swelling part, but in Zhao's decomposition the inelastic deformation is composed of a species induced swelling and a plastic deformation. We don't model plastic deformation. Multiplicative decompositions are commonly assumed in intercalation induced swelling models [15, 16].

In swelling intercalation electrode models it is assumed that the intercalation induced swelling ($\mathbf{F}^C$) is stress free and all of the strain energy stored in the system is attributed to the deformation relative to the stress free swollen body ($\mathbf{F}^e$) [18, 17, 60, 59, 11, 11, 27, 29, 61, 9, 22]. Models based on this assumption will be referred to as total strain energy coupled (TSEC) because the total strain energy is dependent only on the elastic deformation. With the TSEC assumption any of the strain energy densities listed in appendix 8.2 can be used to characterize the strain energy density with respect to the stress-free swollen body (Ψ^e). The Neo-Hookean model taken from [2] (8.7) adapted for the TSEC formulation is written as

$$\Psi^e = \frac{\mu_0}{2}\left(\bar{I}_1^e - 3\right) + \frac{\kappa_0}{2}(J^e - 1)^2 \tag{2.58}$$

where $\bar{I}_1^e = trace\left(\bar{\mathbf{C}}^e\right)$ is the first invariant of the isochoric elastic right Cauchy green deformation tensor defined as

$$\bar{\mathbf{C}}^e = (J^e)^{-2/3}\mathbf{C}^e = (J^e)^{-2/3}\mathbf{F}^{eT}\mathbf{F}^e \tag{2.59}$$

Ψ^e characterizes the strain energy density with respect to the stress free swollen body, so the strain energy density with respect to the undeformed body is

$$\Psi = J^C\Psi^e \tag{2.60}$$

Inserting Equation (2.60) into the free energy balance (2.41) and applying chain rule we arrive at the following free energy balance for our TSEC model.

$$\left(\mathbf{P} - J^C \frac{\partial \Psi^e}{\partial \mathbf{F}^e} : \frac{\partial \mathbf{F}^e}{\partial \mathbf{F}}\right) : \delta \mathbf{F} + \left(\mu_c - \frac{\partial W^C}{\partial C} - \frac{\partial J^C}{\partial C}\Psi^e - J^C \frac{\partial \Psi^e}{\partial \mathbf{F}^e} : \frac{\partial \mathbf{F}^e}{\partial C}\right) \delta C = 0 \quad (2.61)$$

Then nominal stress tensor ($\mathbf{P}$) and chemical potential (μ) are computed with the following relations.

$$\mathbf{P} = J^C \frac{\partial \Psi^e}{\partial \mathbf{F}^e} : \frac{\partial \mathbf{F}^e}{\partial \mathbf{F}} \quad (2.62)$$

$$\mu_c = \frac{\partial W^C}{\partial C} + \frac{\partial J^C}{\partial C}\Psi^e + J^C \frac{\partial \Psi^e}{\partial \mathbf{F}^e} : \frac{\partial \mathbf{F}^e}{\partial C} \quad (2.63)$$

Solving Equation (2.54) for $\mathbf{F}^e$ and taking the derivatives with respect to $\mathbf{F}$ and C we find

$$\frac{\partial \mathbf{F}^e}{\partial \mathbf{F}} = \mathbf{F}^{-C} \frac{\partial \mathbf{F}}{\partial \mathbf{F}} = \mathbf{F}^{-C} \underline{\mathbf{I}} \quad (2.64)$$

$$\frac{\partial \mathbf{F}^e}{\partial C} = \frac{\partial \mathbf{F}^{-C}}{\partial C}\mathbf{F} = -\frac{\Omega}{3}\left(J^C\right)^{-4/3}\mathbf{F} \quad (2.65)$$

where $\underline{\mathbf{I}}$ is the fourth order identity tensor. Using Equations (2.64) and (2.57) the equation for determining the nominal stress simplifies to

$$\mathbf{P} = \left(J^C\right)^{2/3} \frac{\partial \Psi^e}{\partial \mathbf{F}^e} \quad (2.66)$$

Using Equations (2.65) and (2.55) the equation for determining the chemical potential simplifies to

$$\mu_c = \frac{\partial W^C}{\partial C} + \Omega \Psi^e - \frac{\Omega}{3}\left(J^C\right)^{-1/3} \frac{\partial \Psi^e}{\partial \mathbf{F}^e} : \mathbf{F} = \frac{\partial W^C}{\partial C} + \Omega \left(\Psi^e - J^{-C} \frac{\mathbf{P} : \mathbf{F}}{3}\right) \quad (2.67)$$

The last term can be further simplified as shown below.

$$J^{-C} \frac{\mathbf{P} : \mathbf{F}}{3} = J^{-C} \frac{trace\left(\mathbf{P}\mathbf{F}^T\right)}{3} = J^{-C} J \frac{trace\left(J^{-1}\mathbf{P}\mathbf{F}^T\right)}{3} = J^e \frac{trace\left(\boldsymbol{\sigma}\right)}{3} = J^e \sigma_h \quad (2.68)$$

σ_h is called the hydrostatic stress. The chemical potential equation can now be expressed as

$$\mu_c = \frac{\partial W^C}{\partial C} + \Omega\left(\Psi^e - J^e \sigma_h\right) \quad (2.69)$$

Equation (2.69) is nearly equivalent to a chemical potential equation presented in Bower et al. [9], but the mechanical constitutive model is presented in more general terms. It should be noted that Bower derives some very similar formulations, but uses thin film approximations and assumes uniform concentration through the thickness of the electrode circumventing all of the complexities associated with modeling coupled transport in the electrode. Neglecting the $(\Omega\Psi^e)$ term and assuming the elastic deformation is volume preserving, i.e. incompressible, we arrive at Zhao's formula for computing the chemical potential [61].

$$\mu_c = \frac{\partial W^C}{\partial C} - \Omega\sigma_h \tag{2.70}$$

Despite the fact that the author has found no published works which present a chemical free energy density that is dependent on the determinant of the deformation gradient, such a dependency is implied in Zhao et. al. 2011 [61]. In this paper Zhao presents the following chemical potential

$$\mu_c = \mu_{c0} + R_g T \ln(c) - \Omega\sigma_h \tag{2.71}$$

It has been somewhat difficult to follow Zhao's for lack of detail, but he appears to assume that the material is nearly incompressible in which case any volume change is purely due to intercalation induced swelling $(J = J^C)$. Zhao replaces c with CJ^{-1} and then uses $(J = 1+\Omega C)$ in his chemical potential to remove any explicit dependence on J. Zhao ends up using the following equation to define the chemical potential. Although the chemical potential used by Zhao doesn't have an explicit dependence on J, the formulas presented in his paper imply such a dependence is possible.

$$\mu_c = \mu_{c0} + R_g T \ln\left(\frac{C}{1+\Omega C}\right) - \Omega\sigma_h \tag{2.72}$$

When modeling a nearly incompressible material, any explicit dependence on J is removed with the following identity

$$J = 1 + \Omega C \tag{2.73}$$

and $\Psi^{e,vol}$ is replaced by

$$\Psi^{p_o} = (J - 1 - \Omega C)\, p_o \tag{2.74}$$

where Ψ^{p_o} results from using a Lagrange multiplier to satisfy the incompressibility condition (2.73). Then the free energy balance takes on the following form.

$$\begin{aligned} &\left(\mu_c - \tfrac{\partial W^C}{\partial C} - \Omega\Psi^{e,iso} + \tfrac{\Omega}{3}\left(J^C\right)^{-1/3}\tfrac{\partial \Psi^{e,iso}}{\partial \mathbf{F}^e} : \mathbf{F} + \Omega p_0\right)\delta C + \\ &(1 + \Omega C - J)\,\delta p_o + \left(\mathbf{P} - \left(J^C\right)^{2/3}\tfrac{\partial \Psi^{e,iso}}{\partial \mathbf{F}^e} - J p_o \mathbf{F}^{-T}\right) : \delta\mathbf{F} = 0 \end{aligned} \tag{2.75}$$

Using the definition

$$\frac{\left(J^C\right)^{2/3}}{3}\frac{\partial \Psi^{e,iso}}{\partial \mathbf{F}^e} : \mathbf{F} = \frac{trace\left(\mathbf{P}^{iso}\mathbf{F}^T\right)}{3} = J\frac{trace\left(\sigma^{iso}\right)}{3} = J^C\sigma_{hiso} \tag{2.76}$$

we arrive at the following equations for determining the nominal stress tensor ($\mathbf{P}$) and chemical potential (μ_c).

$$\mathbf{P} = \left(J^C\right)^{2/3}\frac{\partial \Psi^{e,iso}}{\partial \mathbf{F}^e} + J p_o \mathbf{F}^{-T} = \mathbf{P}^{iso} + J^C p_o \mathbf{F}^{-T} \tag{2.77}$$

$$\mu_c = \frac{\partial W^C}{\partial C} + \Omega\Psi^{e,iso} - \Omega\sigma_{hiso} - \Omega p_0 = \frac{\partial W^C}{\partial C} + \Omega\left(\Psi^{e,iso} - \sigma_h\right) \tag{2.78}$$

Osmotic pressure is added as a state variable with the addition of the following governing equation.

$$J - 1 - \Omega C = 0 \tag{2.79}$$

When modeling hydrogels a different form of coupling is assumed. In intercalation electrodes is assumed that the portion of the deformation described by F^C is stress free, however researchers assert that in hydrogels this is not the case because polymer chains don't swell and are assumed to undergo strain during swelling. It is assumed that the Ψ^{iso} is a function of the total deformation and Ψ^{vol} is only a function of the portion of the deformation described by F^e [15, 16]. Chester and Anand rename Ψ^{iso} the strain entropy (Ψ^{η}) stating that it is the energy stored by straining lattice chains, while Ψ^{vol} is renamed internal strain energy (Ψ^{ε}) stating that it is the energy stored by forced volume change. Models which use this form of strain energy coupling will be referred to

as volumetric strain energy coupled (VSEC) because only the volumetric strain energy is dependent on the elastic deformation alone. With the VSEC assumption any of the strain energy densities listed in Appendix 8.2 can be used to characterize the VSEC strain energy density by replacing J in Ψ_{vol} by J^e. For example the Neo-Hookean model taken from [2] is written as

$$\Psi = \frac{\mu_0}{2}\left(\bar{I}_1 - 3\right) + \frac{\kappa_0}{2}(J^e - 1)^2 \tag{2.80}$$

$\bar{I}_1$ is the first invariant, a.k.a. the trace, of the purely isochoric component of the Right Cauchy Green Deformation tensor defined below

$$\bar{I}_1 = trace\left(\mathbf{C}\right) J^{-2/3} = \left(\mathbf{C} : \mathbf{I}\right) J^{-2/3} \tag{2.81}$$

Applying the chain rule to Equation (2.41) we arrive at the following free energy balance for the VSEC model.

$$\left(\mathbf{P} - \frac{\partial \Psi^{\eta}}{\partial \mathbf{F}} - \frac{\partial \Psi^{\varepsilon}}{\partial J^e} J^e \mathbf{F}^{-T}\right) : \delta\mathbf{F} + \left(\mu_c - \frac{\partial W^C}{\partial C} + \Omega J^{-C} \frac{\partial \Psi^{\varepsilon}}{\partial J^e} J^e\right) \delta C = 0 \tag{2.82}$$

Then the nominal stress tensor ($\mathbf{P}$) and chemical potential (μ) are computed with the following relations.

$$\mathbf{P} = \frac{\partial \Psi^{\eta}}{\partial \mathbf{F}} + \frac{\partial \Psi^{\varepsilon}}{\partial J^e} J^e \mathbf{F}^{-T} \tag{2.83}$$

$$\mu_c = \frac{\partial W^C}{\partial C} - \Omega J^{-C} \frac{\partial \Psi^{\varepsilon}}{\partial J^e} J^e = \frac{\partial W^C}{\partial C} - \Omega J^e \sigma_{\varepsilon} \tag{2.84}$$

σ_{ε} is called internal energy stress.

The VSEC model is adapted for incompressibility in a similar manner as the TSEC model. Any explicit dependence on J is removed by applying Equation (2.73) and Ψ^{ε} is replaced by Ψ^{p_o} in Equation (2.74). The free energy balance takes on the following form.

$$\left(\mathbf{P} - \frac{\partial \Psi^{\eta}}{\partial \mathbf{F}} - J p_o \mathbf{F}^{-T}\right) : \delta\mathbf{F} + \left(\mu_c - \frac{\partial W^C}{\partial C} + \Omega p_o\right) \delta C + \left(1 + \Omega C - J\right) \delta p_o = 0 \tag{2.85}$$

Therefore, the nominal stress tensor ($\mathbf{P}$) and chemical potential (μ) are computed with the following relations.

$$\mathbf{P} = \frac{\partial \Psi^{\eta}}{\partial \mathbf{F}} + J p_o \mathbf{F}^{-T} \tag{2.86}$$

$$\mu_c = \frac{\partial W^C}{\partial C} - \Omega p_o \tag{2.87}$$

Osmotic pressure is added as a state variable with the addition of the governing Equation (2.79). Equations (2.86) and (2.87) are identical to the constitutive relations used by Hong et al. [34] for modeling incompressible hydrogels. A table summarizing all of the constitutive relations for coupled elasticity and diffusion models is shown belowS.

Table 2.1: Coupled Elasticity and Diffusion Constitutive Table

	$\mathbf{P}$	μ_c
NoSwell	$\frac{\partial \Psi}{\partial \mathbf{F}}$	$\frac{\partial W^C}{\partial C}$
NoSwellI	$\frac{\partial \Psi^{iso}}{\partial \mathbf{F}} + p_0 J \mathbf{F}^{-T}$	$\frac{\partial W^C}{\partial C}$
TSEC	$\left(J^C\right)^{2/3} \frac{\partial \Psi^e}{\partial \mathbf{F}^e}$	$\frac{\partial W^C}{\partial C} - \Omega \sigma_h$
TSECI	$\left(J^C\right)^{2/3} \frac{\partial \Psi^{e,iso}}{\partial \mathbf{F}^e} + J^C p_o \mathbf{F}^{-T}$	$\frac{\partial W^C}{\partial C} - \Omega \sigma_h$
VSEC	$\frac{\partial \Psi^{\eta}}{\partial \mathbf{F}} + \frac{\partial \Psi^{\varepsilon}}{\partial J^e} J^e \mathbf{F}^{-T}$	$\frac{\partial W^C}{\partial C} - \Omega J^e \sigma_{\varepsilon}$
VSECI	$\frac{\partial \Psi^{\eta}}{\partial \mathbf{F}} + J p_o \mathbf{F}^{-T}$	$\frac{\partial W^C}{\partial C} - \Omega p_o$

2.3 Physical Interpretation

With governing equations and constitutive relations developed in general terms we next discuss how to apply mathematical models to physical systems of interest. In a simple cell there are two very different bulk regions which we are interested in explicitly modeling; intercalation electrode host material and electrolyte. In both regions there is diffusive transport, but in the electrode host material the transporting molecules are electrically neutral where in the electrolyte the transporting molecules are ions. Also, the electrode host material tends to swell as molecules are absorbed, while this behavior

has not been documented in studies of battery electrolytes.

2.3.1 Intercalation Electrode Host Material

Intercalation electrode host materials typically swell as they absorb the transport species. It is assumed that the mechanical response is much faster than species transport, so the electrode is always in a state of static mechanical equilibrium described in Section 2.1.1. Assuming that the species transport is purely diffusive we use the equations discussed in Section 2.1.2 as the transport governing equations. The complete set of governing equations and constitutive relations used to represent coupled species diffusion-deformation in intercalation electrode host materials are listed below.

$$\boxed{\nabla^0 \cdot \mathbf{P} = \mathbf{0}} \tag{2.88}$$

$$\boxed{\dot{C} + \nabla \cdot \mathbf{J} = 0} \tag{2.89}$$

where $\mathbf{J} = -C\mathbf{M}\nabla^0\mu_c$.

In silicon electrodes neutral lithium causes significant swelling as it is diffusively transported through the electrode. In the electrode modeling community it is usually assumed that the deformation experienced by the host material can be decomposed into a stress free purely inelastic deformation and a purely elastic deformation [18, 17, 60, 59, 11, 11, 27, 29, 61, 9, 22]. In [61] and [9] the inelastic deformation is further decomposed into plastic and species induced swelling deformations, but in most works including those documented within plastic deformation is neglected leaving the decomposition represented by Equation (2.54). Therefore, the TSEC constitutive relations developed in Section 2.2.4 are used do determine the nominal stress tensor and ($\mathbf{P}$) the chemical potential (μ_c) respectively.

$$\boxed{\mathbf{P} = \left(J^C\right)^{2/3} \frac{\partial \Psi^e}{\partial \mathbf{F}^e}} \tag{2.90}$$

$$\boxed{\mu_c = \frac{\partial W^C}{\partial C} + \Omega\left(\Psi^e - J^e \sigma_h\right)} \tag{2.91}$$

The governing and constitutive relations listed above were developed with large deformation in mind. Using small deformation approximations the governing equations can be written as

$$\boxed{\nabla \cdot \boldsymbol{\sigma} = 0} \tag{2.92}$$

$$\boxed{\dot{c} + \nabla \cdot \mathbf{j} = 0} \tag{2.93}$$

where $\mathbf{j} = -cM\nabla\mu_c$. The constitutive relations can be written as

$$\boxed{\boldsymbol{\sigma} = \underline{\mathbf{C}} : \boldsymbol{\varepsilon}^e = \underline{\mathbf{C}} : (\boldsymbol{\varepsilon} - \boldsymbol{\varepsilon}^c)} \tag{2.94}$$

where $\boldsymbol{\varepsilon} = \frac{1}{2}\left[\nabla\mathbf{u} + (\nabla\mathbf{u})^T\right]$ is the total linear strain tensor and $\boldsymbol{\varepsilon}^c = \frac{\Omega}{3}c$ is the linear intercalation induced swelling strain tensor.

$$\boxed{\mu_c = \frac{\partial W^c}{\partial c} - \Omega\sigma_h} \tag{2.95}$$

The above small deformation approximation equations are identical to the ones used in [60, 59, 27, 29, 22] for modeling coupled species diffusion-mechanics in electrode host materials.

2.3.2 Electrolyte

The discussion within is restricted to binary electrolytes. In a binary electrolyte there are only two types of ions; cations which are positively charged and anions which are negatively charged. The ions are assumed to be diffusively transported, so the mass conservation equations discussed in Section 2.1.2 are chosen as the ion transport governing equations. In choosing a diffusive transport model we are neglecting the possibility of fluid like electrolyte flow. We are, however, not very concerned with the electrolyte flow effects and are interested in modeling solid electrolytes and electrolyte pastes. It is, therefore, reasonable to model the electrolyte as a solid governed by the equations discussed in Section2.1.1. In binary electrolytes like the negative ions, the

positive ions may also be mobile in the electrolyte, but in the modeling community they are never both explicitly modeled.

In practice the electro-neutrality assumption is used to simplify the binary electrolyte model [40, 20, 57, 19, 55, 56]. The electro-neutrality condition can be expressed mathematically as

$$C_+ = C_- = C \tag{2.96}$$

where C_+ and C_- are the nominal cation and anion concentrations respectively, and C will be referred to as the nominal ion concentration. The consequences on the electro-neutrality assumption are we have two different mass balances governing the same state variable. Written with respect to the un-deformed electrolyte

$$\frac{\partial C}{\partial t} + \nabla^0 \cdot \mathbf{J}_+ = 0 = R_{C+} \tag{2.97}$$

$$\frac{\partial C}{\partial t} + \nabla^0 \cdot \mathbf{J}_- = 0 = R_{C-} \tag{2.98}$$

where

$$\mathbf{J}_+ = -\frac{CD_+}{R_g T}\nabla^0 \mu_+ = -C\mathbf{M}_+ \nabla^0 \mu_+ \tag{2.99}$$

$$\mathbf{J}_- = -\frac{CD_-}{R_g T}\nabla^0 \mu_- = -C\mathbf{M}_- \nabla^0 \mu_- \tag{2.100}$$

μ_+ and μ_- are the electrochemical potentials that drives cation diffusion and anion diffusion respectively. Ion diffusion in electrolytes is typically assumed to be driven by electrochemical potentials of the following form [40, 20, 19, 55].

$$\mu_{ci} = \mu_{ci0} + R_g T \log(c_i) + z_i F \phi = \mu_{ci0} + \mu_{ciF} + \mu_\phi \tag{2.101}$$

where c_i is the concentration of the ion i, μ_{ci0} is the initial electrochemical potential ion i, μ_{ciF} is the portion of electrochemical potential which results in Fickian diffusion ion i, ϕ is the electric potential, and μ_ϕ is the electric potential contribution to the electrochemical potential. The subscript "i" represents the i^{th} ion in an electrolyte with N different types of ions. In the binary electrolyte $i \in \{+, -\}$. c_+ and c_- are the true

cation and anion concentrations respectively, and z_+ and z_- are the cation and anion valence numbers respectively. In binary electrolytes $z_+ = -z_- = z$ where we will refer to z as the ion valence number.

The first two terms in Equation (2.101) result in Fickian diffusion, and the third term accounts for ion migration. Ion migration can be described as the diffusion of ions driven by electric forces. Equation (2.101) is expressed as a function of the true concentrations, but in our finite deformation models depend on nominal concentrations. c_i is replaced by $\frac{C_i}{J}$ resulting in the following chemical potential equation.

$$\mu_{ci} = \mu_{ci0} + R_g T \left[\ln\left(C\right) - \ln\left(J\right)\right] + z_i F \phi \tag{2.102}$$

Inserting the electrochemical potential (2.102) into the nominal flux Equations (2.99) and (2.100) we arrive at

$$\mathbf{J}_+ = -C\mathbf{M}_+ \left[\nabla^0 \mu_{cF} + zF\nabla^0 \phi\right] \tag{2.103}$$

$$\mathbf{J}_- = -C\mathbf{M}_- \left[\nabla^0 \mu_{cF} - zF\nabla^0 \phi\right] \tag{2.104}$$

Combining the cation and anion governing equations in the following way we arrive at the new governing equation for the ion concentration.

$$\begin{aligned} \tfrac{D_- R_{C+} + D_+ R_{C-}}{D_+ + D_-} = \quad & \nabla^0 \left(\tfrac{D_-}{D_+ + D_-}\right) \cdot \mathbf{J}_+ + \nabla^0 \left(\tfrac{D_+}{D_+ + D_-}\right) \cdot \mathbf{J}_- \\ & + \tfrac{\partial C}{\partial t} - \nabla^0 \cdot \left[\mathbf{M}_P C \nabla^0 \mu_{cF}\right] \end{aligned} \tag{2.105}$$

Where $\mathbf{M}_p = \frac{D_+ D_-}{D_+ + D_-} \frac{\mathbf{C}^{-1}}{R_g T} = \frac{D_p}{R_g T} \mathbf{C}^{-1}$. Assuming the diffusion coefficients are constant the terms involving gradient of diffusion coefficients vanish resulting in the following governing equation for binary electro neutral electrolyte ion transport.

$$\frac{\partial C}{\partial t} + \nabla^0 \cdot \left[-\mathbf{M}_p C \nabla^0 \mu_{cF}\right] = \frac{\partial C}{\partial t} + \nabla^0 \cdot \mathbf{J}_p = 0 \tag{2.106}$$

$\mathbf{J}_p$ is called the nominal pseudo ion flux. The pseudo designation is used because $\mathbf{J}_p$ is not actually the flux experienced by the ions, it is an algebraic combination of cation and anion flux Equations (2.103) and (2.104). Combining the cation and anion

governing equations in a different way we arrive at the following governing equation for the electrolyte electric potential.

$$\begin{aligned} D_- R_{C+} + D_+ R_{C-} &= \nabla^0 \cdot \mathbf{I}_P = 0 \\ \mathbf{I}_P &= F\frac{C\mathbf{C}^{-1}}{R_g T}\left[-\left(D_+ - D_-\right)\nabla^0 \mu_{cF} - \left(D_+ + D_-\right) zF\nabla^0 \phi\right] \end{aligned} \tag{2.107}$$

$\mathbf{I}_p$ is called the pseudo nominal electric field.

The complete set of governing equations used in modeling deformation, ion transport, and electric potential are listed below.

$$\boxed{\nabla^0 \cdot \mathbf{P} = \mathbf{0}} \tag{2.108}$$

$$\boxed{\dot{C} + \nabla^0 \cdot \mathbf{J}_p = 0} \tag{2.109}$$

$$\boxed{\nabla^0 \cdot \mathbf{I}_P = 0} \tag{2.110}$$

The constitutive relations are listed next.

$$\boxed{\mathbf{P} = \frac{\partial \Psi}{\partial \mathbf{F}}} \tag{2.111}$$

Ψ can be any of the strain energy density functions listed in appendix 8.2.

$$\boxed{\mathbf{J}_p = -\mathbf{M}_p C \nabla^0 \mu_{cF} = \frac{D_- \mathbf{J}_+ + D_+ \mathbf{J}_-}{D_+ + D_-}} \tag{2.112}$$

Any of the chemical potentials listed in appendix 8.3 can be used in the place of μ_{cF}.

$$\boxed{\mathbf{I}_P = \frac{FC\mathbf{C}^{-1}}{R_g T}\left[-\left(D_+ - D_-\right)\nabla^0 \mu_{cF} - \left(D_+ + D_-\right) zF\nabla^0 \phi\right] = F\left(\mathbf{J}_+ - \mathbf{J}_-\right)} \tag{2.113}$$

The final assumption made for the binary electro-neutral electrolyte is only the cations can be extracted from and inserted into the electrolyte through an interface. Written mathematically as

$$\mathbf{J}_- \cdot \mathbf{n}_0 = 0 \tag{2.114}$$

where $\mathbf{n}_0$ the unit surface outward normal with respect to the undeformed electrolyte interface. Therefore, the interface nominal pseudo ion flux and the interface nominal pseudo electric flux must satisfy the following conditions.

$$\mathbf{J}_p \cdot \mathbf{n}_0 = \frac{D_-}{D_+ + D_-}\mathbf{J}_+ \cdot \mathbf{n}_0 \tag{2.115}$$

$$\boxed{\mathbf{I}_p \cdot \mathbf{n}_0 = F\mathbf{J}_+ \cdot \mathbf{n}_0} \tag{2.116}$$

Because batteries are driven electrically the interface electric flux condition (2.116) is used to externally drive ion transport, and the interface nominal pseudo ion flux condition is satisfied just inside the interface with the following equation.

$$\boxed{\mathbf{J}_p \cdot \mathbf{n}_0 = \frac{D_-}{F\left(D_+ + D_-\right)}\mathbf{I}_p \cdot \mathbf{n}_0} \tag{2.117}$$

The governing and constitutive relations listed above were developed with large deformation in mind. Using small deformation approximations the governing equations can be written as

$$\boxed{\nabla \cdot \boldsymbol{\sigma} = 0} \tag{2.118}$$

$$\boxed{\dot{c} + \nabla \cdot \mathbf{j}_p = 0} \tag{2.119}$$

$$\boxed{\nabla \cdot \mathbf{i}_P = 0} \tag{2.120}$$

and the constitutive relations can be represented with the following equations.

$$\boxed{\boldsymbol{\sigma} = \underline{\mathbf{C}} : \boldsymbol{\varepsilon} = \underline{\mathbf{C}} : \left(\frac{\mathbf{1}}{\mathbf{2}}\left[\nabla \mathbf{u} + (\nabla \mathbf{u})^{\mathbf{T}}\right]\right)} \tag{2.121}$$

$$\boxed{\mathbf{j}_p = -\frac{D_p c}{R_g T}\nabla \mu_{cF}} \tag{2.122}$$

$$\boxed{\mathbf{i}_P = \frac{Fc}{R_g T}\left[-\left(D_+ - D_-\right)\nabla \mu_{cF} - \left(D_+ + D_-\right) zF\nabla \phi\right]} \tag{2.123}$$

The above small deformation approximation equations are identical to the ones used in [20, 19, 55] for modeling ion transport through electrolytes, except that mechanics was completely ignored. It's worth noting that although much of the models presented within can be viewed as finite deformation extensions of those used by Dr. Stephanie Golmon, the electrolyte transport model is somewhat different from one used by Dr. Golmon. The model used in [27] can be written as

$$\mathbf{i}_P = -\kappa\left[\nabla \phi - \frac{R_g T}{F}\left(1 - t_+^0\right)\nabla\left(\ln c\right)\right] \tag{2.124}$$

The differences in ours versus Golmon's the models can be attributed to their origins. Our models are based on dilute solution theory which is evident from the lack of interaction terms in the electrochemical potentials of the positive and negative ions. Golmon's model, on the other hand, is based on the concentrated solution theory presented in the PhD thesis of Dr. Doyle [24]. One of the major goals of the works within was to build upon existing models electrochemical models and develop a complete set of microscale models which can be used to model finite deformation mechanics and transport in a battery cell. A complete set of models have been developed and implemented in a finite element framework, but the job of determining if dilute solution theory assumptions are completely appropriate for their intended use remains for future researchers.

2.3.3 Surface Elasticity

DeLuca et al. [22] demonstrated that stress states during swelling, in silicon electrode particles in the <100nm range, are completely dominated by surface stress effects. As we are interested in modeling particles in this range a surface stress model is developed. In general, structures with macro-scale characteristic lengths are mostly unaffected by the influence of surface stress, but when characteristic lengths are in the micro-scale, the surface stress can dominate the stress state [38, 45, 50]. A general expression for surface stress was originally developed by Gurtin et al. [31]. The equilibrium equation on the surface is written as

$$\boldsymbol{\sigma} \cdot \mathbf{n} - \nabla^{\Gamma} \cdot \boldsymbol{\tau} = 0 \tag{2.125}$$

where $\boldsymbol{\tau}$ is the surface stress tensor. The surface elasticity equations were formulated for and studied with the linear strain models; some modifications should probably be made if implementing the models in a finite strain context. The surface stress tensor is a function of the surface stretch , $\boldsymbol{\varepsilon}^{\Gamma}$, and the surface mechanical properties.

$$\boldsymbol{\varepsilon}^{\Gamma} = \frac{1}{2}\left(\nabla^{\Gamma}\mathbf{u} + \nabla^{\Gamma}\mathbf{u}^{T}\right) \tag{2.126}$$

∇^{Γ} is the surface differential operator, which was defined by Gurtin et al. [31]. The surface constitutive relation has been expressed in many different ways; we use one of the most generic forms [38, 45, 42, 43, 22].

$$\boldsymbol{\tau} = \boldsymbol{\tau}_0 + \mathrm{K}^s : \boldsymbol{\varepsilon}^{\Gamma} \tag{2.127}$$

In Equation (2.127) $\boldsymbol{\tau}_0$ is the initial surface stress and K^s is the surface elastic constitutive tensor. In our implementations the 4^{th} order tensors are flattened out into matrices and the second order tensors are flattened out into vectors. The surface stress equation is represented as

$$\bar{\boldsymbol{\tau}} = \bar{\boldsymbol{\tau}}_0 + \bar{\mathbf{K}}^s \bar{\boldsymbol{\varepsilon}}^{\Gamma} = \begin{bmatrix} \tau_{11} \\ \\ \tau_{22} \end{bmatrix} = \begin{bmatrix} \tau_{011} \\ \\ \tau_{022} \end{bmatrix} + \begin{bmatrix} {\mathrm{K}^s}_{11} & {\mathrm{K}^s}_{12} \\ \\ {\mathrm{K}^s}_{12} & {\mathrm{K}^s}_{22} \end{bmatrix} \begin{bmatrix} \varepsilon_{11} \\ \\ \varepsilon_{22} \end{bmatrix} \tag{2.128}$$

Surface elastic properties for Si can be found in Miller and Shenoy 2000 [38].

Chapter 3

Model Implementation

Pertinent physical systems have been characterized with mathematical models. In order to facilitate using the models to study interesting problems the models are implemented in a finite element framework. The finite element framework consists of a time solver for marching the system through time, a non-linear solver for computing the solution at each time step, a linear solver for computing the step towards the solution on each iteration of the non-linear solve, and an element assembly routine for assembling the elemental residuals and jacobians them into the global residual and jacobian to facilitate the linear solve step. In the framework there are a number of choices for time solvers, non-linear solvers, and linear solvers. In most of the studies presented within a first order accurate backward difference formula time solver, a standard Newton non-linear solver, and a direct linear solver are used.

In the finite element framework the elements are responsible for integrating the governing equations, while the material models are responsible for the constitutive equations. This is accomplished by building routines for computing necessary state variables and their gradients into the elements. The state variables and their gradients are computed by the elements and then are passed to the materials where they are used with the constitutive relations to compute derived values, such as $\mathbf{P}$ and $\mathbf{J}$, and their derivatives with respect to the state variables. The derived values and their derivatives are then passed back to the element where they are used with the governing equations to compute

elemental residual and jacobian contributions. With this framework an element can be adapted to simulate many different physical systems simply by using different material models. The nodally discretized state variable are referred to as Degrees of Freedom (DOFs) within and are denoted with the symbol that has been used to represent the corresponding state variable but with a $\sim$ hat.

3.1 Finite Element Types

The different element formulations that have been implemented are presented in the context of the weak form of their governing equations. The elements handle the nodal DOFs in a vector form. In each element nodal DOF residuals are computed and returned as vector and the derivatives of the residual vector with respect to the 0^{th}, 1^{st}, and 2^{nd} derivatives of the nodal DOFs with respect to time are computed and returned as matrices. The assembly routine, knowing how the 0^{th}, 1^{st}, and 2^{nd} time derivatives of the nodal DOFs were computed, assembles the total jacobian from the components accordingly.

3.1.1 Small Deformation Electrode Particle Element

This element implementation is based on the small deformation formulation discussed in Section 2.3.1, and designed for simulating intercalation electrode materials. It operates on displacement ($\tilde{\mathbf{u}}$), species concentration ($\tilde{c}$), electric potential ($\tilde{\phi}$), and hydrostatic stress ($\tilde{\sigma}_h$) DOFs. The $\tilde{\mathbf{u}}$ DOFs are interpolated quadratically, the $\tilde{c}$ and $\tilde{\phi}$ DOFs can be interpolated quadratically or linearly, and the $\tilde{\sigma}_h$ DOFs are interpolated linearly. At each integration point the element can directly compute the following quantities.

$$\begin{array}{cccccccccccc} \text{Var} & \mathbf{u} & c & \dot{c} & \phi & \sigma_h & \boldsymbol{\varepsilon} & \boldsymbol{\varepsilon}_\Gamma & \nabla c & \nabla\phi & \nabla\sigma_h \\ \frac{\partial(\text{Var})}{\partial\tilde{*}} & \frac{\partial\mathbf{u}}{\partial\tilde{\mathbf{u}}} & \frac{\partial c}{\partial\tilde{c}} & \frac{\partial\dot{c}}{\partial\tilde{c}} & \frac{\partial\phi}{\partial\tilde{\phi}} & \frac{\partial\sigma_h}{\partial\tilde{\sigma}_h} & \frac{\partial\boldsymbol{\varepsilon}}{\partial\tilde{\mathbf{u}}} & \frac{\partial\boldsymbol{\varepsilon}_\Gamma}{\partial\tilde{\mathbf{u}}} & \frac{\partial(\nabla c)}{\partial\tilde{c}} & \frac{\partial(\nabla\phi)}{\partial\tilde{\phi}} & \frac{\partial(\nabla\sigma_h)}{\partial\tilde{\sigma}_h} \end{array} \tag{3.1}$$

All of the above variables are defined in the small deformation approximation discussions in Chapter 2.

$$D_- R_{C+} + D_+ R_{C-} = \nabla^0 \cdot \mathbf{I}_P = 0$$

$$\mathbf{I}_P = F\frac{C\mathbf{C}^{-1}}{R_g T}\left[-\left(D_+ - D_-\right)\nabla^0 \mu_{cF} - \left(D_+ + D_-\right) zF\nabla^0 \phi\right]$$

The mechanics governing equation is expressed in the weak form below.

$$\delta W_{\mathbf{u}} = -\int_{\Omega} \delta\boldsymbol{\varepsilon} : \boldsymbol{\sigma}\, d\Omega - \int_{\Gamma} \delta\boldsymbol{\varepsilon}_{\Gamma} \colon \tau\, d\Gamma + \int_{\Gamma} \delta\mathbf{u}\ \cdot (\boldsymbol{\sigma}\cdot\mathbf{n})\, d\Gamma = 0 \tag{3.2}$$

c, $\boldsymbol{\varepsilon}$, and their DOF derivatives are passed to the material model where they are used to compute $\boldsymbol{\sigma}$, $\frac{\partial \boldsymbol{\sigma}}{\partial \tilde{\mathbf{u}}}$, and $\frac{\partial \boldsymbol{\sigma}}{\partial \tilde{c}}$. The element uses the stress tensor ($\boldsymbol{\sigma}$) and it's derivatives to compute the resudial and jacobian contributions represented by the first term in Equation (3.2). The second term in Equation (3.2) is treated in a similar way, but it is only integrated on surfaces. If provided a traction vector or surface pressure, they are integrated over the surface as represented by the third term in Equation (3.2). To integrate a surface traction vector the $(\boldsymbol{\sigma}\cdot\mathbf{n})$ term is replaced by the provided vector, and to integrate a surface pressure the $(\boldsymbol{\sigma}\cdot\mathbf{n})$ term is replaced by the provided pressure times the normal vector.

The species diffusion governing equation is written in the weak form below.

$$\delta W_c = \int_{\Omega} \left(\delta c\dot{c} - \delta\nabla c\cdot\mathbf{j}\right) d\Omega + \int_{\Gamma} \delta c\, \mathbf{j}\cdot\mathbf{n}\, d\Gamma = 0 \tag{3.3}$$

The first term in the first integral in Equation (3.3) is integrated directly without any assistance from the material model. c, ∇c, $\nabla\sigma_h$, and their DOF derivatives are passed to the material model where they are used to compute $\mathbf{j}$, $\frac{\partial \mathbf{j}}{\partial \tilde{c}}$, and $\frac{\partial \mathbf{j}}{\partial \tilde{\sigma}_h}$. The element uses the flux vector ($\mathbf{j}$) and it's derivatives to compute the resudial and jacobian contributions represented by the second term in the first integral in the species diffusion governing Equations (3.3). The second integral in Equation (3.3) represents the surface species flux. If a surface flux is provided it is integrated by replacing $(\mathbf{j}\cdot\mathbf{n})$ with the provided

flux. Surface flux can also be computed with the BV equations by providing the material model with concentrations and voltages on both sides of the interface.

The electric potential governing equation written in the weak form is

$$\delta W_\phi = -\int_\Omega \delta\nabla\phi \cdot \mathbf{i}\, d\Omega + \int_\Gamma \delta\phi\, \mathbf{i}\cdot\mathbf{n}\, d\Gamma = 0 \tag{3.4}$$

$\nabla\phi$ and it's DOF derivatives are passed to the material model where they are used to compute $\mathbf{i}$ and $\frac{\partial \mathbf{i}}{\partial \tilde{\phi}}$. The element uses the electric field vector ($\mathbf{i}$) and it's derivatives to compute the resudial and jacobian contributions represented by the first integral in the electric potential governing Equation (3.4). The second integral in Equation (3.4) represents the surface electric flux. If a surface flux is provided it is integrated by replacing ($\mathbf{i}\cdot\mathbf{n}$) with the provided flux. Surface electric flux can also be computed with the BV equations.

This element is set up to allow stress assisted diffusion models. In stress assisted diffusion flux can be driven by pressure gradients, but since pressure is already a function of the displacement gradients spacial second derivatives would be required to directly compute the pressure gradients. To simplify the pressure gradient computation a hydrostatic stress state variable was introduced with the following governing equation.

$$\delta W_{\sigma_h} = \int_\Omega \delta\sigma_h \left(\sigma_h - \frac{tr(\boldsymbol{\sigma})}{3}\right) d\Omega = 0 \tag{3.5}$$

σ_h and it's DOF derivatives can be directly used to compute the residual and jacobian contributions represented by the first term in (3.5). The stress tensor ($\boldsymbol{\sigma}$) and it's DOF derivatives already computed for the mechanics governing equation are used to integrate the residual and jacobian contributions represented by the second term in (3.5.

3.1.2 Small Deformation Binary Electrolyte Element

This element implementation is based on the small deformation formulation discussed in Section2.3.2, and designed for simulating non-flowing electrolytes. It operates on displacement ($\tilde{\mathbf{u}}$), ion concentration ($\tilde{c}$), and electric potential ($\tilde{\phi}$) DOFs. The

$\tilde{\mathbf{u}}$ DOFs are interpolated quadratically, and the $\tilde{c}$ and $\tilde{\phi}$ DOFs can be interpolated quadratically or linearly. At each integration point the element can directly compute the following quantities.

$$\begin{array}{cccccccc} \text{Var} & \mathbf{u} & c & \dot{c} & \phi & \boldsymbol{\varepsilon} & \nabla c & \nabla\phi \\ \frac{\partial(\text{Var})}{\partial *} & \frac{\partial \mathbf{u}}{\partial \tilde{\mathbf{u}}} & \frac{\partial c}{\partial \tilde{c}} & \frac{\partial \dot{c}}{\partial \tilde{c}} & \frac{\partial \phi}{\partial \tilde{\phi}} & \frac{\partial \boldsymbol{\varepsilon}}{\partial \tilde{\mathbf{u}}} & \frac{\partial(\nabla c)}{\partial \tilde{c}} & \frac{\partial(\nabla\phi)}{\partial \tilde{\phi}} \end{array} \tag{3.6}$$

All of the above variables are defined in the small deformation approximation discussions in chapter 2.

The mechanics governing equation is expressed in the weak form below.

$$\delta W_{\mathbf{u}} = -\int_{\Omega} \delta\boldsymbol{\varepsilon} : \boldsymbol{\sigma}\, d\Omega + \int_{\Gamma} \delta\mathbf{u}\ \cdot (\boldsymbol{\sigma}\cdot\mathbf{n})\, d\Gamma = 0 \tag{3.7}$$

$\boldsymbol{\varepsilon}$ and it's DOF derivatives are passed to the material model where they are used to compute $\boldsymbol{\sigma}$ and $\frac{\partial \boldsymbol{\sigma}}{\partial \tilde{\mathbf{u}}}$. The element uses the stress tensor ($\boldsymbol{\sigma}$) and it's derivatives to compute the resudial and jacobian contributions represented by the first integral in Equation (3.7). If provided a traction vector or surface pressure, they are integrated over the surface as represented by the second term in Equation (3.2). To integrate a surface traction vector the ($\boldsymbol{\sigma}\cdot\mathbf{n}$) term is replaced by the provided vector, and to integrate a surface pressure the ($\boldsymbol{\sigma}\cdot\mathbf{n}$) term is replaced by the provided pressure times the normal vector.

The ion diffusion governing equation is written in the weak form below.

$$\delta W_c = \int_{\Omega} (\delta c\dot{c} - \delta\nabla c\cdot\mathbf{j})\, d\Omega + \int_{\Gamma} \delta c\, \mathbf{j}\cdot\mathbf{n}\, d\Gamma = 0 \tag{3.8}$$

The first term in the first integral in Equation (3.8) is integrated directly without any assistance from the material model. ∇c and it's DOF derivatives are passed to the material model where they are used to compute $\mathbf{j}$, and $\frac{\partial \mathbf{j}}{\partial \tilde{c}}$. The element uses the flux vector ($\mathbf{j}$) and it's derivatives to compute the resudial and jacobian contributions represented by the second term in the first integral in the ion diffusion governing Equations (3.8). The second integral in Equation (3.8) represents the surface ion flux. If a surface

flux is provided it is integrated by replacing $(\mathbf{j} \cdot \mathbf{n})$ with the provided flux. Surface flux can also be computed with the BV equations by providing the material model with concentrations and voltages on both sides of the interface.

The electric potential governing equation written in the weak form is

$$\delta W_\phi = -\int_\Omega \delta\nabla\phi \cdot \mathbf{i}\, d\Omega + \int_\Gamma \delta\phi\, \mathbf{i} \cdot \mathbf{n}\, d\Gamma = 0 \tag{3.9}$$

c, ∇c, $\nabla\phi$ and their DOF derivatives are passed to the material model where they are used to compute $\mathbf{i}$, $\frac{\partial \mathbf{i}}{\partial \tilde{\phi}}$, and $\frac{\partial \mathbf{i}}{\partial \tilde{c}}$. The element uses the electric field vector $(\mathbf{i})$ and it's derivatives to compute the resudial and jacobian contributions represented by the first integral in the electric potential governing Equation (3.9). The second integral in Equation (3.9) represents the surface electric flux. If a surface flux is provided it is integrated by replacing $(\mathbf{i} \cdot \mathbf{n})$ with the provided flux. Surface electric flux can also be computed with the BV equations.

3.1.3 Finite Deformation Electrochemical-Mechanical Element

This element implementation is based on the finite deformation formulations, and designed for simulating coupled transport-mechanics in intercalation host materials and non-flowing electrolytes. It operates on displacement $(\tilde{\mathbf{u}})$, nominal species concentration $(\tilde{C})$, electric potential $(\tilde{\phi})$, and hydrostatic stress $(\tilde{\sigma}_h)$ DOFs. The $\tilde{\mathbf{u}}$ DOFs are interpolated quadratically, the $\tilde{C}$ and $\tilde{\phi}$ DOFs can be interpolated quadratically or linearly, and the $\tilde{\sigma}_h$ DOFs are interpolated linearly. The element also optionally uses linearly interpolated osmotic pressure $(\tilde{p}_o)$ DOFs if an incompressibility flag is set. At each integration point the element can directly compute the following quantities.

$$\begin{array}{cccccccccc} \text{Var} & \mathbf{u} & C & \dot{C} & \phi & \sigma_h & p_o & \mathbf{H} & \nabla^0 C & \nabla^0\phi & \nabla^0\sigma_h \\ \frac{\partial(\text{Var})}{\partial *} & \frac{\partial \mathbf{u}}{\partial \tilde{\mathbf{u}}} & \frac{\partial C}{\partial \tilde{C}} & \frac{\partial \dot{C}}{\partial \tilde{C}} & \frac{\partial \phi}{\partial \tilde{\phi}} & \frac{\partial \sigma_h}{\partial \tilde{\sigma}_h} & \frac{\partial p_o}{\partial \tilde{p}_o} & \frac{\partial \mathbf{H}}{\partial \tilde{\mathbf{u}}} & \frac{\partial(\nabla^0 C)}{\partial \tilde{C}} & \frac{\partial(\nabla^0\phi)}{\partial \tilde{\phi}} & \frac{\partial(\nabla^0\sigma_h)}{\partial \tilde{\sigma}_h} \end{array} \tag{3.10}$$

p_o is only computed if a incompressibility flag is set.

The mechanics governing equation is expressed in the weak form below.

$$\delta W_{\mathbf{u}} = -\int_{\Omega_0} \delta\mathbf{F}\colon \mathbf{P}\; d\Omega_0 + \int_{\Gamma} \delta\mathbf{u}\; \cdot (\mathbf{P}\cdot\mathbf{n}_0)\; d\Gamma_0 = 0 \tag{3.11}$$

C, $\mathbf{H}$, optionally p_o, and their DOF derivatives are passed to the material model where they are used to compute $\mathbf{P}$, $\frac{\partial \mathbf{P}}{\partial \tilde{\mathbf{u}}}$, $\frac{\partial \mathbf{P}}{\partial \tilde{C}}$, and optionally $\frac{\partial \mathbf{P}}{\partial \tilde{p}_o}$. The element uses the stress tensor ($\mathbf{P}$) and it's derivatives to compute the resudial and jacobian contributions represented by the first term in Equation (3.11). If provided a traction vector or surface pressure, they are integrated over the surface as represented by the second term in Equation (3.11). To integrate a surface traction vector the ($\mathbf{P}\cdot\mathbf{n}_0$) term is replaced by the provided vector, but if a surface pressure (p_s) is provided it is assumed to be a true not nominal pressure. Thus, the surface deformation must be accounted for in integrating the surface pressure using the equation below.

$$\mathbf{P}\cdot\mathbf{n}_0 = \mathbf{n}_0 \cdot \left(p_s J \mathbf{F}^{-1}\right) \tag{3.12}$$

The species diffusion governing equation is written in the weak form below.

$$\delta W_C = \int_{\Omega_0} \left(\delta C\dot{C} - \delta\nabla^0 C\cdot\mathbf{J}\right) d\Omega_0 + \int_{\Gamma_0} \delta C\; \mathbf{J}\cdot\mathbf{n}_0\; d\Gamma_0 = 0 \tag{3.13}$$

The first term in the first integral in Equation (3.13) is integrated directly without any assistance from the material model. C, ∇C, $\nabla\sigma_h$, $\mathbf{H}$, and their DOF derivatives are passed to the material model where they are used to compute $\mathbf{J}$, $\frac{\partial \mathbf{J}}{\partial \tilde{C}}$, $\frac{\partial \mathbf{J}}{\partial \tilde{\sigma}_h}$, and $\frac{\partial \mathbf{J}}{\partial \tilde{\mathbf{u}}}$. The element uses the nominal flux vector ($\mathbf{J}$) and it's derivatives to compute the resudial and jacobian contributions represented by the second term in the first integral in the species diffusion governing Equation (3.13). The second integral in Equation (3.13) represents the surface nominal species flux. If a nominal surface flux is provided it is integrated by replacing ($\mathbf{J}\cdot\mathbf{n}_0$) with the provided flux. Surface flux can also be computed with the BV equations by providing the material model with concentrations and voltages on both sides of the interface.

The electric potential governing equations written in the weak form are

$$\delta W_\phi = -\int_{\Omega_0} \delta\nabla^0\phi \cdot \mathbf{I}\, d\Omega_0 + \int_{\Gamma_0} \delta\phi\, \mathbf{I}\cdot\mathbf{n}_0\, d\Gamma_0 = 0 \tag{3.14}$$

C, ∇C, $\nabla\phi$, $\mathbf{H}$, and their DOF derivatives are passed to the material model where they are used to compute $\mathbf{I}$, $\frac{\partial \mathbf{I}}{\partial C}$, $\frac{\partial \mathbf{I}}{\partial \phi}$, and $\frac{\partial \mathbf{I}}{\partial \tilde{\mathbf{u}}}$. The element uses the Nominal electric field vector ($\mathbf{I}$) and it's derivatives to compute the residual and jacobian contributions represented by the first integral in the electric potential governing Equation (3.14). The second integral in Equation (3.14) represents the surface electric flux. If a surface flux is provided it is integrated by replacing ($\mathbf{I}\cdot\mathbf{n}_0$) with the provided flux. Surface electric flux can also be computed with the BV equations by providing the material model with concentrations and voltages on both sides of the interface.

Just as with the small deformation electrode particle element, this element is set up to accommodate stress assisted diffusion. This model is much more flexible in that in can accommodate the two different forms of stress assisted diffusion characterized by the TSEC and VSEC electrochemical-mechanical models. The small deformation electrode particle element uses a small deformation approximation of TSEC stress assisted diffusion. The hydrostatic stress σ_h DOFs are governed by the following equation.

$$\delta W_{\sigma_h} = \int_{\Omega_0} \delta\sigma_h\,(\sigma_h - p^*)\, d\Omega_0 = 0 \tag{3.15}$$

To facilitate using both TSEC and VSEC models the equation for p^* is determined by the material model. In either case C, $\mathbf{H}$, optionally p_o, and their DOF derivatives are passed to the material model where they are used to compute p^*, $\frac{\partial p^*}{\partial \tilde{\mathbf{u}}}$, $\frac{\partial p^*}{\partial C}$, and optionally $\frac{\partial p^*}{\partial p_o}$. If TSEC coupling is used $p^* = \frac{\boldsymbol{\sigma}:\mathbf{I}}{3}$, otherwise if VSEC coupling is used $p^* = \frac{\boldsymbol{\sigma}^{vol}:\mathbf{I}}{3}$, where $\boldsymbol{\sigma}^{vol}$ is the component of the cauchy stress associated with forced volume change. In the case of incompressibility $\boldsymbol{\sigma}^{vol} = p_o$.

In the incompressible formulation the osmotic pressure (p_o) is governed by the

following equation.

$$\delta W_{p_o} = \int_{\Omega_0} \delta p_o \left(J - 1 - \Omega C\right) d\Omega_0 = \int_{\Omega_0} \delta p_o \left(Icmp\right) d\Omega_0 \tag{3.16}$$

C, $\mathbf{H}$, and their DOF derivatives are passed to the material model where they are used to compute $Icmp$, $\frac{\partial Icmp}{\partial \tilde{\mathbf{u}}}$, and $\frac{\partial Icmp}{\partial \tilde{C}}$. The compressibility term and it's derivatives are then used to compute the residual and jacobian contributions represented by Equation (3.16). The finite deformation electrochemical-mechanical element can also integrate the small deformation approximation equations if a flag is specified. If the small deformation flag is specified the element will effectively evaluate the equations presented in Section3.1.1.

3.1.4 Finite Deformation Hydrogel Element

This element implementation is based on a formulation published in Zhang et al. [58], and designed for modeling water transport through incompressible hydrogels. It operates on displacement ($\tilde{\mathbf{u}}$) and chemical potential ($\tilde{\mu}_c$) DOFs. Both DOF types are interpolated with the same interpolators; linear and quadratic forms are implemented. At each integration point the element can directly compute the following quantities.

$$\begin{array}{cccccc} \text{Var} & \mathbf{u} & \mu_c & \mathbf{H} & \dot{\mathbf{H}} & \nabla^0 \mu_c \\ \frac{\partial(\text{Var})}{\partial *} & \frac{\partial \mathbf{u}}{\partial \tilde{\mathbf{u}}} & \frac{\partial \mu_c}{\partial \tilde{\mu}_c} & \frac{\partial \mathbf{H}}{\partial \tilde{\mathbf{u}}} & \frac{\partial \dot{\mathbf{H}}}{\partial \tilde{\mathbf{u}}} & \frac{\partial \left(\nabla^0 \mu_c\right)}{\partial \tilde{\mu}_c} \end{array} \tag{3.17}$$

The mechanics governing equation is expressed in the weak form below.

$$\delta W_{\mathbf{u}} = -\int_{\Omega_0} \delta \mathbf{F} \colon \mathbf{P} \; d\Omega_0 + \int_{\Gamma} \delta \mathbf{u} \; \cdot \left(\mathbf{P} \cdot \mathbf{n}_0\right) d\Gamma_0 = 0 \tag{3.18}$$

μ_c, $\mathbf{H}$, and their DOF derivatives are passed to the material model where they are used to compute $\mathbf{P}$, $\frac{\partial \mathbf{P}}{\partial \tilde{\mathbf{u}}}$, and $\frac{\partial \mathbf{P}}{\partial \tilde{\mu}_c}$. The element uses the stress tensor ($\mathbf{P}$) and it's derivatives to compute the resudial and jacobian contributions represented by the first term in Equation (3.18). If provided a traction vector or surface pressure, they are integrated over the surface as represented by the second term in Equation (3.18). To integrate a surface traction vector the $(\mathbf{P} \cdot \mathbf{n}_0)$ term is replaced by the provided vector, but if a

surface pressure (p_s) is provided it is assumed to be a true not nominal pressure. Thus, the surface deformation must be accounted for in integrating the surface pressure using the equation below.

$$\mathbf{P} \cdot \mathbf{n}_0 = \mathbf{n}_0 \cdot \left(p_s J \mathbf{F}^{-1} \right) \tag{3.19}$$

The water diffusion governing equations are written in the weak form below.

$$\delta W_\mu = \int_{\Omega_0} \left(\delta \mu_c \dot{C} - \delta \nabla^0 \mu_c \cdot \mathbf{J} \right) d\Omega_0 + \int_{\Gamma_0} \delta \mu_c \, \mathbf{J} \cdot \mathbf{n}_0 \, d\Gamma_0 = 0 \tag{3.20}$$

Because C is not a DOF variable the element can not directly compute $\dot{C}$. Instead $\mathbf{H}$, $\dot{\mathbf{H}}$, and their DOF derivatives are passed to the material model where they are used to compute $\dot{C}$, $\frac{\partial \dot{C}}{\partial \tilde{\mathbf{u}}}$, and $\frac{\partial \dot{C}}{\partial \dot{\tilde{\mathbf{u}}}}$. The element uses the nominal concentration rate ($\dot{C}$) and it's derivatives to compute the resudial and jacobian contributions represented by the first term in the first integral in Equation (3.20). $\nabla^0 \mu_c$, $\mathbf{H}$, and their DOF derivatives are passed to the material model where they are used to compute $\mathbf{J}$, $\frac{\partial \mathbf{J}}{\partial \tilde{\mu_c}}$, and $\frac{\partial \mathbf{J}}{\partial \tilde{\mathbf{u}}}$. The element uses the nominal flux vector ($\mathbf{J}$) and it's derivatives to compute the resudial and jacobian contributions represented by the second term in the first integral in the water diffusion governing Equation (3.20). The second integral in Equation (3.13) represents the surface nominal species flux. If a nominal surface flux is provided it is integrated by replacing ($\mathbf{J} \cdot \mathbf{n}_0$) with the provided flux.

3.2 Material Models

The material models are responsible for storing and evaluating material properties, and evaluating constitutive equations provided state information from an element. The different models that have been implemented are presented in the context of the constitutive equations they evaluate. In each material model description the elements that it can pair with are noted.

3.2.1 Small Deformation Electrode Particle Material Model

This material model pairs with the small deformation electrode particle element only. It is responsible for computing linear elastic stresses ($\boldsymbol{\sigma}$), species fluxes ($\mathbf{j}$), electric fields ($\mathbf{i}$), and their derivatives with respect to the DOFs. The equations used to compute the linear elastic stresses ($\boldsymbol{\sigma}$) and their derivatives with respect to $\tilde{\mathbf{u}}$ and $\tilde{c}$ are listed below.

$$\begin{array}{ccc} \text{Equation} & \frac{\partial \text{Equation}}{\partial \tilde{\mathbf{u}}} & \frac{\partial \text{Equation}}{\partial \tilde{c}} \\ \boldsymbol{\varepsilon}^c = \frac{\Omega}{3} c & 0 & \frac{\Omega}{3}\frac{\partial c}{\partial \tilde{c}} \\ \boldsymbol{\varepsilon}^e = \boldsymbol{\varepsilon} - \boldsymbol{\varepsilon}^c & \frac{\partial \boldsymbol{\varepsilon}}{\partial \tilde{\mathbf{u}}} & -\frac{\partial \boldsymbol{\varepsilon}^c}{\partial \tilde{c}} \\ \boldsymbol{\sigma} = \underline{\mathbf{C}} : \boldsymbol{\varepsilon}^e & \mathbf{C} : \frac{\partial \boldsymbol{\varepsilon}^e}{\partial \tilde{\mathbf{u}}} & \underline{\mathbf{C}} : \frac{\partial \boldsymbol{\varepsilon}^e}{\partial \tilde{c}} \end{array} \tag{3.21}$$

The equations used to compute the species flux ($\mathbf{j}$) and it's derivatives with respect to $\tilde{c}$ and $\tilde{\sigma}_h$ are listed below.

$$\begin{array}{ccc} \text{Equation} & \frac{\partial \text{Equation}}{\partial \tilde{c}} & \frac{\partial \text{Equation}}{\partial \tilde{\sigma}_h} \\ \mathbf{j}_c = -D\nabla c & -D\frac{\partial(\nabla c)}{\partial \tilde{c}} & 0 \\ \mathbf{j}_\sigma = M\Omega c \nabla \sigma_h & M\Omega \nabla \sigma_h \frac{\partial c}{\partial \tilde{c}} & M\Omega c \frac{\partial(\nabla \sigma_h)}{\partial \tilde{\sigma}_h} \\ \mathbf{j} = \mathbf{j}_c + \mathbf{j}_\sigma & \frac{\partial \mathbf{j}_c}{\partial \tilde{c}} + \frac{\partial \mathbf{j}_\sigma}{\partial \tilde{c}} & \frac{\partial \mathbf{j}_\sigma}{\partial \tilde{\sigma}_h} \end{array} \tag{3.22}$$

The equations used to compute the electric field ($\mathbf{i}$) and it's derivatives with respect to $\tilde{\psi}$ are listed below.

$$\begin{array}{cc} \text{Equation} & \frac{\partial \text{Equation}}{\partial \tilde{\phi}} \\ \mathbf{i} = k\nabla\phi & k\frac{\partial(\nabla\phi)}{\partial \tilde{\phi}} \end{array} \tag{3.23}$$

3.2.2 Small Deformation Binary Electrolyte Material Model

This material model pairs with the small deformation binary electrolyte element only. It is responsible for computing linear elastic stresses ($\boldsymbol{\sigma}$), ion fluxes ($\mathbf{j}$), electric fields ($\mathbf{i}$), and their derivatives with respect to the DOFs. The equations used to compute

the linear elastic stresses ($\boldsymbol{\sigma}$) and their derivatives with respect to $\tilde{\mathbf{u}}$ are listed below.

$$\begin{array}{cc} \text{Equation} & \frac{\partial \text{Equation}}{\partial \tilde{\mathbf{u}}} \\ \boldsymbol{\sigma} = \mathbf{C} : \boldsymbol{\varepsilon} & \mathbf{C} : \frac{\partial \boldsymbol{\varepsilon}}{\partial \tilde{\mathbf{u}}} \end{array} \tag{3.24}$$

The equations used to compute the ion flux ($\mathbf{j}$) and it's derivatives with respect to $\tilde{c}$ are listed below.

$$\begin{array}{cc} \text{Equation} & \frac{\partial \text{Equation}}{\partial \tilde{c}} \\ \mathbf{j} = -D_p \nabla c & -D \frac{\partial (\nabla c)}{\partial \tilde{c}} \end{array} \tag{3.25}$$

The equations used to compute the electric field ($\mathbf{i}$) and it's derivatives with respect to $\tilde{c}$ and$\tilde{\psi}$ are listed below.

$$\begin{array}{ccc} \text{Equation} & \frac{\partial \text{Equation}}{\partial \tilde{c}} & \frac{\partial \text{Equation}}{\partial \tilde{\sigma}_h} \\ \mathbf{i}_c = -\left(D_+ - D_-\right) \nabla c & -\left(D_+ - D_+\right) \frac{\partial (\nabla c)}{\partial \tilde{c}} & 0 \\ \mathbf{i}_\phi = -\left(D_+ + D_-\right) \frac{zF^2 c}{R_g T} \nabla \phi & -\left(D_+ + D_-\right) \frac{zF^2}{R_g T} \nabla \phi \frac{\partial c}{\partial \tilde{c}} & -\left(D_+ + D_-\right) \frac{zF^2 c}{R_g T} \frac{\partial (\nabla \phi)}{\partial \tilde{\phi}} \\ \mathbf{i} = \mathbf{i}_c + \mathbf{i}_\phi & \frac{\partial \mathbf{i}_c}{\partial \tilde{c}} + \frac{\partial \mathbf{i}_\phi}{\partial \tilde{c}} & \frac{\partial \mathbf{i}_\phi}{\partial \tilde{\phi}} \end{array} \tag{3.26}$$

3.2.3 Hyperelastic Material Model

This material model pairs with the finite deformation electrochemical-mechanical element as the mechanics part of the material model, and the finite deformation total Lagrangian structural element. It is responsible for computing Nominal and Cauchy stress tensors ($\mathbf{P}$ and $\boldsymbol{\sigma}$), the coupling pressure (p^*), and optionally the compression measure ($Icmp$). Compressible and incompressible non-swelling, TSEC, and VSEC formulations of this model have been implemented and are described below. In all six formulations the PK2 tensor ($\mathbf{S}$) is computed, and then it is transformed into either the specified stress tensor and returned to the calling element. Everything computed by the hyperelastic material models is a function of the deformation gradient ($\mathbf{F}$), osmotic pressure (p_o) for incompressible formulations, and nominal concentration (C) for swelling formulations, so all of the derivatives are computed with respect to $\mathbf{F}$, C, and

p_o. Then chain rule is used to compute the derivatives of a specified stress or strain tensor with respect to DOFs.

$$\begin{aligned}\frac{\partial \mathbf{T}}{\partial \tilde{\mathbf{u}}} &= \frac{\partial \mathbf{T}}{\partial \mathbf{F}} : \frac{\partial \mathbf{F}}{\partial \tilde{\mathbf{u}}} \\ \frac{\partial \mathbf{T}}{\partial \tilde{p}_o} &= \frac{\partial \mathbf{T}}{\partial p_o}\frac{\partial p_o}{\partial \tilde{p}_o} \\ \frac{\partial \mathbf{T}}{\partial \tilde{C}} &= \frac{\partial \mathbf{T}}{\partial C}\frac{\partial C}{\partial \tilde{C}}\end{aligned} \tag{3.27}$$

where $\mathbf{T}$ represents the specified tensor. All of the different formulations start by evaluating the following equations.

$$\begin{array}{cc} \text{Equation} & \frac{\partial \text{Equation}}{\partial \mathbf{F}} \\ J = \det(\mathbf{F}) & J\mathbf{F}^{-T} \\ \mathbf{C} = \mathbf{F}^T\mathbf{F} & \frac{\partial \mathbf{F}^T}{\partial \mathbf{F}}\mathbf{F} + \mathbf{F}^T\frac{\partial \mathbf{F}}{\partial \mathbf{F}} \end{array} \tag{3.28}$$

Starting with the compressible non-swelling formulation, the equations for computing $\mathbf{S}$ are listed below.

$$\begin{array}{cc} \text{Equation} & \frac{\partial \text{Equation}}{\partial \mathbf{F}} \\ \mathbf{S}^{iso} = \frac{\partial \Psi^{iso}}{\partial \mathbf{C}} & \frac{\partial^2 \Psi^{iso}}{\partial \mathbf{C}^2} : \frac{\partial \mathbf{C}}{\partial \mathbf{F}} \\ \mathbf{S}^{vol} = \frac{\partial \Psi^{vol}}{\partial \mathbf{C}} & \frac{\partial^2 \Psi^{iso}}{\partial \mathbf{C}^2} : \frac{\partial \mathbf{C}}{\partial \mathbf{F}} \\ \mathbf{S} = \mathbf{S}^{iso} + \mathbf{S}^{vol} & \frac{\partial \mathbf{S}^{iso}}{\partial \mathbf{F}} + \frac{\partial \mathbf{S}^{vol}}{\partial \mathbf{F}} \end{array} \tag{3.29}$$

The non-swelling incompressible equations for computing $\mathbf{S}$ are listed below.

$$\begin{array}{ccc} \text{Equation} & \frac{\partial \text{Equation}}{\partial \mathbf{F}} & \frac{\partial \text{Equation}}{\partial p_o} \\ \mathbf{S}^{iso} = \frac{\partial \Psi^{iso}}{\partial \mathbf{C}} & \frac{\partial^2 \Psi^{iso}}{\partial \mathbf{C}^2} : \frac{\partial \mathbf{C}}{\partial \mathbf{F}} & 0 \\ \mathbf{S}^{vol} = p_0 J\mathbf{C}^{-1} & p_0\left(\frac{\partial J}{\partial \mathbf{F}} \otimes \mathbf{C}^{-1} + J\frac{\partial \mathbf{C}^{-1}}{\partial \mathbf{F}}\right) & J\mathbf{F}^T \\ \mathbf{S} = \mathbf{S}^{iso} + \mathbf{S}^{vol} & \frac{\partial \mathbf{S}^{iso}}{\partial \mathbf{F}} + \frac{\partial \mathbf{S}^{vol}}{\partial \mathbf{F}} & \frac{\partial \mathbf{S}^{vol}}{\partial p_0} \end{array} \tag{3.30}$$

All of the different swelling formulations evaluate the following equations.

$$\begin{array}{ccc} \text{Equation} & \frac{\partial \text{Equation}}{\partial \mathbf{F}} & \frac{\partial \text{Equation}}{\partial C} \\ J^C = 1 + \Omega C & 0 & \Omega \\ J^e = \left(J^C\right)^{-1} J & \left(J^C\right)^{-1} J \mathbf{F}^{-T} & -\left(J^C\right)^{-1} J \frac{\partial J^C}{\partial C} \\ \mathbf{F}^{-C} = \left(J^C\right)^{-1/3} \mathbf{I} & 0 & -\frac{1}{3}\left(J^C\right)^{-4/3} \mathbf{I} \\ \mathbf{F}^e = \mathbf{F}^{-C} \mathbf{F} & \mathbf{F}^{-C} \frac{\partial \mathbf{F}}{\partial \mathbf{F}} & \frac{\partial \left(\mathbf{F}^{-C}\right)}{\partial C} \mathbf{F} \\ \mathbf{C}^e = \mathbf{F}^{eT} \mathbf{F}^e & \frac{\partial \mathbf{F}^{eT}}{\partial \mathbf{F}} \mathbf{F}^e + \mathbf{F}^{eT} \frac{\partial \mathbf{F}^e}{\partial \mathbf{F}} & \frac{\partial \mathbf{F}^{eT}}{\partial C} \mathbf{F}^e + \mathbf{F}^{eT} \frac{\partial \mathbf{F}^e}{\partial C} \end{array} \tag{3.31}$$

The TSEC compressible equations for computing $\mathbf{S}$ are listed below.

$$\begin{array}{ccc} \text{Equation} & \frac{\partial \text{Equation}}{\partial \mathbf{F}} & \frac{\partial \text{Equation}}{\partial C} \\ \mathbf{S}^{eiso} = \frac{\partial \Psi^{eiso}}{\partial \mathbf{C}^e} & \frac{\partial^2 \Psi^{eiso}}{\partial \mathbf{C}^{e2}} : \frac{\partial \mathbf{C}^e}{\partial \mathbf{F}} & \frac{\partial^2 \Psi^{eiso}}{\partial \mathbf{C}^{e2}} : \frac{\partial \mathbf{C}^e}{\partial C} \\ \mathbf{S}^{evol} = \frac{\partial \Psi^{evol}}{\partial \mathbf{C}^e} & \frac{\partial^2 \Psi^{evol}}{\partial \mathbf{C}^{e2}} : \frac{\partial \mathbf{C}^e}{\partial \mathbf{F}} & \frac{\partial^2 \Psi^{evol}}{\partial \mathbf{C}^{e2}} : \frac{\partial \mathbf{C}^e}{\partial C} \\ \mathbf{S}^e = \mathbf{S}^{eiso} + \mathbf{S}^{evol} & \frac{\partial \mathbf{S}^{eiso}}{\partial \mathbf{F}} + \frac{\partial \mathbf{S}^{evol}}{\partial \mathbf{F}} & \frac{\partial \mathbf{S}^{evol}}{\partial C} \\ \mathbf{S} = J^C \mathbf{F}^{-C} \mathbf{S}^e \mathbf{F}^{-CT} = \left(J^C\right)^{1/3} \mathbf{S}^e & \left(J^C\right)^{1/3} \frac{\partial \mathbf{S}^e}{\partial \mathbf{F}} & \frac{-\left(J^C\right)^{-2/3}}{3} \frac{\partial J^C}{\partial C} \mathbf{S}^e + \left(J^C\right)^{1/3} \frac{\partial \mathbf{S}^e}{\partial C} \end{array} \tag{3.32}$$

The TSEC incompressible equations for computing $\mathbf{S}$ are listed below.

$$\begin{array}{cc} \text{Equation} & \frac{\partial \text{Equation}}{\partial \mathbf{F}} \\ \mathbf{S}^{eiso} = \frac{\partial \Psi^{eiso}}{\partial \mathbf{C}^e} & \frac{\partial^2 \Psi^{eiso}}{\partial \mathbf{C}^{e2}} : \frac{\partial \mathbf{C}^e}{\partial \mathbf{F}} \\ \mathbf{S}^{iso} = \left(J^C\right)^{1/3} \mathbf{S}^{eiso} & \left(J^C\right)^{1/3} \frac{\partial \mathbf{S}^{eiso}}{\partial \mathbf{F}} \\ \mathbf{S} = \mathbf{S}^{iso} + J \mathbf{C}^{-1} p_0 & \frac{\partial \mathbf{S}^{eiso}}{\partial \mathbf{F}} + \left(\frac{\partial J}{\partial \mathbf{F}} \mathbf{C}^{-1} + J \frac{\partial \mathbf{C}^{-1}}{\partial \mathbf{F}}\right) p_0 \end{array} \tag{3.33}$$

$$\begin{array}{cc} \frac{\partial \text{Equation}}{\partial C} & \frac{\partial \text{Equation}}{\partial p_o} \\ \frac{\partial^2 \Psi^{eiso}}{\partial \mathbf{C}^{e2}} : \frac{\partial \mathbf{C}^e}{\partial C} & 0 \\ \frac{-\left(J^C\right)^{-2/3}}{3} \frac{\partial J^C}{\partial C} \mathbf{S}^{eiso} + \left(J^C\right)^{1/3} \frac{\partial \mathbf{S}^{eiso}}{\partial C} & 0 \\ \frac{\partial \mathbf{S}^{eiso}}{\partial C} & J \mathbf{C}^{-1} \end{array}$$

The VSEC compressible equations for computing $\mathbf{S}$ are listed below.

$$\begin{array}{lll} \text{Equation} & \frac{\partial \text{Equation}}{\partial \mathbf{F}} & \frac{\partial \text{Equation}}{\partial C} \\ \mathbf{S}^{iso} = \frac{\partial \Psi^{iso}}{\partial \mathbf{C}} & \frac{\partial^2 \Psi^{iso}}{\partial \mathbf{C}^2} : \frac{\partial \mathbf{C}}{\partial \mathbf{F}} & 0 \\ \mathbf{S}^{vol} = \frac{\partial \Psi^{vol}}{\partial \mathbf{C}} & \frac{\partial^2 \Psi^{vol}}{\partial \mathbf{C}^2} : \frac{\partial \mathbf{C}}{\partial \mathbf{F}} & \frac{\partial^2 \Psi^{vol}}{\partial C \partial \mathbf{C}} \\ \mathbf{S} = \mathbf{S}^{iso} + \mathbf{S}^{vol} & \frac{\partial \mathbf{S}^{iso}}{\partial \mathbf{F}} + \frac{\partial \mathbf{S}^{vol}}{\partial \mathbf{F}} & \frac{\partial \mathbf{S}^{vol}}{\partial C} \end{array} \tag{3.34}$$

The VSEC incompressible equations for computing $\mathbf{S}$ are identical to the non-swelling equations presented in Equation set (3.30). To minimize redundancy they are not listed again.

Algorithms for computing the PK2 stress tensor have been implemented for all of the strain energy models described in the appendix. With the PK2 stress tensor, it's derivatives, and the transformation rules listed in Table 8.1 the Nominal or Cauchy stress tensors and their derivatives are computed as specified below.

$$\begin{array}{lll} \text{Equation} & \frac{\partial \text{Equation}}{\partial \mathbf{F}} & \frac{\partial \text{Equation}}{\partial *} \\ \mathbf{P} = \mathbf{F}\mathbf{S} & \frac{\partial \mathbf{F}}{\partial \mathbf{F}}\mathbf{S} + \mathbf{F}\frac{\partial \mathbf{S}}{\partial \mathbf{F}} & \mathbf{F}\frac{\partial \mathbf{S}}{\partial *} \\ \boldsymbol{\sigma} = J^{-1}\mathbf{P}\mathbf{F}^T & J^{-1}\left(-J^{-1}\frac{\partial J}{\partial \mathbf{F}}\mathbf{P}\mathbf{F}^T + J^{-1}\frac{\partial \mathbf{P}}{\partial \mathbf{F}}\mathbf{F}^T + J^{-1}\mathbf{P}\frac{\partial \mathbf{F}^T}{\partial \mathbf{F}}\right) & J^{-1}\frac{\partial \mathbf{P}}{\partial *}\mathbf{F}^T \end{array} \tag{3.35}$$

$*$ represents either C or p_o. With all the pieces in place derivatives with respect to the DOFs are computed with the equations listed in Equation set (3.27).

If one of the swelling formulations are being used this model is also responsible for computing the coupling pressure (p^*). In the case of the TSEC models, p^* and it's derivatives are computed with the following equations.

$$\begin{array}{lll} \text{Equation} & \frac{\partial \text{Equation}}{\partial \tilde{\mathbf{u}}} & \frac{\partial \text{Equation}}{\partial \tilde{*}} \\ p^* = \frac{1}{3}\boldsymbol{\sigma} : \mathbf{I} & \frac{1}{3}\frac{\partial \boldsymbol{\sigma}}{\partial \tilde{\mathbf{u}}} : \mathbf{I} & \frac{1}{3}\frac{\partial \boldsymbol{\sigma}}{\partial \tilde{*}} : \mathbf{I} \end{array} \tag{3.36}$$

In the case of the VSEC models, p^* is the mean of the volumetric component of the Cauchy stress tensor ($\boldsymbol{\sigma}^{vol}$) instead of being the mean of the total Cauchy stress tensor ($\boldsymbol{\sigma}$). $\boldsymbol{\sigma}^{vol}$ and it's derivatives with respect to $\mathbf{F}$ and $*$ are computed by replacing $\mathbf{S}$ and it's derivatives in Equation set (3.35) with $\mathbf{S}^{\mathbf{vol}}$ and it's derivatives. p^* and it's

derivatives can then be computed by using $\boldsymbol{\sigma}^{vol}$ and it's derivatives with Equation set (3.36)

The compressible formulations are also responsible for computing the incompressibility term ($Icmp$) defined in Equation (3.16). $Icmp$ and it's derivatives with respect to the DOFs are computed with the following equations.

$$\begin{array}{ccc} \text{Equation} & \frac{\partial \text{Equation}}{\partial \tilde{\mathbf{u}}} & \frac{\partial \text{Equation}}{\partial \tilde{C}} \\ J & \frac{\partial J}{\partial \mathbf{F}} : \frac{\partial \mathbf{F}}{\partial \tilde{\mathbf{u}}} & 0 \\ Icmp = J - 1 - \Omega C & \frac{\partial J}{\partial \tilde{\mathbf{u}}} & -\Omega \frac{\partial C}{\partial \tilde{C}} \end{array} \tag{3.37}$$

3.2.4 Pseudo Finite Deformation Species Transport Material Model

This material model pairs with the finite deformation electrochemical-mechanical element as the deformation independent component of the species transport model only. It is responsible for computing chemical potentials, pseudo nominal species fluxes, and pseudo nominal electric fields. Models based on the chemical potentials in the appendix have been implemented. This model computes the deformation independent parts of the nominal flux and electric field ($\mathbf{J}$, $\mathbf{I}$). $\mathbf{J}_{di}$ and $\mathbf{I}_{di}$ will be used to represent the deformation independent pieces of the nominal flux and electric field respectively. The equations for computing $\mathbf{J}_{di}$ and it's derivatives with respect to the DOFs are presented below.

$$\begin{array}{ccc} \text{Equation} & \frac{\partial \text{Equation}}{\partial \tilde{C}} & \frac{\partial \text{Equation}}{\partial \tilde{\sigma}_h} \\ \xi_C = MC\frac{\partial \mu_c}{\partial C} & M\left(\frac{\partial \mu_c}{\partial C} + C\frac{\partial^2 \mu_c}{\partial C^2}\right)\frac{\partial C}{\partial \tilde{C}} & 0 \\ \mathbf{J}_{dic} = -\xi_C \nabla^0 C & -\left(\frac{\partial \xi_C}{\partial \tilde{C}}\nabla^0 C + \xi_C \frac{\partial (\nabla^0 C)}{\partial \tilde{C}}\right) & 0 \\ \mathbf{J}_{di\sigma} = M\Omega C \nabla^0 \sigma_h & M\Omega \nabla^0 \sigma_h \frac{\partial C}{\partial \tilde{C}} & M\Omega C \frac{\partial (\nabla \sigma_h)}{\partial \tilde{\sigma}_h} \\ \mathbf{J}_{di} = \mathbf{J}_{dic} + \mathbf{J}_{di\sigma} & \frac{\partial \mathbf{J}_{dic}}{\partial \tilde{C}} & \frac{\partial \mathbf{J}_{di\sigma}}{\partial \tilde{\sigma}_h} \end{array} \tag{3.38}$$

The equations for computing $\mathbf{I}_{di}$ and it's derivatives with respect to the DOFs are presented below.

$$\begin{array}{cc} \text{Equation} & \frac{\partial \text{Equation}}{\partial \tilde{\phi}} \\ \mathbf{I}_{di} = k\nabla^0\phi & k\frac{\partial\left(\nabla^0\phi\right)}{\partial\tilde{\phi}} \end{array} \tag{3.39}$$

This model is designed for simulating swelling intercalation electrode host materials as described in Section2.3.1.

3.2.5 Pseudo Finite Deformation Ion Transport Material Model

This material model pairs with the finite deformation electrochemical-mechanical element as part of the ion transport model only. It is responsible for computing chemical potentials, pseudo nominal species fluxes, and pseudo nominal electric fields. Models based on the chemical potentials in the appendix have been implemented. This model computes the deformation independent parts of the nominal flux and electric field ($\mathbf{J}$, $\mathbf{I}$). $\mathbf{J}_di$ and $\mathbf{I}_di$ will be used to represent the deformation independent pieces of the nominal pseudo-flux and pseudo-electric field respectively. The equations for computing $\mathbf{J}_di$ and it's derivatives with respect to the DOFs are presented below.

$$\begin{array}{cc} \text{Equation} & \frac{\partial \text{Equation}}{\partial \tilde{C}} \\ \xi_C = \frac{D_p C}{R_g T}\frac{\partial \mu_c}{\partial C} & \frac{D_p}{R_g T}\left(\frac{\partial \mu_c}{\partial C} + C\frac{\partial^2 \mu_c}{\partial C^2}\right)\frac{\partial C}{\partial \tilde{C}} \\ \mathbf{J}_{di} = -\xi_C \nabla^0 C & -\left(\frac{\partial \xi_C}{\partial \tilde{C}}\nabla^0 C + \xi_C \frac{\partial\left(\nabla^0 C\right)}{\partial \tilde{C}}\right) \end{array} \tag{3.40}$$

The equations for computing $\mathbf{I}_di$ and it's derivatives with respect to the DOFs are presented below.

$$\begin{array}{ccc} \text{Equation} & \frac{\partial \text{Equation}}{\partial \tilde{C}} & \frac{\partial \text{Equation}}{\partial \tilde{\phi}} \\ \xi_C = \left(D_+ - D_-\right)\frac{FC}{RT}\frac{\partial \mu_c}{\partial C} & \left(D_+ - D_-\right)\frac{F}{RT}\left(\frac{\partial \mu_c}{\partial C} + C\frac{\partial^2 \mu_c}{\partial C^2}\right)\frac{\partial C}{\partial \tilde{C}} & 0 \\ \xi_\phi = \left(D_+ + D_-\right) z\frac{F^2 C}{RT} & \left(D_+ + D_-\right) z\frac{F^2}{RT}\frac{\partial C}{\partial \tilde{C}} & 0 \\ \mathbf{I}_{dic} = -\xi_C \nabla^0 C & -\left(\frac{\partial \xi_C}{\partial \tilde{C}}\nabla^0 C + \xi_C \frac{\partial\left(\nabla^0 C\right)}{\partial \tilde{C}}\right) & 0 \\ \mathbf{I}_{di\phi} = -\xi_\phi \nabla^0 \phi & -\frac{\partial \xi_\phi}{\partial C}\nabla^0\phi & -\xi_\phi \frac{\partial\left(\nabla^0\phi\right)}{\partial\tilde{\phi}} \\ \mathbf{I}_{di} = \mathbf{I}_{dic} + \mathbf{I}_{di\phi} & \frac{\partial \mathbf{I}_{dic}}{\partial \tilde{C}} & \frac{\partial \mathbf{I}_{di\phi}}{\partial \tilde{\phi}} \end{array} \tag{3.41}$$

This model is designed for simulating binary electro-neutral electrolytes as described in Section2.3.2.

3.2.6 Finite Deformation Species Transport Coupled Material Model

This material model couples a mechanics model described in Section3.2.3 and a pseudo finite deformation transport model described in Section3.2.4, and is responsible for computing all quantities required by the finite deformation electrochemical-mechanical element described in Section3.1.3. It is designed for simulating finitely deforming intercalation electrode host materials. The nominal stress tensor ($\mathbf{P}$), the coupling pressure (p^*), optionally the compression measure ($Icmp$) defined in Equation set (3.37), and their derivatives are computed directly with the mechanics model. The pseudo finite deformation transport model computes the deformation independent pieces of the nominal flux ($\mathbf{J}_{di}$) using Equation set (3.38), then getting the required mechanics pieces from the mechanics model the nominal species flux ($\mathbf{J}$) and it's derivatives are computed with the following equations.

$$\begin{array}{ccccc} \text{Equation} & \frac{\partial \text{Equation}}{\partial \tilde{\mathbf{u}}} & \frac{\partial \text{Equation}}{\partial \tilde{C}} & \frac{\partial \text{Equation}}{\partial \tilde{\sigma}_h} \\ \mathbf{C}^{-1} & \frac{\partial \mathbf{C}^{-1}}{\partial \mathbf{F}} : \frac{\partial \mathbf{F}}{\partial \tilde{\mathbf{u}}} & 0 & 0 \\ \mathbf{J} = \mathbf{C}^{-1}\mathbf{J}_{di} & \frac{\partial \mathbf{C}^{-1}}{\partial \tilde{\mathbf{u}}}\mathbf{J}_{di} & \mathbf{C}^{-1}\frac{\partial \mathbf{J}_{di}}{\partial \tilde{C}} & \mathbf{C}^{-1}\frac{\partial \mathbf{J}_{di}}{\partial \tilde{\sigma}_h} \end{array} \tag{3.42}$$

Assembling pieces from the two materials in a similar way, the nominal electric field ($\mathbf{I}$) and its derivatives are computed with the following equations.

$$\begin{array}{ccc} \text{Equation} & \frac{\partial \text{Equation}}{\partial \tilde{\mathbf{u}}} & \frac{\partial \text{Equation}}{\partial \tilde{\phi}} \\ J & J\mathbf{F}^{-T} : \frac{\partial \mathbf{F}}{\partial \tilde{\mathbf{u}}} & 0 \\ \mathbf{I} = J\mathbf{C}^{-1}\mathbf{I}_{di} & \left(J\frac{\partial \mathbf{C}^{-1}}{\partial \tilde{\mathbf{u}}} + \frac{\partial J}{\partial \tilde{\mathbf{u}}}\mathbf{C}^{-1}\right)\mathbf{I}_{di} & J\mathbf{C}^{-1}\frac{\partial \mathbf{I}_{di}}{\partial \tilde{C}} \end{array} \tag{3.43}$$

3.2.7 Finite Deformation Ion Transport Coupled Material Model

This material model couples a mechanics model described in Section3.2.3 and a pseudo finite deformation transport model described in Section3.2.5, and is respon-

sible for computing all quantities required by the finite deformation electrochemical-mechanical element described in Section3.1.3. It is designed for simulating finitely deforming non-flowing electrolytes. The nominal stress tensor ($\mathbf{P}$), optionally the compression measure ($Icmp$), and their derivatives are computed directly with the mechanics model. The pseudo finite deformation transport model computes the deformation independent pieces of the nominal flux ($\mathbf{J}_{di}$) using Equation set (3.40), then getting the required mechanics pieces from the mechanics model the nominal ion flux ($\mathbf{J}$) and it's derivatives are computed with the following equations.

$$\begin{array}{ccc} \text{Equation} & \frac{\partial \text{Equation}}{\partial \tilde{\mathbf{u}}} & \frac{\partial \text{Equation}}{\partial \tilde{C}} \\ \mathbf{C}^{-1} & \frac{\partial \mathbf{C}^{-1}}{\partial \mathbf{F}} : \frac{\partial \mathbf{F}}{\partial \tilde{\mathbf{u}}} & 0 \\ \mathbf{J} = \mathbf{C}^{-1}\mathbf{J}_{di} & \frac{\partial \mathbf{C}^{-1}}{\partial \tilde{\mathbf{u}}}\mathbf{J}_{di} & \mathbf{C}^{-1}\frac{\partial \mathbf{J}_{di}}{\partial \tilde{C}} \end{array} \tag{3.44}$$

Assembling pieces from the two materials in a similar way, the nominal electric field ($\mathbf{I}$) and its derivatives are computed with the following equations.

$$\begin{array}{cccc} \text{Equation} & \frac{\partial \text{Equation}}{\partial \tilde{\mathbf{u}}} & \frac{\partial \text{Equation}}{\partial \tilde{C}} & \frac{\partial \text{Equation}}{\partial \tilde{\phi}} \\ \mathbf{I} = \mathbf{C}^{-1}\mathbf{I}_{di} & \frac{\partial \mathbf{C}^{-1}}{\partial \tilde{\mathbf{u}}}\mathbf{I}_{di} & \mathbf{C}^{-1}\frac{\partial \mathbf{I}_{di}}{\partial \tilde{C}} & \mathbf{C}^{-1}\frac{\partial \mathbf{I}_{di}}{\partial \tilde{\phi}} \end{array} \tag{3.45}$$

3.2.8 Finite Deformation Hydrogel Material Model

This material model pairs with the finite deformation hydrogel element only. This Hydrogel model is based on an incompressible model developed by Zhang et al. [58]. It is responsible for computing the nominal stress tensor ($\mathbf{P}$), the nominal species flux vector ($\mathbf{J}$), and the nominal species concentration rate of change with respect to time ($\frac{\partial C}{\partial t} = \dot{C}$). The nominal stress tensor equation is based on the following free energy function taken from Zhang et al. [58].

$$\begin{array}{rl} \Psi\left(\mathbf{F}, J, \mu_c\right) = & -\frac{R_g T}{\Omega}\left[(J-1)\ln\left(\frac{J}{J-1}\right) + \frac{\chi}{J}\right] - \frac{\mu_c}{\Omega}(J-1) \\ & +\frac{\mu_0}{2}\left[\mathbf{F}:\mathbf{F} - 3 - 2\ln(J)\right] \end{array} \tag{3.46}$$

Based on the above free energy function the nominal stress tensor and it's derivatives are computed with the following formulas.

$$
\begin{aligned}
\mathbf{F} &= \mathbf{H} + \delta \\
J &= \det \mathbf{F} \\
\mathbf{P} = \frac{\partial \Psi}{\partial \mathbf{F}} &= \mu_0 \left[\delta - \mathbf{F}^{-T}\right] - \frac{1}{\Omega}\left[R_g T\left(J \ln\left[\frac{J}{J-1}\right] - 1 - \frac{\chi}{J}\right) + \mu_c J\right]\mathbf{F}^{-T} \\
\frac{\partial \mathbf{F}}{\partial \tilde{\mathbf{u}}} &= \frac{\partial \mathbf{H}}{\partial \tilde{\mathbf{u}}} \\
\frac{\partial J}{\partial \tilde{\mathbf{u}}} &= J\mathbf{F}^{-T} : \frac{\partial \mathbf{F}}{\partial \tilde{\mathbf{u}}} \\
\frac{\partial \mathbf{F}^{-1}}{\partial \tilde{\mathbf{u}}} &= -\mathbf{F}^{-1}\frac{\partial \mathbf{F}}{\partial \tilde{\mathbf{u}}}\mathbf{F}^{-1} \\
\frac{\partial \mathbf{P}}{\partial \tilde{\mathbf{u}}} = & \left(-\mu_0 - \frac{1}{\Omega}\left[R_g T\left(J \ln\left[\frac{J}{J-1}\right] - 1 - \frac{\chi}{J}\right) + \mu_c J\right]\right)\frac{\partial \mathbf{F}^{-T}}{\partial \tilde{\mathbf{u}}} \\
& -\frac{1}{\Omega}\left[R_g T\left(\ln\left[\frac{J}{J-1}\right] - \frac{1}{J-1} + \frac{\chi}{J^2}\right) + \mu_c\right]\frac{\partial J}{\partial \tilde{\mathbf{u}}}\mathbf{F}^{-T} \\
\frac{\partial \mathbf{P}}{\partial \tilde{\mu}_c} &= -\frac{J}{\Omega}\mathbf{F}^{-T}\frac{\partial \mu_c}{\partial \tilde{\mu}_c}
\end{aligned}
\tag{3.47}
$$

The nominal species flux vector and it's derivatives with respect to the DOF vectors are computed with the following equations.

$$
\begin{aligned}
\mathbf{M} &= \frac{D}{\Omega R_g T} J\mathbf{C}^{-1} \\
\mathbf{J} &= -\mathbf{M}\nabla^0 \mu_c \\
\frac{\partial \mathbf{M}}{\partial \tilde{\mathbf{u}}} &= \frac{D}{\Omega R_g T}\left(\frac{\partial J}{\partial \tilde{\mathbf{u}}}\mathbf{C}^{-1} + J\frac{\partial \mathbf{C}^{-1}}{\partial \tilde{\mathbf{u}}}\right) \\
\frac{\partial \mathbf{J}}{\partial \tilde{\mathbf{u}}} &= -\frac{\partial \mathbf{M}}{\partial \tilde{\mathbf{u}}}\nabla^0 \mu_c \\
\frac{\partial \mathbf{J}}{\partial \tilde{\mu}_c} &= -\mathbf{M}\mathbf{B}^{\mu_c}
\end{aligned}
\tag{3.48}
$$

The formula for computing ($\dot{C}$) is based on the incompressibility condition rewritten to express the concentration as a function of the deformation gradient derivative.

$$
C = \frac{\det \mathbf{F} - 1}{\Omega} \tag{3.49}
$$

The species concentration rate of change with respect to time, derived by differentiating Equation (3.49) with respect to time, and it's derivatives with respect to the DOF and

DOF rate vectors are computed with the following equations.

$$\begin{aligned} \dot{C} &= \tfrac{1}{\Omega}\tfrac{\partial J}{\partial t} = \tfrac{1}{\Omega} J\mathbf{F}^{-T} : \tfrac{\partial \mathbf{F}}{\partial t} = \tfrac{1}{\Omega} J\mathbf{F}^{-T} : \dot{\mathbf{H}} \\ \tfrac{\partial \dot{C}}{\partial \tilde{\mathbf{u}}} &= \tfrac{1}{\Omega}\left(\tfrac{\partial J}{\partial \tilde{\mathbf{u}}}\mathbf{F}^{-T} + J\tfrac{\partial \mathbf{F}^{-T}}{\partial \tilde{\mathbf{u}}}\right) : \dot{\mathbf{H}} \\ \tfrac{\partial \dot{C}}{\partial \dot{\tilde{\mathbf{u}}}} &= \tfrac{1}{\Omega} J\mathbf{F}^{-T} : \tfrac{\partial \dot{\mathbf{H}}}{\partial \dot{\tilde{\mathbf{u}}}} \end{aligned} \tag{3.50}$$

Chapter 4

Geometric Considerations

There have been numerous studies which suggest that electrode particle geometry can have significant impact on the performance of intercalation electrodes. In order to investigate the validity of such claims and create a hopefully useful numerical experiment/design tool pertinent mathematical models have been implemented in a finite element framework. Finite elements are ideal for exploring geometric effects because the model implementation is for the most part geometry independent; if a geometry can be discretized it can be simulated. However, just because a simulation can be performed doesn't mean that it will produce physically meaningful results. There are many choices that must be made when setting up a finite element simulation that can have significant impact on predictions including: application of initial and boundary conditions, choices of various solvers, material properties and constants.

Assuming good choices have been made for the entire problem setup, inaccurate results can still be predicted if the geometry isn't adequately represented. For example the thick walled sphere verification problem illustrated in Figure 5.12 is predicted to be too stiff on coarse meshes but as the mesh is refined the simulations converge on the accepted solution. To facilitate efficient modeling various geometries one, two, and three dimensional models have been implemented. In Section4.1 the assumptions made in implementing the one and two dimensional models are discussed.

The finite element model implementations provide powerful tools for studying

geometric effects, but complicated geometries can be difficult to discretize. While there are many powerful meshing tools which can be used to discretize complicated geometries, meshing can be very time consuming and difficult to automate for arbitrary geometries. As I am interested in optimization automation is a major concern. Without automated mesh generation optimization studies must be performed manually. For example in DeLuca et al. [22] a range of particle sizes and geometries were simulated in efforts to identify optimal silicon electrode particle morphologies. The study provided some interesting insight into size effects, but is was limited to simple cylindrical and spherical shapes. In order to facilitate studies of more complicated geometries and fully automated optimization an extended finite element method (XFEM) framework was developed. The XFEM framework is discussed in Section4.2.

4.1 Reduced Order Model Simplifications

The model development within is all presented within a general three dimensional context. However, in many problems of interest symmetry and assumptions about stress, strain, and transport can be used to reduce the number of spacial dimensions and thus the number of discrete degrees of freedom and computational expense. Two different two-dimensional and one one-dimensional reduced order models (ROM) have been implemented: plane-strain, axis-symmetric, and sphere-symmetric. All of the ROMs assume there is no variation in any of the state variables in the out of plane directions. In the two dimensional coordinate frame ROMs (plane-strain, and axis-symmetric) the transport governing equations can be written as

$$\dot{C} + \frac{\partial \mathrm{J}_x}{\partial x} + \frac{\partial \mathrm{J}_y}{\partial y} = 0 \tag{4.1}$$

with

$$\mathbf{J} = \begin{bmatrix} \mathrm{J}_x \\ \mathrm{J}_x \end{bmatrix} = CM \begin{bmatrix} \mathrm{C}_{xx} & \mathrm{C}_{xy} \\ \mathrm{C}_{yx} & \mathrm{C}_{yy} \end{bmatrix} \begin{bmatrix} \frac{\partial \mu_c}{\partial X} \\ \frac{\partial \mu_c}{\partial X} \end{bmatrix} \tag{4.2}$$

The plane-strain simplification is based on a three dimensional Cartesian coordinate frame making out of plane the z direction. While the transport equations for both of the two dimensional ROMs are identical, the mechanics equations for the tow different methods take on slightly different forms. In the plane-strain ROM it is assumed that there is no out of plane deformation; from this assumption it follows that all of the out of plane strain components are identically zero. By inspecting the constitutive relations listed in the appendix it can be determined that with no out of plane strain there is no out of plane shear stresses, but the out of plane normal stress (P_{zz}) may not be zero. In integrating the mechanics Equations (3.11) the nominal stress is second order contracted with the variation of the deformation gradient, so since there is no out of plane deformation the out of plane normal stress doesn't contribute to the system. Therefore, in purely mechanical systems all of the out of stress and strain components can be neglected. In our coupled systems, however, the transport can be driven by hydrostatic stress gradients. The out of plane normal stress contributes to the hydrostatic stress, and therefore must be computed in order to correctly model stress assisted diffusion.

The axis-symmetric ROM is based on a cylindrical coordinate frame making out of plane the θ direction. When changing from Cartesian to Cylindrical coordinate frames the gradient operators must also be changed. Using the standard cylindrical gradient operator and the assumption of no out of plane displacement, the displacement gradient can be written as

$$\nabla^0\mathbf{u} = \begin{bmatrix} \mathrm{H}_{rr} & \mathrm{H}_{ry} & 0 \\ \mathrm{H}_{yr} & \mathrm{H}_{yy} & 0 \\ 0 & 0 & \mathrm{H}_{\theta\theta} \end{bmatrix} = \begin{bmatrix} \frac{\partial \mathrm{u}_x}{\partial X} & \frac{\partial \mathrm{u}_x}{\partial Y} & 0 \\ \frac{\partial \mathrm{u}_y}{\partial X} & \frac{\partial \mathrm{u}_y}{\partial Y} & 0 \\ 0 & 0 & \frac{\mathrm{u}_x}{X} \end{bmatrix} \tag{4.3}$$

There are no out of plane shear strains, so there can be no out of plane shear stresses. Because $\mathrm{H}_{\theta\theta}$ is non-zero $\mathrm{P}_{\theta\theta}$ is non-zero. Therefore, $\mathrm{H}_{\theta\theta}$ and $\mathrm{P}_{\theta\theta}$ must both be accounted for when integrating the mechanics Equations (3.11). Furthermore, $\mathrm{P}_{\theta\theta}$ contributes to

the hydrostatic stress and must not be neglected when modeling stress assisted diffusion.

The sphere-symmetric ROM is based on a spherical coordinate frame, and assumes that state variables only vary in the radial direction. The transport governing equations can be written as

$$\dot{C} + \frac{\partial \mathrm{J}_x}{\partial X} + 2\frac{\mathrm{J}_x}{X} = 0 \tag{4.4}$$

with

$$\mathrm{J}_x = -C\mathrm{M}_{xx}\frac{\partial \mu_c}{\partial X} \tag{4.5}$$

M_{xx} is the xx component of the mobility tensor which depends on the deformation. Assuming that deformation is purely in the radial direction and using the standard spherical gradient operator the displacement gradient takes on the following form.

$$\nabla^0 \mathbf{u} = \begin{bmatrix} \mathrm{H}_{rr} & 0 & 0 \\ 0 & \mathrm{H}_{\theta\theta} & 0 \\ 0 & 0 & \mathrm{H}_{\phi\phi} \end{bmatrix} = \begin{bmatrix} \frac{\partial \mathrm{u}_x}{\partial X} & 0 & 0 \\ 0 & \frac{\mathrm{u}_x}{X} & 0 \\ 0 & 0 & \frac{\mathrm{u}_x}{X} \end{bmatrix} \tag{4.6}$$

Because there are no shear strains there can be no shear stresses. The sphere-symmetric ROM is convenient because it facilitates quick simulations.

4.2 Extended Finite Element Method

The extended finite element method extends traditional finite element methods to accommodate changing geometries on a fixed grid. XFEM was originally developed in efforts to model discontinuous deformation fields in crack propagation problems [7, 39, 48, 21]. Later, using level sets to represent an interface location, Miegrot and Duysinx [51] and Wei et al. [52] employed XFEM to model the evolving geometries in structural topology optimization problems. XFEM has also used to model discrete boundaries in fluid flow problems. Chessa and Belytchko [14] and Sauerland and Fries [44] used XFEM to model two phase flows, and Gerstenberger and Wall [26, 25] used XFEM to simulate fluid-structure interaction problems.

As has been demonstrated in several published works, XFEM provides a powerful framework for simulating changing geometries on a fixed grid. With the requirement of body fitted meshes removed, complicated geometries can be studied much more easily, and complicated geometry studies can be fully automated. The mesh still, however, places some restrictions on accuracy with which geometry can be represented. For example the circle inclusion in a square shown in Figure 4.1 is very accurately represented on the fine mesh, but in the coarse mesh the circle is represented as a rotated square. Therefore, when using an XFEM framework a mesh density must be intelligently chosen to adequately represent geometric features of interest. This concern is not, however, foreign to standard FEM, and responsible engineers using FEM tools typically perform mesh refinement studies before designing around simulation results.

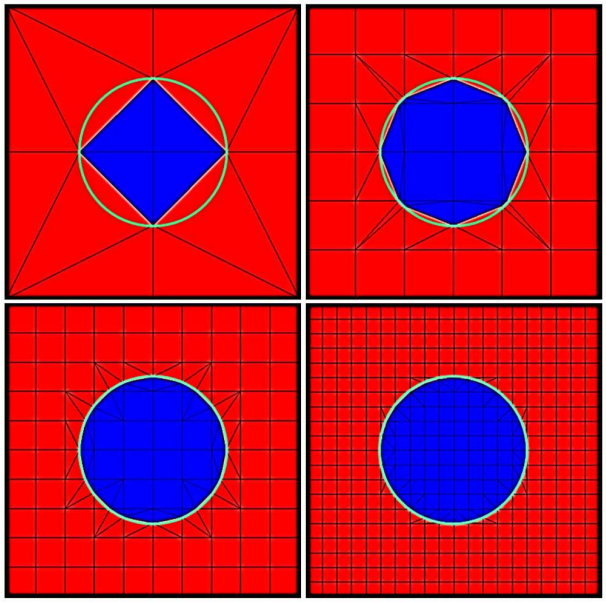

Figure 4.1: XFEM representations of a circle in a square on different grids. Phase 1 is blue and phase 2 is red.

In our XFEM implementation the phase distribution is represented by a nodally discretized level set field, where the zero levelset represents a phase interface. The

levelset field is interpolated linearly so no element edge can be intersected by the zero levelset more than once. Therefore the 2x2 mesh in Figure 4.1 is the coarsest structured grid that can be used to represent an inclusion in a square. In the coarse mesh all of the elements are represented as triangles because they are all intersected by a phase interface. When an element is intersected a geometric triangulation is used to determine integration points. From the finite element assembly routine's perspective the course mesh consists of four quadrilateral elements which are independent of the intersection pattern, but if the intersection pattern is changed a different triangulation will be used to determine how to integrate the mathematical systems used to represent the physics in each phase and along the interface. The triangulation used for determining integration points is convenient for visualizing XFEM results.

With levelsets and intersected element triangulation, we have a framework for representing arbitrary phase distributions on a grid. All of the details of our XFEM implementation will not be discussed within. There will, however, be some discussion on the treatment of constraints on the XFEM interfaces. For the purposes of being able to simulate battery phenomena we are concerned with satisfying displacement continuity and flux conditions at electrode-electrolyte interfaces. Butler-Volmer equations can be used directly for determining interface fluxes, but satisfying displacement continuity conditions is more complicated. We assume that displacements are continuous across an interface.

$$\int_{\Gamma} [\![\mathbf{u}]\!] \, d\Gamma^{(1/2)} = \int_{\Gamma} \left(\mathbf{u}^{(1)} - \mathbf{u}^{(2)} \right) d\Gamma^{(1/2)} = \mathbf{0} \tag{4.7}$$

The superscripts in parentheses indicate which phase the variables are with respect to; $\Gamma^{(1/2)}$ represents the interface between the two phases with respect to phase one. The displacement continuity constraint could be directly added to the system by including the following governing equations expressed in their weak form.

$$\int_{\Gamma} \delta\lambda \cdot [\![\mathbf{u}]\!] \, d\Gamma^{(1/2)} = 0 \tag{4.8}$$

Any Lagrange multiplier will satisfy Equation (4.8) so a consistency condition is added to stabilize the Lagrange multiplier preventing numerical issues. Setting the Lagrange multiplier equal to the average stress times the surface normal with respect to phase 1, the augmented Lagrange multiplier governing equation takes on the following form.

$$\underbrace{\int_{\Gamma} \delta\lambda \cdot \left(\lambda - \{\mathbf{P}\} \cdot \mathbf{n_0}^{(1)}\right) \Gamma^{(1/2)}}_{\text{consistency}} + \gamma \underbrace{\int_{\Gamma} \delta\lambda \cdot [\![\mathbf{u}]\!] \, \Gamma^{(1/2)}}_{\text{constraint}} = 0 \tag{4.9}$$

where $\{\mathbf{P}\} = \frac{1}{2}\left(\mathbf{P}^{(1)} + \mathbf{P}^{(2)}\right)$, and γ is a constraint scaling parameter. Assuming the Lagrange multiplier is constant over an element

$$\lambda = \int_{\Gamma} \left(\{\mathbf{P}\} \cdot \mathbf{n_0}^{(1)} - \gamma [\![\mathbf{u}]\!]\right) \Gamma^{(1/2)} \Big/ \int_{\Gamma} \Gamma^{(1/2)} \tag{4.10}$$

then from the equilibrium mechanics governing equations

$$\int_{\Gamma} \delta\mathbf{u}^{(1)} \cdot \mathbf{P}^{(1)} \cdot \mathbf{n_0}^{(1)} \Gamma^{(1/2)} + \int_{\Gamma} \delta\mathbf{u}^{(2)} \cdot \mathbf{P}^{(2)} \cdot \mathbf{n_0}^{(2)} \Gamma^{(2/1)} \tag{4.11}$$

is replaced by

$$\int_{\Gamma} [\![\delta\mathbf{u}]\!] \cdot \lambda d\Gamma^{(1/2)} \tag{4.12}$$

The above method for satisfying the displacement constraint is known as the local Lagrange multiplier method. It is convenient because It doesn't require the addition of any Lagrange multiplier DOFs. Another method for satisfying the displacement constraint without the addition of Lagrange multiplier DOFs which has been implemented in the code is known as the Nitsche method. In the Nitsche method the equilibrium mechanics boundary terms (Equation (4.11)) are replaced by

$$\begin{aligned} &\int_{\Gamma} [\![\delta\mathbf{u}]\!] \cdot \left(\{\mathbf{P}\} \cdot \mathbf{n_0}^{(1)}\right) \, d\Gamma^{(1/2)} - \int_{\Gamma} \delta \left(\{\mathbf{P}\} \cdot \mathbf{n_0}^{(1)}\right) \cdot [\![\mathbf{u}]\!] \, d\Gamma^{(1/2)} \\ &\underbrace{+ \gamma \int_{\Gamma} [\![\delta\mathbf{u}]\!] \cdot [\![\mathbf{u}]\!] \, d\Gamma^{(1/2)}}_{\text{stabilizationterm}} \end{aligned} \tag{4.13}$$

As will be demonstrated in the verification section both methods produce nearly equivalent behavior.

Chapter 5

Finite Element Model Verification

Mathematical models of coupled transport and mechanics have been implemented in a finite element framework. To verify that the models have been implemented correctly, example problems with known solutions are simulated with our finite element framework. Known solutions, some derived analytically within and some taken from publications, are compared to our simulation results. Verification studies for the small deformation models are presented in Section 5.1, followed by Section 5.2 covering the verification studies for finite deformation models.

5.1 Small Deformation Models

This first section of the verification chapter is concerned with validating the small deformation models. The small deformation models include the linear elastic mechanical equilibrium with species induced swelling model, the linear elastic surface stress model, and the small deformation diffusion model with and without stress coupling.

5.1.1 Analytical: Static Sphere with Surface Stress

The governing equation for mechanical equilibrium can be written for a sphere with no shear stresses as

$$\frac{\partial \sigma_r}{\partial r} + \frac{2}{r}\left(\sigma_r - \sigma_t\right) = 0 \tag{5.1}$$

where r is the radial coordinate, σ_r is the radial stress component, and σ_t is the tangential stress component. Assuming linear elasticity the stress components can be calculated with Equations (5.2) and (5.3).

$$\sigma_r = (\lambda_0 + 2\mu_0)\frac{\partial u_r}{\partial r} + \frac{2\lambda_0}{r}u_r \tag{5.2}$$

$$\sigma_t = \lambda_0\frac{\partial u_r}{\partial r} + \frac{2}{r}(\lambda_0 + \mu_0)u_r \tag{5.3}$$

By combining (5.2) and (5.3) with (5.1) we arrive at a second order differential equation.

$$\frac{\partial^2 u_r}{\partial r^2} + \frac{2}{r}\frac{\partial u_r}{\partial r} - \frac{2}{r^2}u_r = 0 \tag{5.4}$$

Assuming u_r has the form of a constant multiplied by r^n we find that

$$u_r = k_1 r + k_2 r^{-2} \tag{5.5}$$

Using a symmetry boundary condition (u_r(r)=-u_r(-r)) we find that k_2=0. Next we use the surface stress Equation (2.125) as a boundary condition to solve for k_1. For a sphere the surface stress equation reduces to

$$\sigma_r|_{r=R} + \frac{2}{R}\left(\tau_0 + \frac{\kappa^s}{R}u_r|_{r=R}\right) = 0 \tag{5.6}$$

Substituting Equations (5.2) and (5.5) into (5.6) we arrive at the following solution for radial displacement.

$$u_r = \frac{-\tau_0}{\frac{\mu_0}{2}R + \lambda_0 R + \kappa^s}r \tag{5.7}$$

Using a similar procedure the displacement solution for an infinite cylinder in equilibrium with surface stress is determined to be

$$u_r = \frac{-\tau_0}{\mu_0 R + \lambda_0 R + \kappa^s}r \tag{5.8}$$

Analytical solutions are compared to finite element solutions below.

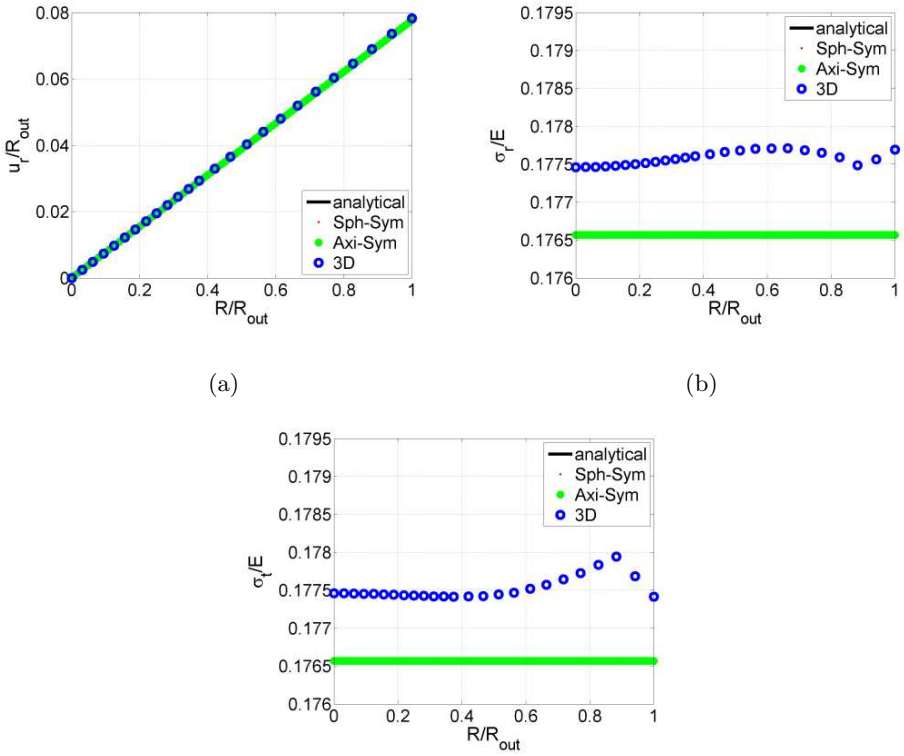

Figure 5.1: 1μm sphere in equilibrium with surface stress. (a) displacement profile, (b) radial stress profile, (c) tangential stress profile.

The sphere-symmetric problem is discretized with 100 bar3 elements in the interior and 1 point element at the boundary; the axis-symmetric problem is discretized with 2356 quad8 elements in the interior and 76 bar3 elements at the boundary; the 3D problem is discretized with 864 hexa20 elements in the interior and 108 quad8 elements at the boundary. The material properties and constants used in the simulations are listed in Table 5.1. Figure 5.1 shows that the sphere-symmetric, axis-symmetric, and 3D models all closely match the analytical solution. The deviation in the 3D solution can be removed with mesh refinement. For computational speed the higher dimensional meshes are increasingly coarse. The coarser meshes show further deviation from the analytical solution as should be expected. Similar results were obtained for an infinite cylinder. This test verifies that the mechanical part of the model including the surface

stress piece is correctly implemented.

Table 5.1: Particle Material Parameters

Symbol	Value	Units	Description
E	1.124e11	Pa	Young's modulus
ν	0.28	-	Poisson's ratio
τ_0	-1.0e4	N/m	Initial surface stress
κ^s	1.0e3	N/m	Tangent modulus

5.1.2 Analytical: Potentiostatic Insertion into Sphere

Cheng and Verbrugge derived analytical solutions for the concentration field and stress fields in a sphere particle during potentiostatic charging/discharging [13]. They used a linear elastic infinitesimal deformation model with concentration induced stresses and species flux described by Fick's Law. Using small deformation electrode particle elements 3.1.1 with simple Fickian diffusion, their solution was reproduced with a finite element simulation.

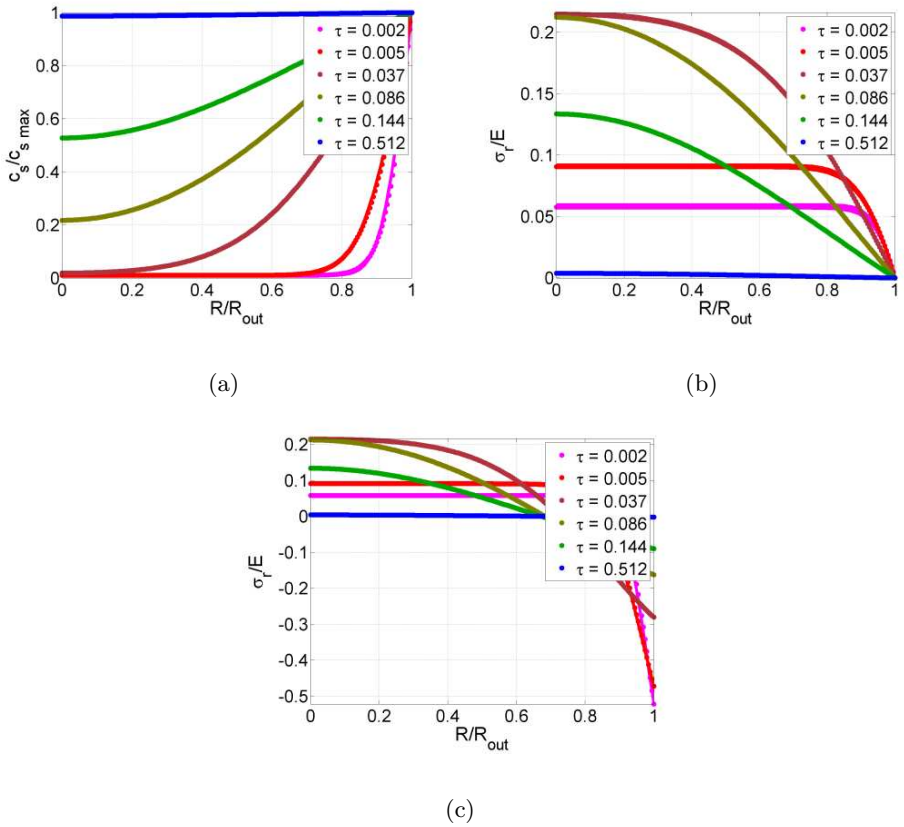

(a) (b)

(c)

Figure 5.2: 1μm sphere during potentiostatic insertion without stress induced diffusion. The dots represent the finite element solutions and the lines represent the analytical solution. (a) normalized concentration profile, (b) radial stress profile, (c) tangential stress profile.

The problem was discretized with 100 sphere-symmetric bar3 elements. The material properties and constants used in the simulation are listed in Table 5.2. The finite element simulation results very closely match the analytical solution. The largest deviation occurs for early times because the simulation is started with an infinite concentration gradient. However, as the simulation progressed the solutions converge towards the analytical solution. This test verifies the correctness of the linear elastic implementation not including the stress induced diffusion or surface stresses.

Table 5.2: Particle Material Parameters

Symbol	Value	Units	Description
E	1.124e11	Pa	Young's modulus
ν	0.28	-	Poisson's ratio
ω	1.422e-6	m^3/mol	Species expansion coefficient
D	1.0e-15	m^2/s	Species diffusion coefficient
c_{max}	3.111e5	mol/m^3	Maximum species concentration
c_0	3.111e3	mol/m^3	Initial species concentration

5.1.3 Analytical: Galvanostatic Insertion into Sphere

In the same paper from which solution of the previous validation study was taken there is an analytical solutions for the concentration and stress fields in a sphere particle during galvanostatic charging/discharging [13]. The same finite element model that was used in the previous verification study is used in this one. The only difference in the two problems is that we enforce Neumann instead of a Dirichlet boundary condition.

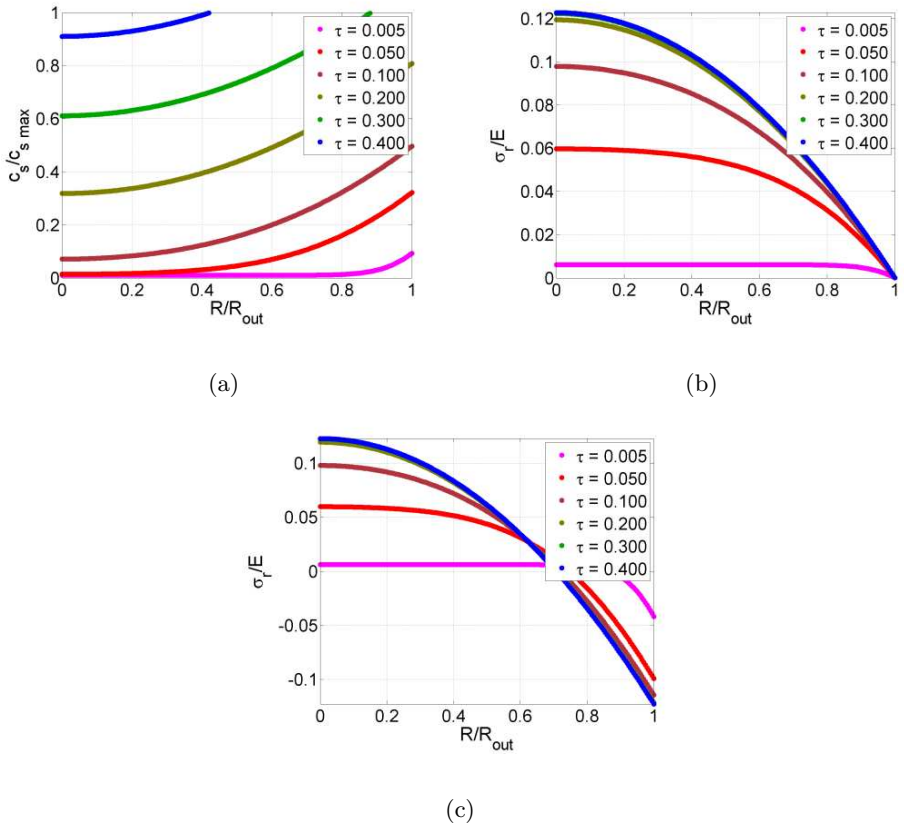

Figure 5.3: 1μm Sphere during galvanostatic insertion without stress induced diffusion. The dots represent the finite element solutions and the lines represent the analytical solution. (a) normalized concentration profile, (b) radial stress profile, (c) tangential stress profile.

The problem was discretized with 100 sphere-symmetric bar3 elements. The material properties and constants used in the simulation are listed in Table 5.2. Over all time steps the simulation results match the analytical solution very well. This test further verifies the correctness of the linear elastic implementation not including the stress induced diffusion or surface stresses.

5.1.4 Analytical: Potentiostatic Insertion into Sphere with Surface Stress

In an earlier paper by Cheng and Verbrugge [11], analytical solutions were developed for the concentration field and stress fields in a sphere particle during galvanostatic charging/discharging with surface stress included. In order to verify that the sphere-symmetric, axis-symmetric, and three dimensional versions of the governing equations are correctly implemented, all three models are compared to the analytical solutions.

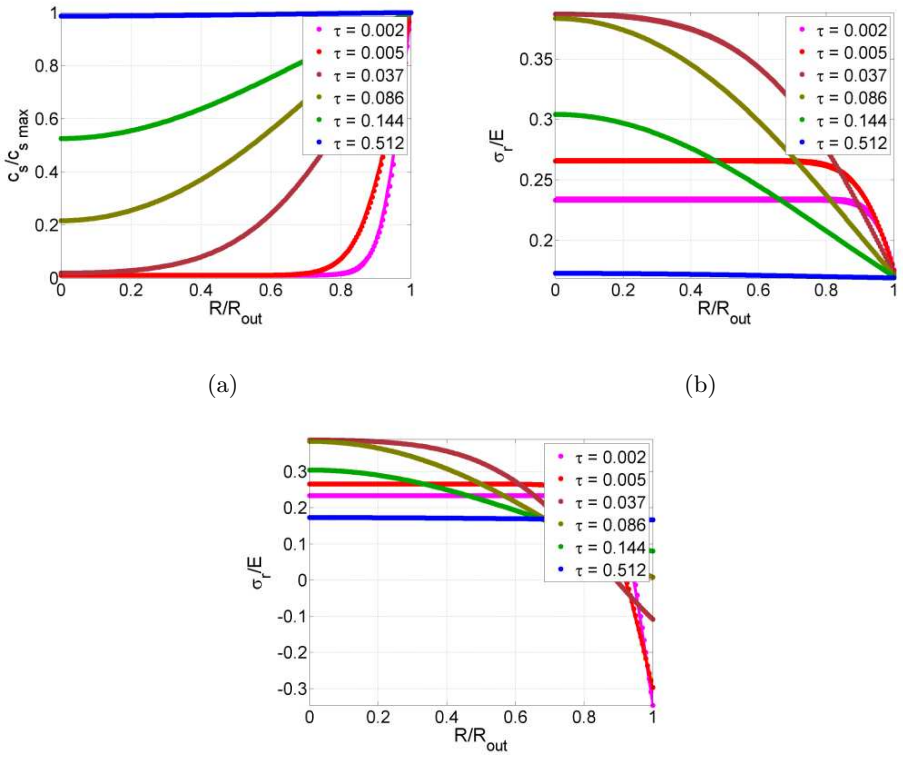

(a) (b)

(c)

Figure 5.4: (Sphere-Symmetric) 1μm sphere during potentiostatic insertion with surface stress and without stress induced diffusion. The dots represent the finite element solutions and the lines represent the analytical solution. (a) normalized concentration profile, (b) radial stress profile, (c) tangential stress profile.

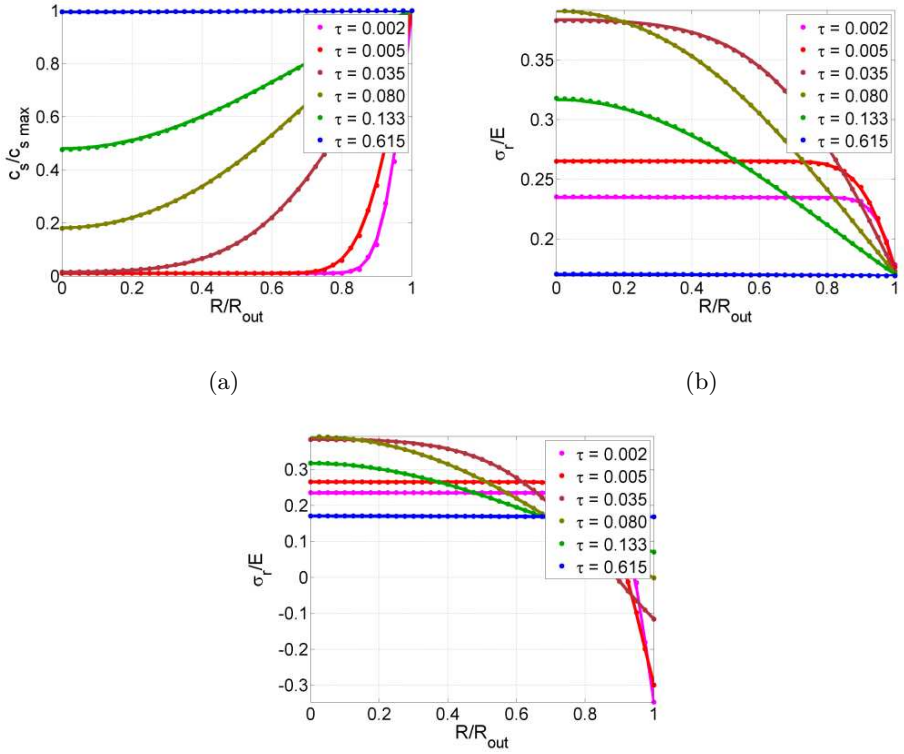

(a) (b)

(c)

Figure 5.5: (Axis-Symmetric) 1μm sphere during potentiostatic insertion with surface stress and without stress induced diffusion. The dots represent the finite element solutions and the lines represent the analytical solution. (a) normalized concentration profile, (b) radial stress profile, (c) tangential stress profile.

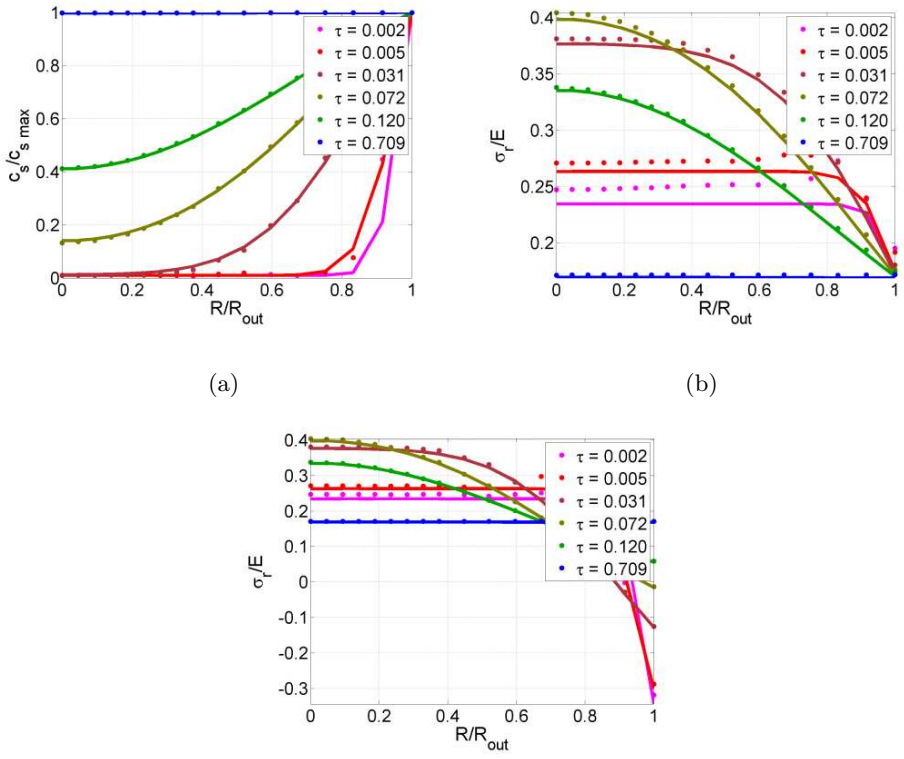

Figure 5.6: (Full 3D) 1μm sphere during potentiostatic insertion with surface stress and without stress induced diffusion. The dots represent the finite element solutions and the lines represent the analytical solution. (a) normalized concentration profile, (b) radial stress profile, (c) tangential stress profile.

The 1D mesh was very finely discretized to get as close to the analytical solution as possible, but because computational expense increases exponentially with the dimension of the elements the 2D and 3D meshes are much coarser. The sphere-symmetric problem is discretized with 100 bar3 elements in the interior and 1 point element at the boundary; the axis-symmetric problem is discretized with 2356 quad8 elements in the interior and 76 bar3 elements at the boundary; the 3D problem is discretized with 2624 hexa20 elements in the interior and 192 quad8 elements at the boundary. The deviation seen in 3D solution can be alleviated with mesh refinement. Just as in the potentiostatic simulation without surface stress, the largest deviation occurs for early

times because the simulation is started with an infinite concentration gradient. Most of the material properties used in the simulation are listed in Table 5.2, and the surface stress properties are listed in Table 5.1. This test verifies the correctness of the linear elastic implementation with surface stresses not including stress induced diffusion.

5.1.5 Finite Element: Galvanostatic Insertion into Sphere (Fully Coupled)

No analytical solutions have been developed for the fully coupled model with stress induced diffusion included. Zhang et al. [60] simulated galvanostatic Li insertion into Mn_2O_4 spheres, using a linear elastic model that is identical to ours. In order to validate the full model Zhang's finite element results are reproduced with our finite element code. The black lines are taken from the published paper and the colored lines were produced by compiling data from finite element simulations run in our finite element code.

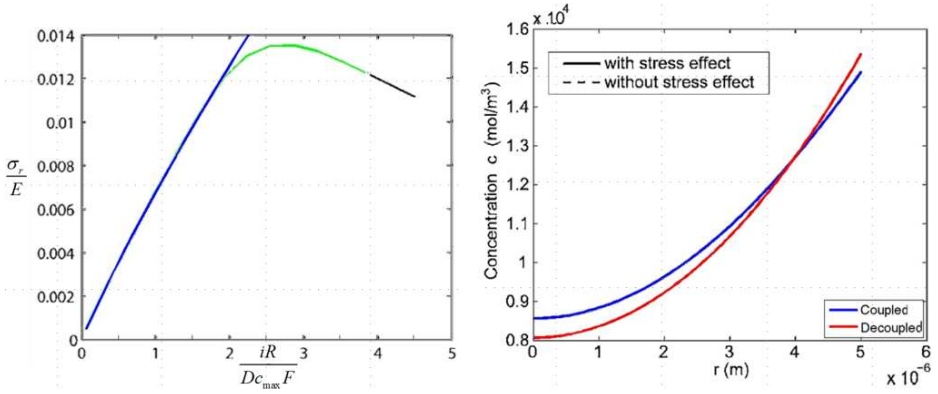

(a) (b)

Figure 5.7: Sphere during galvanostatic insertion

Figure 5.7(a) shows the maximum non-dimensional radial stress during Li insertion as a function of the non-dimensional insertion rate. The green line was generated by finding the absolute maximum stress predicted in by each simulation before the surface

concentration reached the maximum concentration. In Zhang et al. [60] simulations were stopped when the surface concentration reached the maximum concentration, but in simulations with large applied surface currents the stresses magnitudes are still increasing when the surface reaches the maximum concentration. If the simulations are allowed to continue running until the particles reach their theoretical maximum capacity, which happens after the maximum concentration is reached at the surface, then compiling the maximum stresses produces the blue line. Figure 5.7(b) shows concentration profiles at time ($t = 1000s$) for galvanostatic simulations with and without stress-diffusion coupling. Our finite element results match the published results as closely as can be measured by overlaying graphical results. The problem was discretized with 100 bar3 elements, and all of the material properties and constants were taken from Zhang et al. [60]. This test verifies the correctness of the fully coupled linear elastic model, not including surface stress.

5.2 Finite Deformation Models

This section is concerned with validating the finite deformation models. The finite deformation models include six non-linear elastic mechanical equilibrium with species induced swelling models, and two finite deformation diffusion models with stress coupling.

5.2.1 Analytical: Compressible Non-linear Elastic Materials with Uniform Stress Fields

Six different non-linear elastic models have been implemented: two different Neo-Hookean models [8, 2], a Mooney-Rivlin model [6], an Arruda-Boyce model [2], a Gent model [2], and a Kirchhoff model [8]. The strain energy densities and the associated PK2 stress equations for each material model are presented in the appendix. In efforts to verify that the stress equations were implemented correctly, the finite element models

were loaded in ways that produce uniform stress and strain fields. The loads are applied as surface pressures integrated over the deformed surfaces. Then using the deformation solutions from the finite element models, stresses were calculated outside of the finite element model and compared to those calculated with the finite element model. Because uniform pressures are applied to the surfaces the uniform stress fields should match the applied pressures. Four different cases were simulated with each model and with as many different element types as could be used. The four loading cases called uniaxial deformation, equi-biaxial deformation, equi-triaxial deformation, and shear deformation are depicted in the figure below.

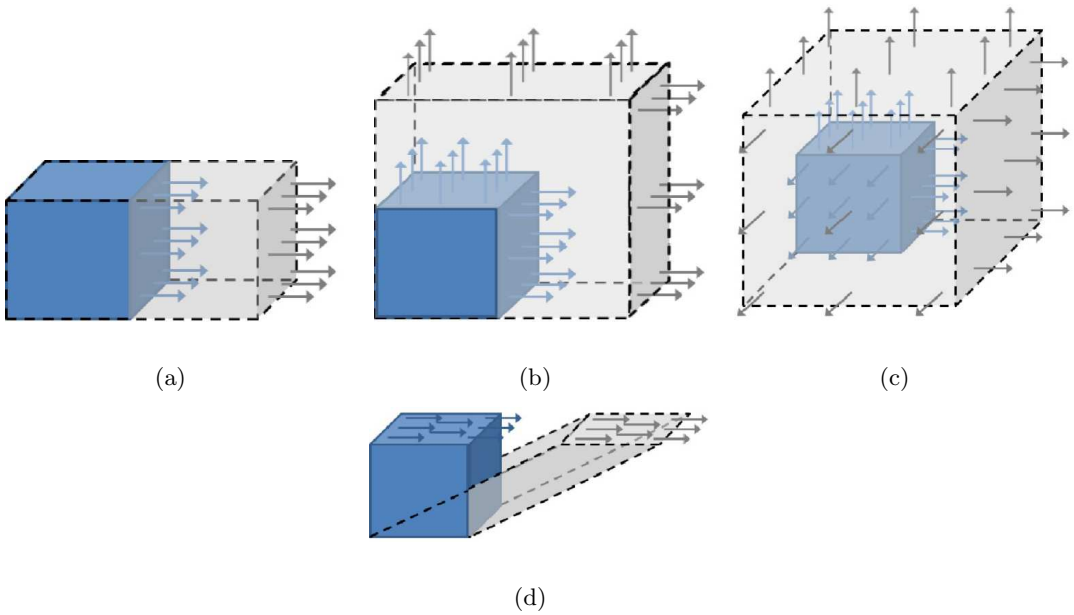

Figure 5.8: Compressible nonlinear structure test schematics. (a) uniaxial deformation, (b) equi-biaxial deformation, (c) equi-triaxial deformation, (d) shear deformation.

For each of the first three cases, all planes with no applied pressures are constrained to remain on the same plane as the reference configuration. The blue cubes represent the reference configurations, and the grey translucent shapes represent the deformed configurations. The arrows represent uniform applied surface tractions. The

characteristic deformation states of each of the four cases are described below.

$$\begin{aligned} \text{uniaxial}: &\qquad \lambda_1 = \lambda, &\qquad \lambda_2 = \lambda_3 = 1 \\ \text{equi}-\text{biaxial}: &\qquad \lambda_1 = \lambda_2 = \lambda, &\qquad \lambda_3 = 1 \\ \text{equi}-\text{triaxial}: &\qquad \lambda_1 = \lambda_2 = \lambda_3 = \lambda \\ \text{shear}: &\qquad \mathbf{F} = \begin{bmatrix} 1 & \frac{\partial u_x}{\partial y} & 0 \\ 0 & 1 & 0 \\ 0 & 0 & 1 \end{bmatrix} \end{aligned} \tag{5.9}$$

Table 5.3 lists the material properties used in this set of tests, and Table 5.4 lists all of the elements and material types that were validated with this set of tests. In each of the tests performed, the finite element computed stresses perfectly matched the analytical ones. Element type and material model keys for the abbreviations used in Table 5.4 are presented in tables 5.5 and 5.6 respectively. These tests verify that the stress equations entered into the finite element models are consistent with the stress equations used outside of the simulations and that the surface element correctly accounts for deformation when integrating surface pressures.

Table 5.3: Compressible Elastic Material Properties

Symbol	Value	Units	Description
E	1.0e10	Pa	Young's modulus
ν	0.30	-	Poisson's ratio
λ_{mab}	2.5	-	Arruda-Boyce stretch limiting parameter
λ_{mg}	7.0	-	Gent stretch limiting parameter

Table 5.4: Compressible Elastic Materials with Uniform Stresses Verification Problems

Test No.	Test Name	Element Types						Material Models
		Bar2	Bar3	Quad4	Quad8	Hexa8	Hexa20	
1	Uniaxial Deformation (Single Element)	NA	NA	AX & PE	AX & PE	X	X	Lin, NH, NH1, MR, GE, AB, KR
2	Equi-Biaxial Deformation (Single Element)	NA	NA	PE	PE	X	X	Lin, NH, NH1, MR, GE, AB, KR
3	Equi-Biaxial Deformation (Cylinder)	NA	NA	1x1 (AX)	1x1 (AX)	6x6x1	6x6x1	Lin, NH, NH1, MR, GE, AB, KR
4	Equi-Triaxial Deformation (Single Element)	X	X	NA	NA	X	X	Lin, NH, NH1, MR, GE, AB, KR
5	Equi-Triaxial Deformation (Sphere)	1	1	10x10 (AX)	10x10 (AX)	8x8x8	8x8x8	Lin, NH, NH1, MR, GE, AB, KR
6	Shear Deformation (Single Element)	NA	NA	PE	PE	X	X	Lin, NH, NH1, MR, GE, AB, KR

Table 5.5: Element Type Key

Symbol	Description
Bar2	2-node linear symmetric sphere line element
Bar3	3-node quadratic symmetric sphere line element
Quad4 (PE)	4-node bilinear plane-strain quadrilateral element
Quad4 (PS)	4-node bilinear plane-stress quadrilateral element
Quad4 (AX)	4-node bilinear axis-symmetric quadrilateral element
Quad8 (PE)	8-node biquadratic plane-strain quadrilateral element
Quad8 (PS)	8-node biquadratic plane-stress quadrilateral element
Quad8 (AX)	8-node biquadratic axis-symmetric quadrilateral element
Hexa8	8-node trilinear hexahedral element
Hexa20	20-node triquadratic hexahedral element

Table 5.6: Material Model Key

Symbol	Description
Lin	Isotropic linear elasticity
NH	Neo-Hookean [8]
NH1	Neo-Hookean [2]
MR	Mooney-Rivlin [6]
GE	Gent [2]
AB	Arruda-Boyce [2]
KR	Isotropic Kirchhoff [8]

5.2.2 Analytical: Incompressible Non-linear Elastic Materials with Uniform Stress Fields

According to the mechanical theory, the finite element model should be able to nearly produce compressible behavior if the Poission's ration is set close to one half. In order to further validate the finite element implementation the results from the code are compared to analytical solutions to incompressible materials in two simple loading cases pictured below.

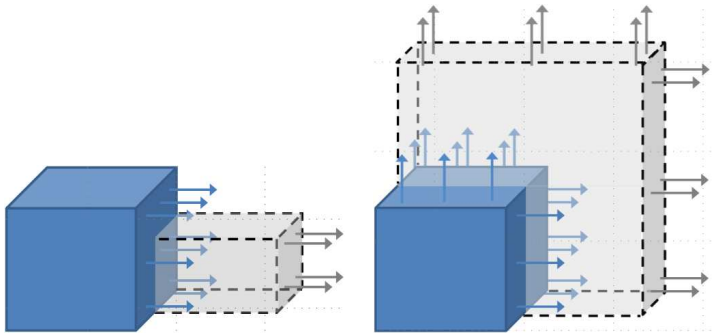

(a) (b)

Figure 5.9: (a) Simple Stretching, (b) Equi-Biaxial Stretching.

Also, as was done in the previous validation studies, the deformation solutions

from the finite element models were used to compute the stresses outside of the finite element model and compared to those calculated with the finite element model. Analytical solutions are derived within for incompressible Neo-Hookean and Mooney-Rivlin models following the work of Gerhard A. Holzapfel [33]. For incompressible hyperelastic material models the third invariant, I_3, is identically 1. Combining the well known transformation equation, $\boldsymbol{\sigma} = J^{-1}\mathbf{F}\mathbf{S}\mathbf{F}^{\mathbf{T}}$, with the PK2 equation for incompressible materials (2.37) we arrive at the following equation for the Cauchy stress tensor [33].

$$\boldsymbol{\sigma} = 2\left(\frac{\partial \Psi}{\partial I_1} + I_1\frac{\partial \Psi}{\partial I_2}\right)\mathbf{B} - 2\frac{\partial \Psi}{\partial I_2}\mathbf{B}^2 - p_o\boldsymbol{\delta} \tag{5.10}$$

$\mathbf{B}$ is the left Cauchy-Green deformation tensor and p_o is the osmotic pressure. The inverse of the determinant of the deformation gradient, J^{-1}, is intentionally left out of Equation (5.10) because it is identically 1. The left Cauchy-Green deformation tensor is calculated as

$$\mathbf{B} = \mathbf{F}\mathbf{F}^T \tag{5.11}$$

From here we can assume a volume preserving deformation state and determine the pressure term. In the case of simple stretching ($\lambda_1 = \lambda$, $\lambda_2 = \lambda_3 = 1/\sqrt{\lambda}$) the invariants are

$$\begin{aligned} I_1 &= \lambda^2 + 2\lambda^{-1} \\ I_2 &= \lambda^{-2} + 2\lambda \end{aligned} \tag{5.12}$$

and the left Cauchy-Green deformation tensor is

$$\mathbf{B} = \begin{bmatrix} \lambda^2 & 0 & 0 \\ 0 & \lambda^{-1} & 0 \\ 0 & 0 & \lambda^{-1} \end{bmatrix} \tag{5.13}$$

We assume that the deformation is caused by applying a pressure on one face while keeping the others free. Therefore, there should be a uniform stress in the direction of

the applied pressure while the other stresses should be zero.

$$\begin{aligned} \sigma_2 = \sigma_3 = 0 &= 2\left(\frac{\partial\Psi}{\partial I_1} + I_1\frac{\partial\Psi}{\partial I_2}\right)\lambda^{-1} - 2\frac{\partial\Psi}{\partial I_2}\lambda^{-2} - p_o \\ \Rightarrow p_o &= 2\left(\frac{\partial\Psi}{\partial I_1} + I_1\frac{\partial\Psi}{\partial I_2}\right)\lambda^{-1} - 2\frac{\partial\Psi}{\partial I_2}\lambda^{-2} \end{aligned} \tag{5.14}$$

Substituting the osmotic pressure and the first invariant into Equation (5.10) we arrive at the following equation for the principal stress.

$$\sigma_1 = 2\left(\lambda^2 - \lambda^{-1}\right)\left(\frac{\partial\Psi}{\partial I_1} + \lambda^{-1}\frac{\partial\Psi}{\partial I_2}\right) \tag{5.15}$$

The strain energy functions for the incompressible Neo-Hookean and Mooney-Rivlin materials can be written in the form below [33].

$$\Psi = \frac{\mu_0}{2}\left(I_1 - 3\right) \tag{5.16}$$

$$\Psi = C_1\left(I_1 - 3\right) + C_2\left(I_2 - 3\right) \tag{5.17}$$

$2\left(C_1 + C_2\right) = \mu_0$, and μ_0 is the shear modulus. Substituting the strain energy functions into the equation for the principal Cauchy stress (5.15) we arrive at the following analytical solutions for the principal stress experienced during simple stretching for Neo-Hookean and Mooney-Rivlin models respectively.

$$\sigma_1 = \mu_0\left(\lambda^2 - \lambda^{-1}\right) \tag{5.18}$$

$$\sigma_1 = 2\left(\lambda^2 - \lambda^{-1}\right)\left(C_1 + C_2\lambda^{-1}\right) \tag{5.19}$$

Figure 5.10 shows the stress stretch curves for five different compressible hyperelastic models, the Kirchhoff model, and the linear elastic model plotted over the analytical solutions presented above. In the Mooney-Rivlin model we set $C_1 = C_2$.

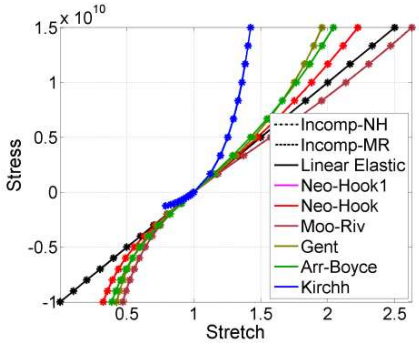

Figure 5.10: (Simple stretching) The points marked with asterisks, *, are data points from finite element simulations, the color lines represent the analytical stresses calculated with the deformation states from the finite element simulations, and the black lines represent analytical solutions to the fully incompressible models.

The presented results were produced with quad4 elements using a axissymmetric assumption, but identical results, not presented within, were also produced with axissymmetric quad8 elements, hexa8 elements, and hexa20 elements. Material properties used in the simple stretching problem are presented in Table 5.7. The stresses computed by the finite element models perfectly match those calculated given the deformation states in the finite element simulations, for all material models. Both Neo-Hookean and the Mooney-Rivlin finite element models produce solutions nearly coincident to their analytical incompressible counterparts. The analytical solutions on the figure are completely obscured by the finite element solutions. This study verifies that the equations are implemented correctly, the compressible models are capable accurately of simulating incompressible behavior when there is a uniform single axis stress field, and that the surface elements correctly account for deformation when integrating surface pressures.

Following a similar procedure as was discussed above, an analytical solution can be obtained for Incompressible hyperelastic materials during equi-biaxial stretching ($\lambda_1 = \lambda_2 = \lambda$, $\lambda_3 = 1/\lambda^2$). The analytical solutions for the incompressible Neo-Hookean and

incompressible Mooney-Rivlin are given by the following equations, respectively

$$\sigma_1 = \mu_0 \left(\lambda^2 - \lambda^{-4}\right) \tag{5.20}$$

$$\sigma_1 = 2 \left(\lambda^2 - \lambda^{-4}\right) \left(C_1 + C_2 \lambda^2\right) \tag{5.21}$$

Figure 5.11 shows the stress stretch curves for five different compressible hyperelastic models, the Kirchhoff model, and the linear elastic model plotted over the analytical solutions presented above.

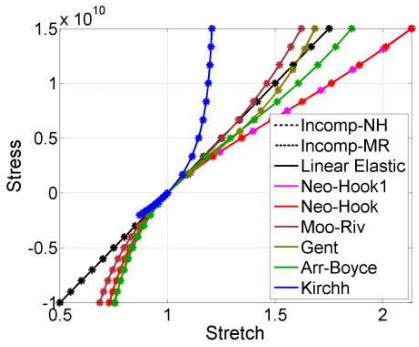

Figure 5.11: (Equi-biaxial stretching) The points marked with asterisks, *, are data points from finite element simulations, the color lines represent the analytical stresses calculated with the deformation states from the finite element simulations, and the black lines represent analytical solutions to the fully incompressible models.

The above results were produced with quad4 elements using a axissymmetric assumption, but identical results, not presented within, were also produced with axissymmetric quad8 elements, hexa8 elements, and hexa20 elements. Material properties used in the biaxial stretching problem are presented in Table 5.7. The stresses computed by the finite element models perfectly match those calculated given the deformation states in the finite element simulations, for all material models. Both Neo-Hookean and the Mooney-Rivlin finite element models produce solutions nearly coincident to their analytical incompressible counterparts. The analytical solutions on the figure are completely obscured by the finite element solutions. This study verifies that the equations are

implemented correctly, the compressible models are capable accurately of simulating incompressible behavior when there is a uniform two axis stress field, and that the surface elements correctly account for deformation when integrating surface pressures.

The simple stretching and biaxial stretching problems were also set up and solved with a plane-stress assumption, but the simulations results significantly deviated from the analytical solution. This is because unlike in linear elasticity the plane-stress assumption does not have an analytical solution for the out of plane strain component. The out of plane strain component must either be computed with a nonlinear solver at each gauss point, or as is typically done in the Ansys and Abaqus codes it can be approximated based on the in plane strains and the Poisson's ratio. In the current version of the finite element code the out of plane strain is approximated to minimize complications.

Table 5.7: Incompressible Elastic Material Properties

Symbol	Value	Units	Description
E	1.0e10	Pa	Young's modulus
ν	0.49975	-	Poisson's ratio
λ_{mab}	2.5	-	Arruda-Boyce stretch limiting parameter
λ_{mg}	7.0	-	Gent stretch limiting parameter

All of the above non-linear elastic validation studies require some derivation and/or interpretation, which leaves room for mistakes. In order circumvent sources of error, a hyperelasticity benchmark problem from the Ansys verification manual , VM269 [3], was reproduced with a number of elements implemented in the femdoc code. The sphere problem was perfectly matched with the bar2, bar3, quad4 (AX), quad8 (AX), hexa8, and hexa20 elements, and the cylinder problem was perfectly matched with the quad4 (AX), quad8 (AX), hexa8, and hexa20 elements. The Ansys benchmark prob-

lem further verifies the correctness of the code implementation by comparison with a well known solution. However, as with the previous problems in VM269 the stress field is uniform. To verify that the code behaves correctly for a more complicated loading case, another validation problem is taken from the paper referenced by the benchmark problem. In Yosibash et al 2007 [54], an "exact" solution for a thick walled incompressible hyperelastic hollow sphere with an applied internal pressure is reported and compared with finite element solutions obtained with different formulations. A thick walled incompressible hyperelastic hollow sphere, Figure 5.12, is loaded with an internal pressure, p = 1MPa.

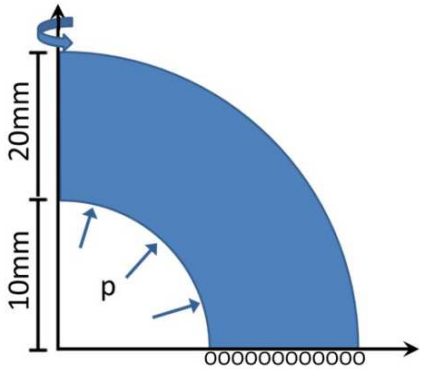

Figure 5.12: Thick walled sphere with applied internal pressure.

In the Yosibash paper the problem was simulated with axis-symmetric 4 node bilinear quadrilateral elements, so initially the problem was simulated in femdoc with the quad4 (AX) element. The plots below show the results of an initial mesh convergence study.

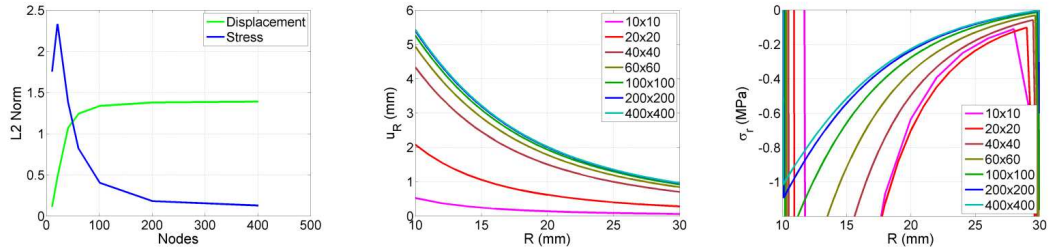

(a) (b) (c)

Figure 5.13: (a) mesh convergence, (b) displacement profile, (c) radial stress profile.

The results pictured in Figure 5.13 show much worse mesh convergence than those presented in the Yosibash paper [54]. After comparisons with results generated using Ansys and investigation into the Ansys theory reference [2], it was determined that some form of selective reduce integration (SRI) scheme must have been used. A selective reduced integration scheme taken from Belytchko et al 2004 [8] was implemented and the mesh convergence study was repeated.

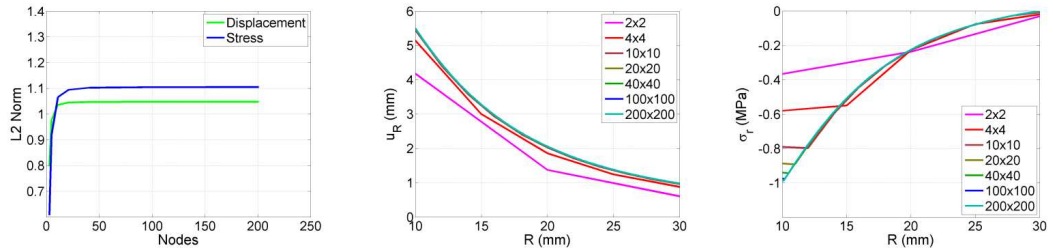

(a) (b) (c)

Figure 5.14: (a) mesh convergence, (b) displacement profile, (c) radial stress profile.

Figure 5.14 illustrates the results of the mesh convergence study with SRI. The SRI results match Ansys and the results published in the Yoshibash paper. Mesh convergence studies were performed with all of the other element in femdoc that were capable of discretizing the domain: for a complete list refer to Table 5.9. Figure 5.15 shows the results of the mesh convergence study that was performed using under integrated quad8 (AX) elements.

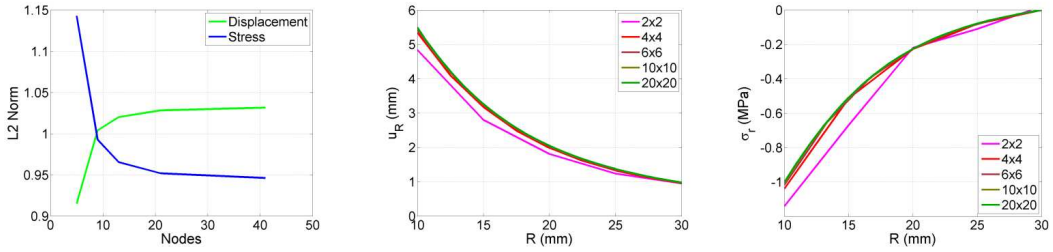

(a) (b) (c)

Figure 5.15: (a) mesh convergence, (b) displacement profile, (c) radial stress profile.

The discrepancies in initial quad4 (AX) mesh convergence study are the result of element locking in nearly incompressible elements. In linear elements some form of reduced integration should be used to prevent element locking [2, 8], but quadratic elements can simply be under integrated to mitigate the problem. Figure 5.15 demonstrates that under integrated quadratic elements are superior to SRI linear elements for simulating incompressible hyperelastic problems. These tests complete the validation ot the non-linear elastic elements, as well as the finite deformation surface elements. The material properties used in the incompressible thick walled hollow cylinder and hollow sphere problems are listed in Table 5.8. Table 5.9 lists all of the elements and material models that were validated by comparison with each of the incompressible non-linear elastic test problems.

Table 5.8: Incompressible Elastic Material Properties

Symbol	Value	Units	Description
E	3.0e6	Pa	Young's modulus
ν	0.49975	-	Poisson's ratio

Table 5.9: Incompressible Elastic Materials Verification Problems

Test No.	Test Name	Element Types						Material Models
		Bar2	Bar3	Quad4	Quad8	Hexa8	Hexa20	
1	Incompressible Simple Tension (Single Element)	NA	NA	AX	AX	X	X	Lin, NH, NH1, MR, GE, AB, KR
2	Incompressible Biaxial Tension (Single Element)	NA	NA	AX	AX	X	X	Lin, NH, NH1, MR, GE, AB, KR
3	VM269 Hollow Cylinder with uniform pressure	NA	NA	AX	AX	X	X	NH1
4	VM269 Hollow Sphere with uniform pressure	X	X	AX	AX	X	X	NH1
5	Hollow Sphere with internal pressure	X	X	AX	AX	X	X	NH1

5.2.3 Analytical: Incompressible Non-linear Elastic Swollen Materials with Uniform Stress Fields

The mechanical models have been verified with a large number of test problems, but thus far swelling has been ignored. To verify the swelling piece of the finite deformation mechanical models, uniform non-zero concentrations are applied, and then the models are subjected to simple stretching (illustrated in Fig. 5.9(a)). In the following study the deforming body is deicretized with a single element. This setup is used to verify total and volumetric strain energy coupled compressible and incompresible models. The compressible models produce nearly incompressible behavior if the Poission's ration is set close to one half. Because all of the different nonlinear elastic models have been thoroughly verified only Belytchko's Neohookean model, Equation (8.5), is studied in these tests. Analytical solutions are derived in a very similar manner as was done in for the simple stretching case presented above. For incompressible materials the deformation gradient determinant is only a function of the nominal concentration ($J^c = 1 + \Omega C = J$). Therefore if the body is held at a constant uniform concentration then the deformation gradient determinant should remain constant. Then assuming simple stretching of a swollen body, the deformation gradient takes on the following

form.

$$\mathbf{B} = \begin{bmatrix} \lambda & 0 & 0 \\ 0 & \left(\frac{J}{\lambda}\right)^{1/2} & 0 \\ 0 & 0 & \left(\frac{J}{\lambda}\right)^{1/2} \end{bmatrix} \tag{5.22}$$

First analytic solutions are derived for the total strain energy coupled swelling formulation. Using the Neohookean model represented by (8.5) with the compressible TSEC nominal stress Equation (2.62) and the appropriate stress transformation rule (8.1) the PK2 stress tensor can be represented with the following formula.

$$\mathbf{S} = \mu_0 J \left[J^{-2/3} \boldsymbol{\delta} - \mathbf{C}^{-1} \right] + p_o J^2 \mathbf{C}^{-1} \tag{5.23}$$

Then using the appropriate stress transformation rule, Equation (8.1), we arrive at the following equation the Cauchy stress tensor.

$$\boldsymbol{\sigma} = \mu_0 \left[J^{-2/3} \mathbf{B} - \boldsymbol{\delta} \right] + p_o J \boldsymbol{\delta} \tag{5.24}$$

Knowing that the true stress in the free directions are zero, $\sigma_2 = \sigma_3 = 0$, we solve for the osmotic pressure, p_o.

$$p_o = \mu_0 J^{-1} \left[1 - \frac{J^{1/3}}{\lambda} \right] \tag{5.25}$$

Then inserting the osmotic pressure into the equation for the stress in the stretch direction we find the following equation for computing the only non-zero stress component.

$$\sigma_1 = \mu_0 \left[\left(\frac{\lambda}{J^{1/3}} \right)^2 - \frac{J^{1/3}}{\lambda} \right] \tag{5.26}$$

Next we derive the analytical solution for the incompressible volumetric strain energy coupled mechanical model. The deformation gradient can be characterized in the same way, but the stress equations are different. Using the general Neohookean PK2 Equation (8.6) with the incompressible volumetric strain energy coupled model's PK2 Equations (3.30) the PK2 tensor can be represented with the following formula.

$$\mathbf{S} = \mu_0 \left[\boldsymbol{\delta} - \mathbf{C}^{-1} \right] + p_o J \mathbf{C}^{-1} \tag{5.27}$$

Then using the appropriate stress transformation rule, Equation (8.1), we arrive at the following equation the Cauchy stress tensor.

$$\boldsymbol{\sigma} = \frac{\mu_0}{J}\left[\mathbf{B} - \boldsymbol{\delta}\right] + p_o\boldsymbol{\delta} \tag{5.28}$$

Knowing that the true stress in two of the three principal directions are zero, $\sigma_2 = \sigma_3 = 0$, we solve for the osmotic pressure, p_o.

$$p_o = \frac{\mu_0}{J}\left[1 - \frac{J}{\lambda}\right] \tag{5.29}$$

Then inserting the osmotic pressure into the equation for the stress in the stretch direction we find the following equation for computing the only non-zero stress component.

$$\sigma_1 = \mu_0\left[\frac{\lambda^2}{J} - \frac{1}{\lambda}\right] \tag{5.30}$$

The figure below shows the analytical principal stress solutions for both coupling types plotted with results obtained with the various finite element implementations.

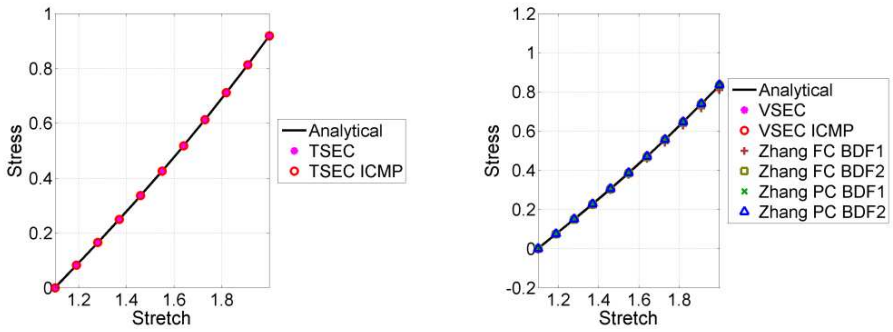

(a) (b)

Figure 5.16: (a) Total strain energy coupled (TSEC) stress, (b) Volumetric strain energy coupled (VSEC) stress.

In Figure 5.16 "ICMP" signifies when the incompressible formulations of the swelling hyperelastic material models described in section 3.2.6 were used. If Figure 5.16(b) "Zhang" signifies when the finite deformation hydrogel material model described

in Section 3.2.8. The Zhang model is based on a volumetric strain energy coupled Neohookean formulation so its' stress solutions were included in the VSEC plot. There are four sets of Zhang solutions: "PC" stands for prescribed chemical potential, "FC" stands for free chemical potential, "BDF1" stands for first order backward difference time solver, and "BDF2" stands for second order backward difference time solver. The parameters used in the swollen simple stretching simulations are listed in Table 5.10.

All of the generated solutions appear to lie directly on top of their analytical counterparts, but there are some discrepancies between the analytical solution and the Zhang solutions. In the PC solutions the chemical potential is prescribed as the body is deformed, and the stress strain behavior matches the analytical predictions. However, in the FC solution the chemical potential is initialized in the simulation setup but then allowed to evolve as the body is deformed, resulting in solutions which deviate from the analytical predictions. The cause of the deviation is investigated.

We start by deriving the analytical solutions with the Zhang formulation, which should be equivalent to the incompressible Neohookean VSEC formulation with the Flory-Huggins incompressible stress coupled chemical potential, Equation (8.22). It should be noted that the osmotic pressure used within is defined as the negative of the osmotic pressure used by Zhang and co-workers [58, 34]. Applying the appropriate stress transformation rule (8.1) to Zhang's nominal stress tensor formula (3.47) we arrive at the following equation for the Cauchy stress tensor.

$$\boldsymbol{\sigma} = \frac{\mu_0}{J}\left[\mathbf{B} - \boldsymbol{\delta}\right] + \frac{1}{\Omega}\left[R_g T\left(\ln\left[\frac{J-1}{J}\right] + J^{-1} + \frac{\chi}{J^2}\right) - \mu_c\right]\boldsymbol{\delta} \tag{5.31}$$

Knowing that the true stress in two of the three principal directions are zero, $\sigma_2 = \sigma_3 = 0$, we solve for the chemical potential, μ_c.

$$\mu_c = \frac{\mu_0 \Omega}{J}\left[\frac{J}{\lambda} - 1\right] + R_g T\left[\ln\left[\frac{J-1}{J}\right] + J^{-1} + \frac{\chi}{J^2}\right] \tag{5.32}$$

Then inserting the chemical potential into the equation for the stress in the stretch direction we arrive back at equation (5.30). This derivation verifies that the Zhang

solutions should indeed match the VSEC solutions. Because only the Zhang FC stress solutions deviate from their analytical counterparts, we know that discrepancy can be attributed to deviations in the chemical potential solution. Figure 5.17 shows the chemical potential solutions for the various models plotted with the analytical chemical potential solution.

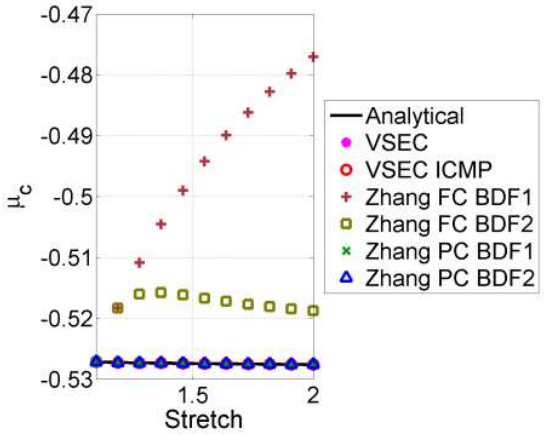

Figure 5.17: Chemical potential vs. stretch

Deviations can be attributed to the nominal concentration time rate of change ($\dot{C}$) term. Assuming the test is performed on a unit cube we can use the following relation to represent the stretch in terms of the displacement in the direction of the principal stretch at the outer corner.

$$\lambda_1 = \frac{\partial u_1}{\partial X} + 1 = u_{o1} + 1 = \lambda \tag{5.33}$$

u_1 is the displacement field in the direction of the principal stretch, and u_{o1} is the displacement in the direction of the principal stretch at the outer corner. Using the above formula we can represent the deformation gradient, it's inverse, and it's time

derivative as functions of u_{o1} with the following three equations respectively.

$$\mathbf{F} = \begin{bmatrix} u_{o1}+1 & 0 & 0 \\ 0 & \sqrt{\frac{J}{u_{o1}+1}} & 0 \\ 0 & 0 & \sqrt{\frac{J}{u_{o1}+1}} \end{bmatrix} \tag{5.34}$$

$$\mathbf{F}^{-1} = \mathbf{F}^{-T} = \begin{bmatrix} (u_{o1}+1)^{-1} & 0 & 0 \\ 0 & \sqrt{\frac{u_{o1}+1}{J}} & 0 \\ 0 & 0 & \sqrt{\frac{u_{o1}+1}{J}} \end{bmatrix} \tag{5.35}$$

$$\dot{\mathbf{F}} = \begin{bmatrix} \dot{u}_{o1} & 0 & 0 \\ 0 & \frac{-1}{2}\sqrt{\frac{J}{(u_{o1}+1)^3}}\dot{u}_{o1} & 0 \\ 0 & 0 & \frac{-1}{2}\sqrt{\frac{J}{(u_{o1}+1)^3}}\dot{u}_{o1} \end{bmatrix} \tag{5.36}$$

Applying the equation for $\dot{C}$ (3.50) we can verify that the term should be identically zero.

$$\dot{C} = \frac{J}{\Omega}\left[\frac{\dot{u}_{o1}}{u_{o1}+1} + 2\frac{-\dot{u}_{o1}}{2}\sqrt{\frac{J}{(u_{o1}+1)^3}}\sqrt{\frac{(u_{o1}+1)}{J}}\right] = \frac{J}{\Omega}\left[\frac{1-1}{u_{o1}+1}\right]\dot{u}_{o1} = 0 \tag{5.37}$$

However, in order for the above identity to hold in the finite element simulations the time derivatives of the displacements must be accurately computed. In the simulations the deformation state is controlled by applying a first order time varying x displacement on the driving face. Therefore, the x displacement can be represented as

$$u_x = X\left(mt + b\right) \tag{5.38}$$

where t is time and m and b are constants. Because the material is incompressible, and no material is added or removed we know that the deformation gradient determinant must remain constant and it's time derivative must be zero.

$$\dot{J} = 0 = \dot{\lambda}_1\lambda_2\lambda_3 + \lambda_1\dot{\lambda}_2\lambda_3 + \lambda_1\dot{\lambda}_2\lambda_3 = \dot{\lambda}_1{\lambda_2}^2 + 2\lambda_1\lambda_2\dot{\lambda}_2 = \dot{u}_x\frac{J}{\lambda} + 2\lambda\sqrt{\frac{J}{\lambda}}\dot{u}_y \tag{5.39}$$

Then solving for $\dot{u}_y$ which should be equal to $\dot{u}_z$ we can represent the time derivative of the displacement vector with the following equation.

$$\dot{\mathbf{u}} = \begin{bmatrix} \dot{u}_x \\ \dot{u}_y \\ \dot{u}_z \end{bmatrix} = \begin{bmatrix} Xm \\ -X\frac{m}{2}\sqrt{\frac{J}{(1+X(mt+b))^3}} \\ -X\frac{m}{2}\sqrt{\frac{J}{(1+X(mt+b))^3}} \end{bmatrix} \tag{5.40}$$

The time derivative of the x displacement is zero order in time, so this time solver should have no problem adequately computing it. However, the time derivatives of the y and z displacements are rational functions of time which cannot be adequately computed with low order time solvers. The time solvers inability to adequately compute the time derivatives of the y and z displacements is directly responsible for the deviations observed in the simulations with the Zhang model. Figure 5.18 shows values that various finite difference schemes compute for the $\dot{C}$ term responsible for the deviations.

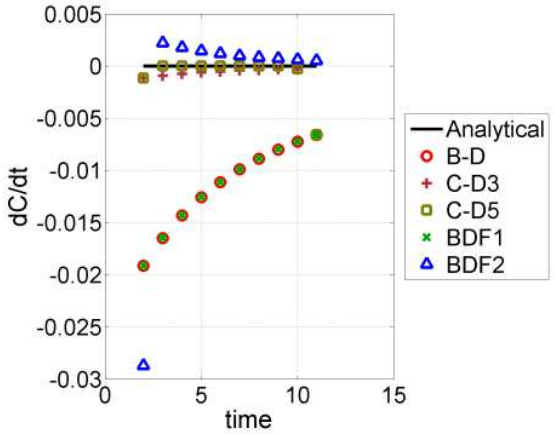

Figure 5.18: $\dot{C}$ vs time for various finite difference schemes.

Both "BDF" lines show data taken directly from simulations with first and second order in time backward difference formulas, and the rest show values computed outside of the finite element code with other finite difference schemes. "B-D" represents a two point backward difference formula, "CD-3" represents a three point central difference scheme, and "CD-5" represents a five point central difference schemes. The equation

used in computing the "B-D" points is identical to the equation implemented in the finite element code for the "BDF1" time solver, and the points are coincident. As is expected the five point central difference scheme does the best job of computing $\dot{u}_y$ and $\dot{u}_z$ and therefore $\dot{C}$. This investigation of the Zhang et al. [58] formulation shows that while it can be used to solve stretching problems on swollen incompressible bodies with a finite element formulation, high order finite difference schemes must be used to adequately compute velocities and prevent non-physical material generation.

Table 5.10: Swollen Simple Stretching Simulation Parameters

Symbol	Value	Units	Description
E	1.2e5	Pa	Young's modulus
ν	0.4999	-	Poisson's ratio
ν_{ICMP}	0.5	-	Poisson's ratio (incompresible)
Ω	6.022e-5	m^3/mol	Species partial molar volume
D	8.0e-10	m^2/s	Species diffusion coefficient
$\Omega C_{\max}$	32.23	-	Non-dimensional maximum nominal concentration
ΩC_s	7.4578	-	Non-dimensional surface nominal concentration
χ	0.2	-	Enthalpy of mixing parameter
R_gT	2.409e3	J/mol	Thermal energy energy per mol

5.2.4 Analytical: Concentration Induced Swelling of Constrained Body

The non-linear elastic mechanical models have been effectively validated, but swelling phenomena up until now have been ignored. To verify that the model swells the appropriately two simple incompressible swelling tests are performed by setting the Poisson's ratio to 0.49975 and fixing the concentration field at 1. The swelling model is tested with two different problem setups based on the uniaxial stretching and equi-triaxial stretching tests depicted in Figure 5.8. All faces without arrows are constrained

with slip conditions. For the uniaxial test the stretch coefficient, ω, is set to 1, and as was expected the cube doubled in volume by doubling it's length in the x direction. For the equi-triaxial test the stretch coefficient, ω, is set to 7, and as was expected the cube swelled to 8 times it's original volume by doubling it's length in all directions.

5.2.5 Analytical: Diffusion in Deforming Body

The non-linear elastic mechanical models have been completely validated, so in the following studies we work towards validating the model for diffusion on a deforming body. For simple deformation cases with prescribed concentration and pressure fields fluxes can be determined analytically. The flux equation implementation is validated on bodies undergoing uniaxial and equi-triaxial deformation illustrated in Figure 5.8. The uniaxial tests are used to validate the fluxes computed by the plane-strain and 3D elements, and the equi-triaxial tests are used to validate the fluxes computed by the linear and quadratic bar elements and the 3D elements.

5.2.6 Finite Difference: Galvanostatic Insertion into Incompressible Sphere (Fully Coupled)

It has been verified that all of the individual pieces of the finite deformation diffusion models are correctly implemented, so the next task is to verify that they all work correctly together. Zhao et al. [61] developed a mechanically incompressible fully coupled finite deformation model with plastic deformation. Their model was developed in a very similar manner to ours, so efforts have been made to reproduce the results that they report that don't include plastic effects. Zhao's results were computed using a finite differencing method. The comparison problem is a 1μm radius sphere subjected to galvanostatic insertion is simulated. The material properties and constants used in the simulations are presented in Table 5.11. The published results from Zhao et al. [61] are pictured below (Figure 5.19).

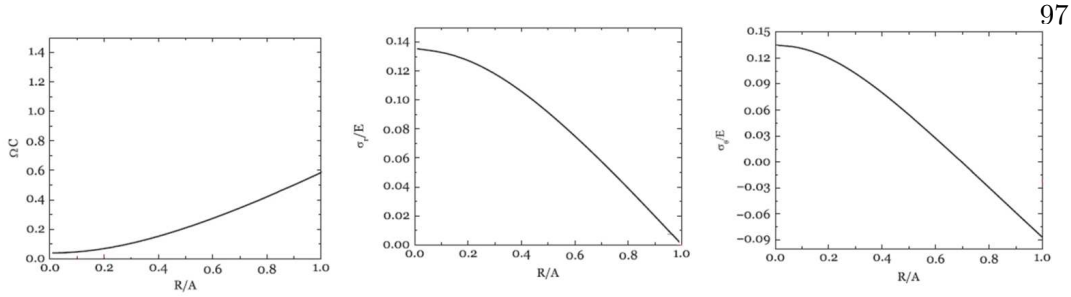

(a) (b) (c)

Figure 5.19: Profiles of non-dimensional values taken at t = 480s (a) concentration, (b) radial stress, (c) tangential stress.

The problem was simulated using 60 quadratic 3 node bar elements who's formulation is described in section 3.1.3. The TSEC form of the material model as described in section 3.2.6, with mechanical and chemical models described in [61]. Material properties and parameters used in the problem setup are listed in Table 5.11. Figure 5.20 shows the results produced with the femdoc models.

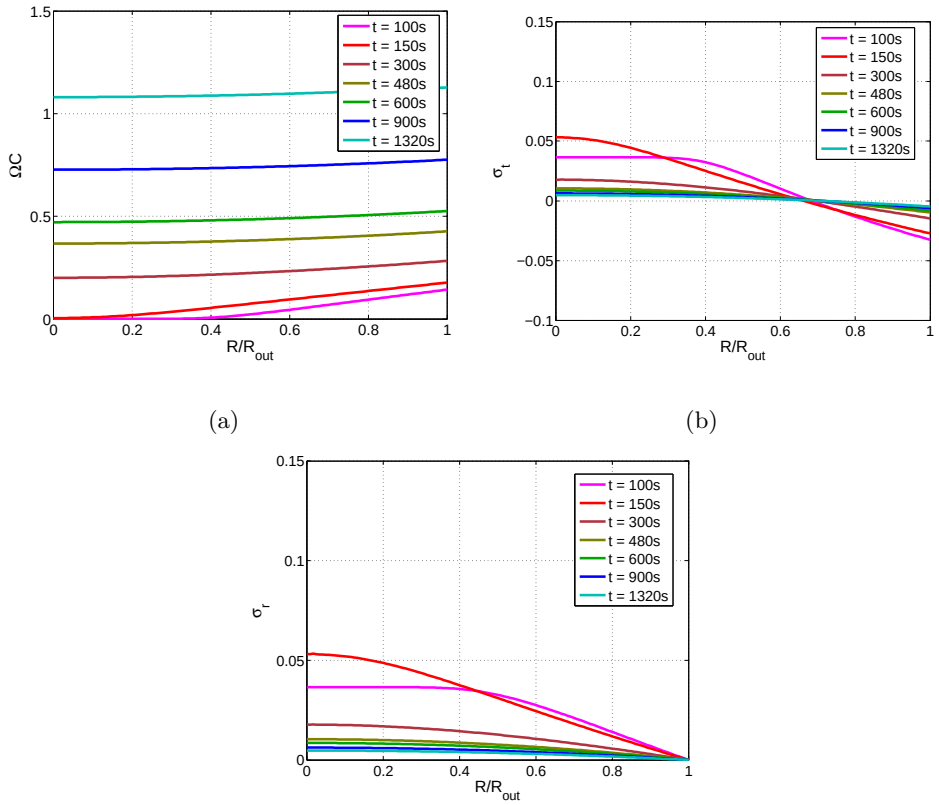

Figure 5.20: Profiles of non-dimensional values taken at various times (a) concentration, (b) radial stress, (c) tangential stress.

There are clearly some considerable discrepancies between the solutions published in Zhao et al. [61] shown in Figure 5.19 and the solutions produced by our models shown in Figure 5.20. Because the concentration profile at 480s in our simulation is so much flatter than Zhao's, it was concluded that our model is predicting much larger fluxes. To track down the source of the discrepancy the flux equations were investigated. Zhao used a chemical potential of the following form.

$$\mu_c = \mu_c 0 + R_g T \ln\left(\frac{C}{1+\Omega C}\right) - \Omega\sigma_h \tag{5.41}$$

Zhao used an sphere particle formulation, which assumes there is only flux in the radial direction. Inserting Equation (5.41) into Equation (2.23) and specifying to spherical

symmetry we arrive at the following equation for the radial flux.

$$J_r = -M\left[\left(\frac{R_gT}{C} - \frac{\Omega R_gT}{1+\Omega C}\right)\frac{\partial C}{\partial R} - \Omega\frac{\partial \sigma_h}{\partial R}\right] \tag{5.42}$$

where M is the mobility and is computed as

$$M = \frac{CD}{R_gT{\lambda_r}^2} \tag{5.43}$$

λ_r is the radial stretch. Assuming incompressibility and a constant nominal surface flux we arrive at the following relation between time and the ratio of the reference volume to the current volume.

$$\frac{V}{V_0} = 1 + \left(\frac{V_{\max}}{V_0} - 1\right)\frac{t}{t_{\max}} = \left(\frac{r_0}{R_0}\right)^3 = {\lambda_\theta}^3 \tag{5.44}$$

Then the hoop stretch at the surface can be computed as

$$\lambda_\theta = \left[1 + \left(\frac{V_{\max}}{V_0} - 1\right)\frac{t}{t_{\max}}\right]^{1/3} \tag{5.45}$$

The quantity $\frac{V_{\max}}{V_0}$ can be computed by using the incompressibility condition ($\frac{V_{\max}}{V_0} = 1+\Omega C_{\max} = 4$). Next using the incompressibility condition, $\det(\mathbf{F}) = \lambda_r{\lambda_\theta}^2 = 1+\Omega C$, we arrive at the following formula for the radial stretch at the surface as a function of time and concentration.

$$[\lambda_r = \frac{1+\Omega C}{{\lambda_\theta}^2} = (1+\Omega C)\left[1 + \left(\frac{V_{\max}}{V_0} - 1\right)\frac{t}{t_{\max}}\right]^{-2/3} \tag{5.46}$$

Based on the non-dimensional quantities provided in Zhao's paper, we put the radial flux Equation (5.42) into the following non-dimensional form.

$$\left(\frac{\Omega R_0}{D}\right)J_r = -{\lambda_r}^{-2}\left[\left(\frac{1}{1+\Omega C}\right)\frac{\partial(\Omega C)}{\partial(R/R_0)} - \frac{\Omega E}{R_gT}\left(\frac{\Omega C}{3}\right)\left(\frac{\partial(\sigma_r/E)}{\partial(R/R_0)} + 2\frac{\partial(\sigma_\theta/E)}{\partial(R/R_0)}\right)\right] \tag{5.47}$$

Now the radial flux is in a convenient form for computing what the non-dimensional surface flux should be given the material properties and the published solutions. To preserve continuity the non-dimensional flux computed by Equation (5.47) at the surface

should match the prescribed non-dimensional surface flux ($\frac{\Omega R_0}{D} J_0$). We next extract the following non-dimensional values from Figure 5.19.

$$\begin{bmatrix} \Omega C|_{R=R_0} \approx 0.575 & \frac{\partial(\Omega C)}{\partial(R/R_0)}\Big|_{R=R_0} \approx 0.75 \\ \frac{\partial(\sigma_r/E)}{\partial(R/R_0)}\Big|_{R=R_0} \approx -0.2 & \frac{\partial(\sigma_\theta/E)}{\partial(R/R_0)}\Big|_{R=R_0} \approx -0.2875 \end{bmatrix} \tag{5.48}$$

Then we compute the radial stretch at the surface as shown below.

$$\lambda_r|_{\substack{R=R_0 \\ \text{\&} \\ t=480s}} \approx 1.575\left[1+3\frac{480}{3600}\right]^{-2/3} \approx 1.25853 \tag{5.49}$$

Finally putting all of the pieces together we arrive at the following surface flux.

$$\left(\frac{\Omega R_0}{D}\right) J_{sx}\Big|_{R=R_0} \approx -1.25853^{-2}\left[\left(\frac{0.75}{1.575}\right) - 263\left(\frac{0.575}{3}\right)(-0.2 - 2\cdot 0.2875)\right] \approx 24.96 \tag{5.50}$$

The computed surface flux is an order of magnitude larger than the prescribed surface flux, see Table 5.11, indicating an inconsistency. Diving a little deeper, we prescribed a graphically matched concentration profile in our model to see what stresses and fluxes result. With the prescribed concentration profile the resulting stresses very closely match those shown in Figure 5.19. There are minor discrepancies in stress gradients at the particle center and surface but not enough to account for the order of magnitude of difference in fluxes. Furthermore, the fluxes computed by our model that result from prescribing the concentration field are also an order of magnitude larger than the prescribed surface flux. We therefore conclude that there is an inconsistency in the results published in Zhao et al. [61].

Table 5.11: Simulation Parameters for Comparison with Zhao

Symbol	Value	Units	Description
E	8.0e10	Pa	Young's modulus
ν	0.5	-	Poisson's ratio
Ω	8.190e-6	m^3/mol	Species partial molar volume
$C_{max}\Omega$	3.0	-	Non-dimensional maximum concentration
D	1.0e-16	m^2/s	Species diffusion coefficient
$\frac{\Omega E}{R_g T}$	263	-	Coupling parameter
$\left(\frac{\Omega R_0}{D}\right) J_0$	2.8	-	Non-dimensional surface flux
$t_{\max}$	3600	s	Ideal time to fill particle

5.2.7 Finite Element: Hydrogel Problems

With a lack of published results for finite deformation coupled stress-diffusion problems in the context of battery electrodes, verification problems had to be found in other fields. Two papers by Suo and co-workers focus on the some of the details of modeling coupled nonlinear elastic deformation and diffusion of water through hydrogels [34, 58]. The following tests are used to verify the fully coupled finite deformation electrode particle element in Section3.1.3 with the VSEC mechanical models and the Flory-Huggins incompressible stress coupled chemical potential, Equation (8.22), and the finite deformation hydrogel element in Section3.1.4. Suo employed the following transformation so that the chemical potential could be used as a state variable.

$$\hat{W} = W - C\mu_c \tag{5.51}$$

With the chemical potential as a state variable the free swelling can be simulated by enforcing that the surface potential is equal to zero. Because the hydrogel element uses chemical potential state variables to control diffusion, chemical potential boundary conditions can readily be enforced. However, in order to enforce surface chemical potentials

with the finite deformation electrode particle element some form of boundary integral must be evaluated. Two techniques for enforcing the surface potential condition are implemented. In the first technique chemical potential state variables are introduced everywhere with the addition of the following state equation.

$$\delta W_{\mu_{cs}} = \int_{\Omega} \delta\mu_{cs} \left[\mu_{cs} - \mu_c \left(C, p_o\right)\right] = 0 \tag{5.52}$$

μ_{cs} is the new chemical potential state variable, and $\mu_c \left(C, p_o\right)$ is the true chemical potential evaluated with the Flory-Huggins incompressible stress coupled chemical potential. The new state variable drives surface flux by replacing the surface integral in Equation 3.13 with the following term.

$$\int_{\Gamma_0} \delta C \left(-\mathbf{M}\nabla^0 \mu_{cs}\right) \cdot \mathbf{n}_0 d\Gamma_0 \tag{5.53}$$

The other method for controlling the surface flux with a chemical potential condition is based the local Lagrange multiplier method described in section 4.2. We use a Lagrange multiplier, Π, to represent the surface flux and replace the surface flux integral by

$$\int_{\Gamma_0} \delta C \Pi d\Gamma_0 \tag{5.54}$$

Then the following governing equations are used to evolve the new variable on the surface.

$$0 = \gamma \int_{\Gamma_0} \delta\Pi \left(\Pi - \mathbf{J} \cdot \mathbf{n}_0\right) d\Gamma_0 + \int_{\Gamma_0} \delta\Pi \left(\mu_c - \mu_{c0}\right) d\Gamma_0 \tag{5.55}$$

μ_c is the true chemical potential on the surface, μ_{c0} is the prescribed surface potential, and γ is a constant that determines how well the constraint is enforced. The first term is know as the compatibility condition, and the second is the constraint. Treating Π as a constant over each surface element the new variable can be condensed out as follows

$$\Pi = \frac{\int_{\Gamma_0} \delta\Pi \mathbf{J} \cdot \mathbf{n}_0 d\Gamma_0 + \frac{1}{\gamma} \int_{\Gamma_0} \delta\Pi \left(\mu_c 0 - \mu_c\right) d\Gamma_0}{\int_{\Gamma_0} \delta\Pi d\Gamma_0} \tag{5.56}$$

For future reference the method of chemical potential boundary enforcement represented by Equation (5.53) will be referred to as the "State Variable Method"; the other method for enforcing a chemical potential controlled flux boundary will be referred to a the "Local Lagrange Multiplier Method".

With all of the pieces in place we start with a simple 1D hydrogel problem. The first problem considered involves a hydrogel draining under a weight. An initially unconstrained hydrogel is allowed to equilibrate under free swelling conditions, zero surface chemical potential, then the gel is placed in a box constraining the X and Y faces from spreading under an applied pressure. Then a weight is plasec on a rigid permeable plate on top of the gel changing the chemical potential of the gel and causing water to slowly drain from the hydrogel. The figure below (5.21) illustrates the problem setup.

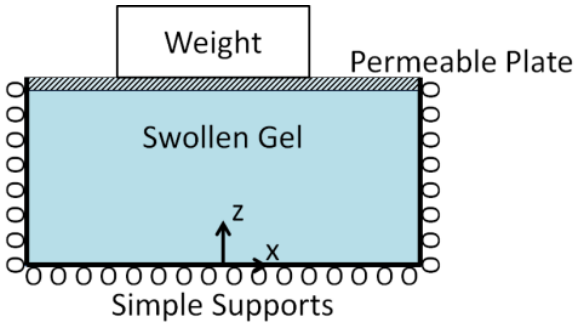

Figure 5.21: Diagram of gel draining under weight problem

Because the problem is 1D in space with a constant surface pressure and chemical potential, we know the concentration on the surface must also be constant. Therefore, either of the above methods can be used to enforce the surface chemical potential constraint, but the problem could be equivalently be set up by applying the same surface pressure with a potentiostatic boundary condition. The problem was first simulated with the chemical potential constraint enforced with each method, then the equivalent

simulation was run with a Derichlet concentration boundary condition that was taken from the other simulations. The weight is simulated by integrating a constant nominal pressure, p_s, over the surface. Material properties and parameters used in the hydrogel simulations are listed in Table 5.12. The figures below (5.22) show the results of the three simulations with the results from Zhang et al. [58] overlaid.

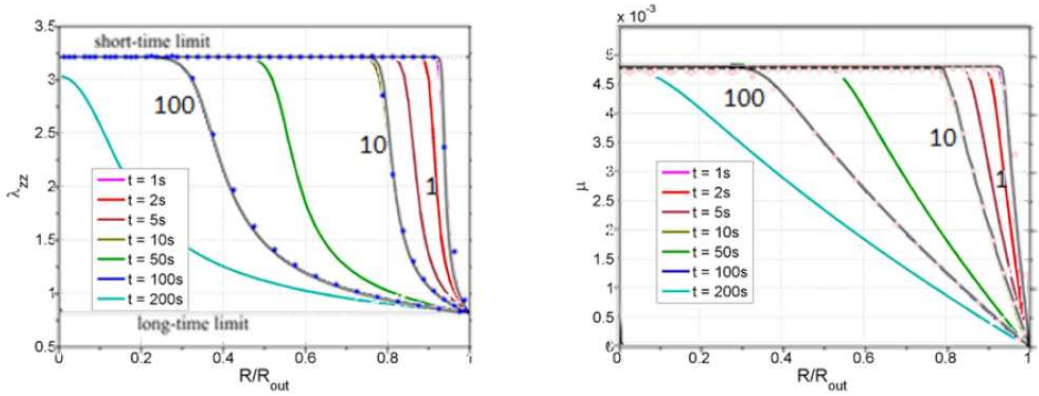

(a) (b)

Figure 5.22: State Variable Method (a) z stretch, (b) chemical potential.

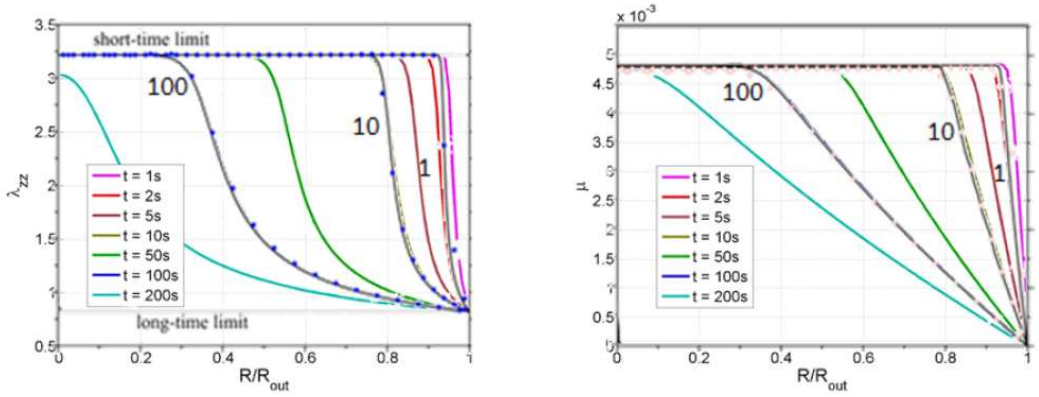

(a) (b)

Figure 5.23: Local Lagrange Multiplier Method (a) z stretch, (b) chemical potential.

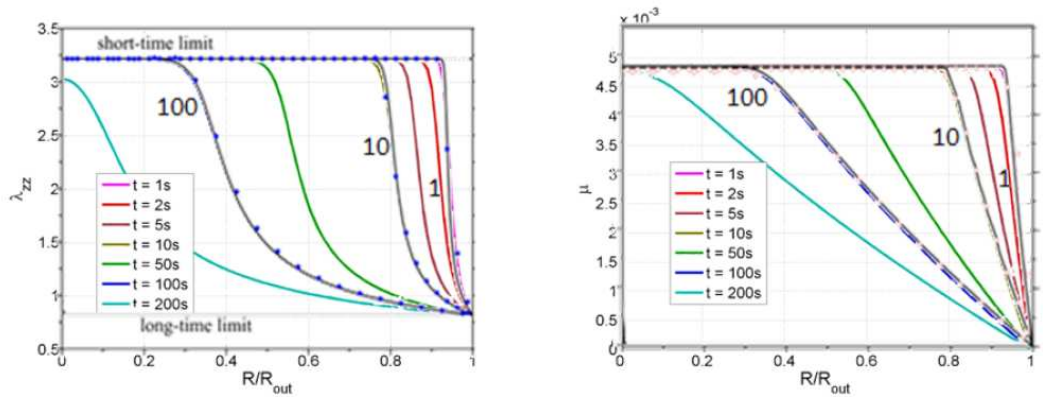

(a) (b)

Figure 5.24: Potentiostatic with pressure (a) z stretch, (b) chemical potential.

In Figures 5.22, 5.23, and 5.24 the colored lines are the results from our finite element simulations, the black lines are Zhang's results from a finite difference model, and the blue dots are Zhang's results from a finite element model. All three of our simulations were run on a 1x1x100 mesh of 20 node quadratic brick elements. All three methods effectively simulate this problem. Furthermore, the agreement of the potentiostatic simulation verifies our understanding of the link between concentration, pressure, and chemical potential. All of the pictured results were produced with compressible formulations, but the incompressible formulations produced equivalent results.

Next efforts were made to reproduce the free swelling cube results from Zhang et al. [58]. In this problem an initially dry unit cube of hydrogel is placed in water and allowed to swell freely until it reaches an equilibrium state. The published results only show the deformed cube with stress contours plotted on the surface at four times. We show the equivalent results produced by our simulation. The results plotted below were produced by simulating one eight of the domain with 512 eight node hexahedral incompressible hydrogel elements described in Section 3.1.4.

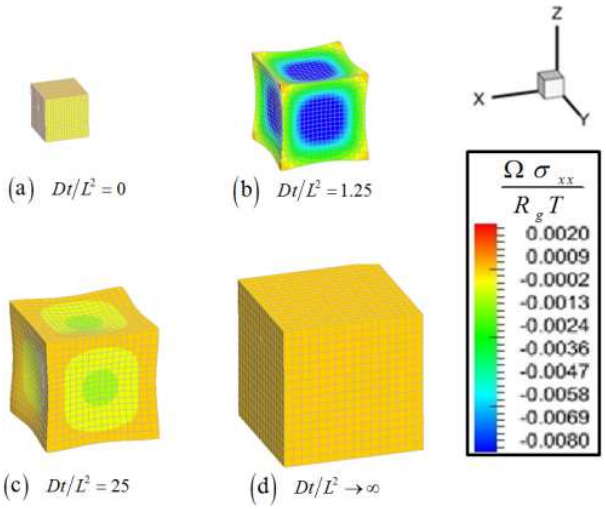

Figure 5.25: Snapshots of swelling cube with non-dimensional stress contours

The formulation is highly unstable, and the nonlinear solves during the first time steps had to be severely under-relaxed. Also, the simulation had to be started with tiny time steps. The sizes of the time steps were slowly increased so a steady state solution could be found without too much computational cost. It should be noted that the formulations presented in [58] are difficult to solve using numerical techniques and without some form of stabilization many problems, including this free swelling cube problem, will be non-convergent. The results closely match their published counterparts verifying the implementation of the hydrogel element.

Table 5.12: Simulation Parameters for Comparison with Zhang

Symbol	Value	Units	Description
E	1.2e5	Pa	Young's modulus
ν	0.499999	-	Poisson's ratio
Ω	6.022e-5	m^3/mol	Species partial molar volume
D	8.0e-10	m^2/s	Species diffusion coefficient
$\Omega C_{\max}$	32.23	-	Non-dimensional maximum nominal concentration
ΩC_s	7.4578	-	Non-dimensional surface nominal concentration
χ	0.2	-	Enthalpy of mixing parameter
R_gT	2.409e3	J/mol	Thermal energy energy per mol

5.3 Extended Finite Element Model Verification

In previous sections the finite element implementations are rigorously verified. In order to verify that our XFEM implementations produce meaningful solutions, simulation results produced by using our standard FEM implementation are compared with equivalent results generated with our XFEM implementation. First the mechanical models, including the no slip interface condition, are verified with a cantilever beam problem. Then the full electrode models are verified with a Li half cell problem.

5.3.1 Cantilever Beam FEM vs XFEM

A cantilever beam problem is studied with standard FEM models using body fitted meshes and XFEM models. Using XFEM the model, the problem is set up in two different ways. In the first setup (referred to as the one phase XFEM beam) the beam is only half of the domain. The other half of the domain treated as void and the beam separates from the void phase. In the second setup (referred to as the two phase XFEM beam) the beam is made of two identical phases, and it fills the whole domain. Diagrams of the three different ways of setting up the problem are shown in

the following figure.

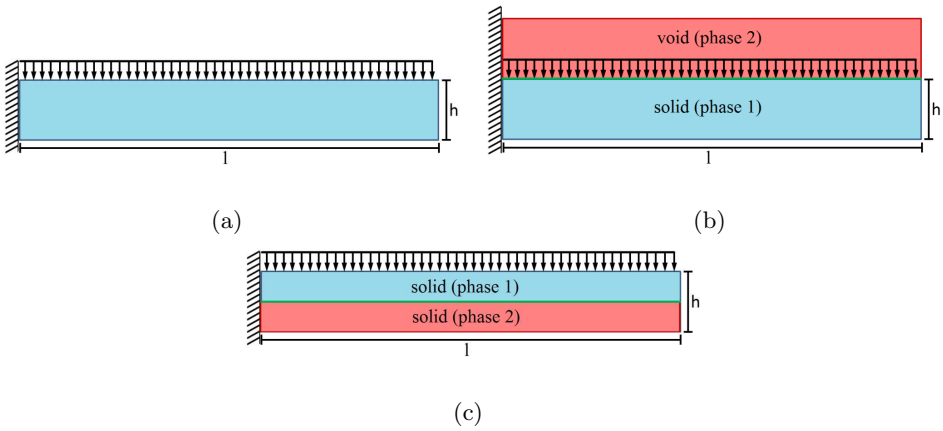

Figure 5.26: Cantilever beam with distributed load (a) One phase FEM beam, (b) One phase XFEM beam, (c) Two phase XFEM beam.

The beam problems are setup as dimensionless. The beam is 1 length unit thick and 20 length units long. The surface pressure (p_s) is chosen such that significant deformation is predicted. A large pressure is chosen to facilitate the verification of the XFEM finite deformation mechanics. The one phase XFEM beam problem is used to demonstrate that we can correctly integrate distributed loads on XFEM interfaces. The two phase XFEM beam problem is used to demonstrate that the interface continuity conditions work correctly. The parameters used in the simulations are presented in the following table.

Table 5.13: Simulation Parameters for Cantilever Beam Study

Symbol	Value	Units	Description
E	1.0	-	Non-dimensional Young's modulus
ν	0.25	-	Poisson's ratio
p_s	5.0e-5	-	Non-dimensional surface pressure
γ_{LLM}	-1.0e3	-	LLM constraint scaling parameter
γ_{Nit}	1.0e2	-	Nitsche constraint scaling parameter

In the following mesh refinement studies the X axes show the number of elements in the length direction. In each simulation the number of elements in the thickness direction is chosen such that the elements remain square, so the number of elements in the length direction are incremented by 20 and the number of elements in the thickness direction are incremented by one during mesh refinement. The one phase XFEM beam problem is however an exception because the XFEM domain is twice as thick as the beam domain.

Figure 5.27(a) demonstrates that with mesh refinement, all three problem formulations converge on the same results. Furthermore by comparing the convergence behaviors of the two different methods for satisfying displacement continuity it appears that both methods show very similar mesh refinement behavior. To further investigate the behaviors of the two displacement continuity formulations the interface displacement jumps are presented in Figure 5.27(b).

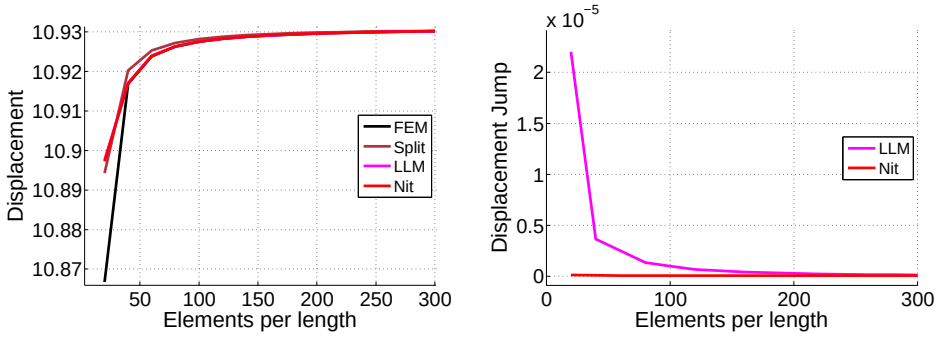

(a) (b)

Figure 5.27: Mesh refinement results (a) Tip displacement, (b) XFEM interface displacement jump.

In Figure 5.27 "FEM" represents the one phase FEM beam, "Split" represents the one phase XFEM beam, "LLM" represents the two phase FEM beam with the Local Lagrange Multiplier displacement continuity formulation, and "Nit" represents the two phase FEM beam with the Nitsche displacement continuity formulation. Shown in

Figure 5.27 the Nitsche does a better job of satisfying displacement continuity, but with mesh refinement the displacement jump computed when using the Local Lagrange Multiplier method appears converge on the jump computed when using the Nitsche method. Furthermore, even on the most coarse mesh the displacement jumps are more than five orders of magnitude smaller than the computed displacement of the beam tip.

The cantilever beam studies are used to demonstrate that our treatment equilibrium mechanics within the XFEM framework produces accurate and reliable results. The two phase XFEM beam problems demonstrate that both implemented methods for satisfying interface displacement continuity work and are nearly equivalent. The One phase XFEM beam problem demonstrates that we can accurately integrate loads on XFEM interfaces. There are many more studies that should be performed to rigorously verify the XFEM implementations, but this work will be left for colleagues and future researchers.

5.3.2 Si Cylinder in Electrolyte (Half Cell) FEM vs XFEM

In efforts to verify the fully coupled finite deformation-transport XFEM implementation a simple Li half-cell problem is studied. The half-cell consists of a cylinder of Si embedded in a cube of electrolyte with Li foil on the top and bottom of the cube. Lithiation is controlled by an applied electric potential difference between the Si and the Li foil. A diagram of the problem is illustrated in Figure 5.28.

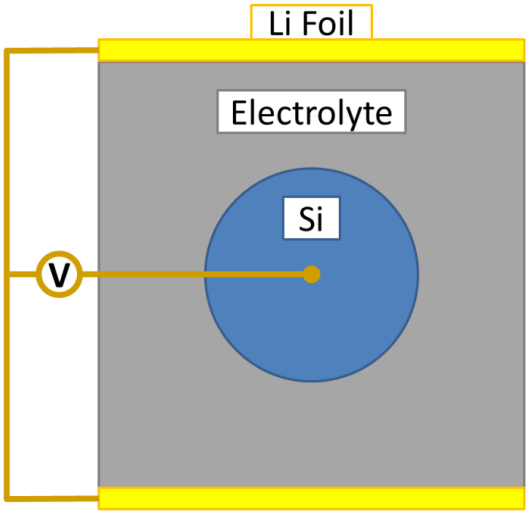

Figure 5.28: Li-Si half cell problem

Using the symmetries in the x and y axes through the center of the cylinder only 1/4 of the domain is actually simulated and the problem is simplified to 2D by assuming plane-strain. Example body-fitted and XFEM meshes used for simulating the example half-cell problem are pictured below.

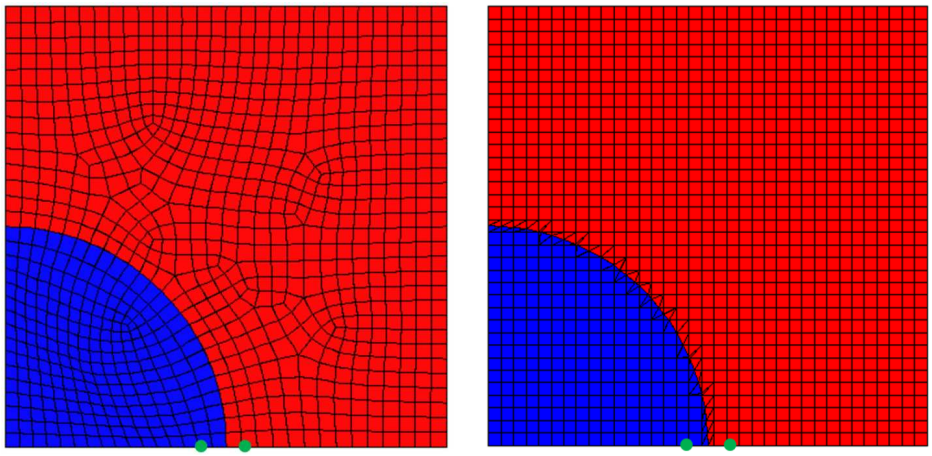

(a) (b)

Figure 5.29: Example Half-Cell Meshes (30x30 grids) (a) body-fitted mesh, (b) XFEM mesh.

The green dots represent the locations where variables are plotted. Plotting loca-

tions where chosen near the interface because most of the differences between standard FEM and XFEM are localized to interfaces. The problem is convenient for testing the XFEM battery models because it incorporates all piece developed for simulating battery electrodes in one simulation, including: finite deformation mechanics in swelling bodies, interface displacement continuity, species transport through electrode host materials, ion transport through binary electro-neutral electrolytes, Butler-Volmer electrode electrolyte interface reaction kinetics. Furthermore, the simple geometry allows for easy comparison with standard FEM models. The displacement continuity condition has been shown to work, so displacement data won't be presented again. The half-cell problem was simulated with varying mesh densities. Parameters and material properties used in setting up the problem are listed in Table 5.14. State variables at the specified locations in the electrode particle and electrolyte are plotted over time. The evolutions of phase 1 and phase 2 state variables over time are presented for the various mesh densities in Figures 5.30 and 5.31 respectively.

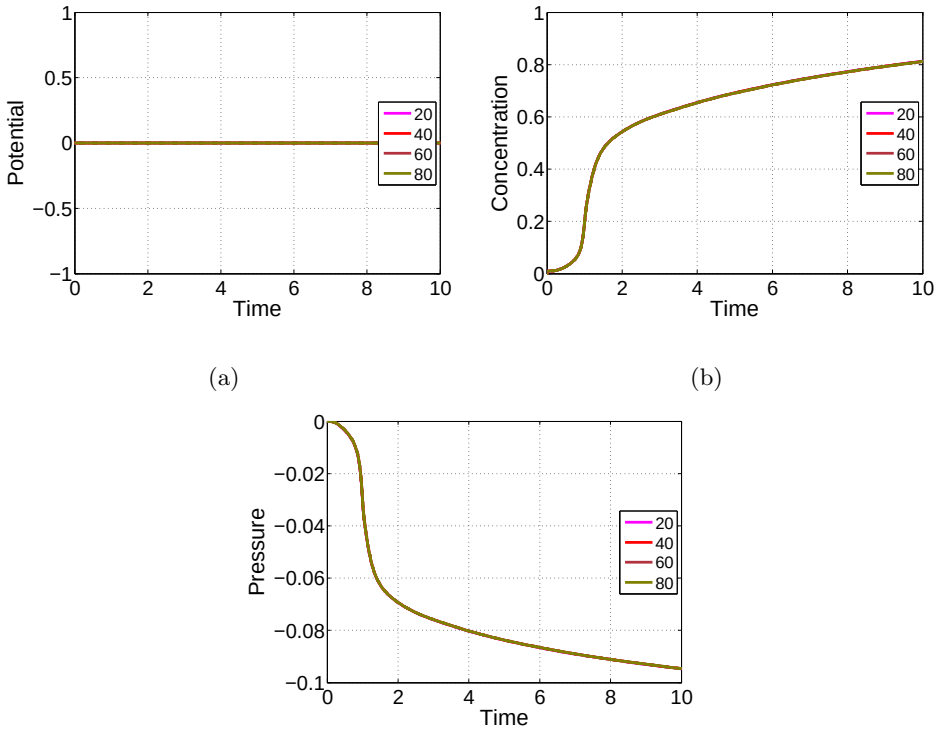

(a) (b)

(c)

Figure 5.30: Half-Cell problem phase 1 solutions at various mesh densities (FEM solutions are solid lines, XFEM solutions are dashed lines) (a) Electric Potential, (b) Concentration, (c) Hydrostatic Stress.

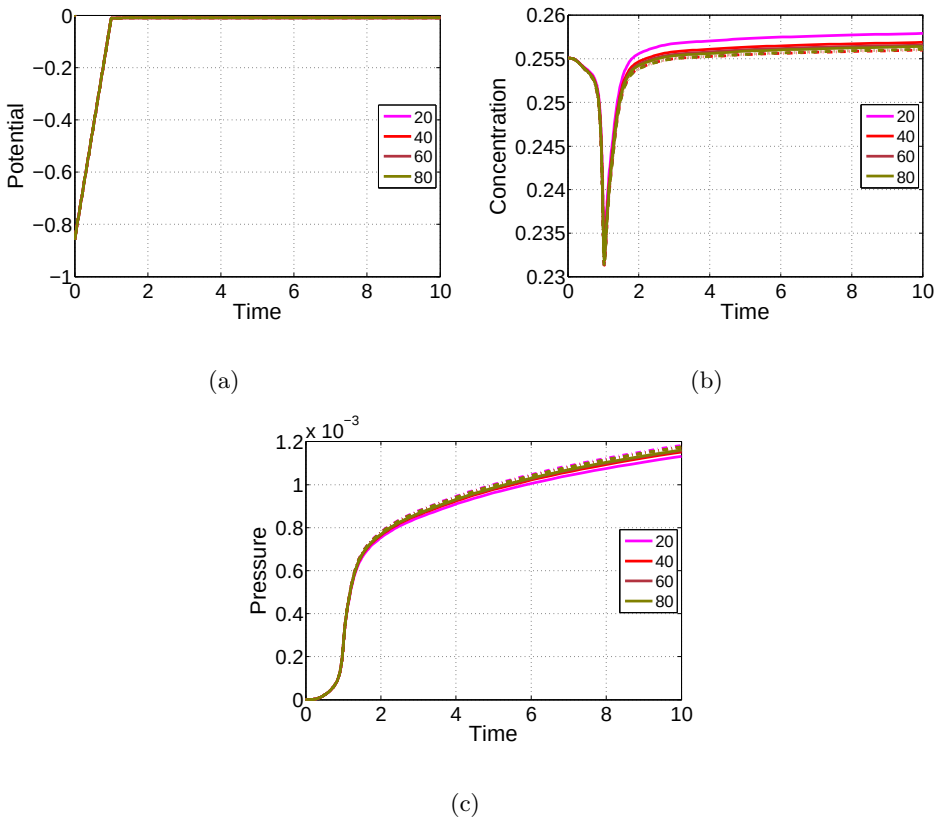

Figure 5.31: Half-Cell problem phase 2 solutions at various mesh densities (FEM solutions are solid lines, XFEM solutions are dashed lines) (a) Electric Potential, (b) Concentration, (c) Natural Log of the Determinant of the Deformation Gradient.

The different colors represent solutions computed on different mesh densities, for example "20" represents solutions computed on a 20x20 grid. All of the lines in the phase one variable plots (Figure 5.30) lie almost directly on top of one another, providing confidence that the standard FEM and XFEM models are nearly equivalent. Mesh refinement appears to have little impact on the phase one solutions, but it should be noted that the XFEM problem did not converge when attempts were made to run it on a coarser mesh. While the phase 1 solutions great agreement, the phase 2 solutions do show some deviation. By examining the plots in Figure 5.31 it can be observed that the FEM and XFEM "concentration" and "pressure" solutions show some deviation. The largest deviation between the fem and XFEM solutions are seen on the most

coarse mesh, but with mesh refinement the FEM and XFEM solutions approach one another. Although the phase two solutions are more significantly impacted by switching to XFEM, both models appear to approach the same solution with mesh refinement. Furthermore, even though there is some deviation in the phase two solutions, all models even on the most coarse grids produce very similar trends. Having established that the XFEM solutions produce meaningful and reliable results the new tool can be used in electrode design problems with much greater confidence.

Table 5.14: Simulation Parameters for Li-Si Half Cell Problem

Symbol	Value	Units	Description
$\tilde{E}_1$	1.124e11	Pa	Young's modulus Silicon
$\tilde{E}_2$	1.124e10	Pa	Young's modulus Electrolyte
ν_1	0.28	-	Poisson's ratio Silicon
ν_2	0.475	-	Poisson's ratio phase 2
Ω	8.190e-6	m^3/mol	Partial molar volume of Li
C_{max1}	3.663e5	mol/m^3	Maximum nominal concentration Silicon
C_{max2}	3.920e3	mol/m^3	Maximum nominal concentration Electrolyte
C_{01}	3.663e3	mol/m^3	Initial nominal concentration phase 1
C_{02}	1.0e3	mol/m^3	Initial nominal concentration Electrolyte
D_1	1.0e-15	$m^2/2$	Li diffusion coefficient in Silicon
D_{2+}	7.5e-13	$m^2/2$	Li ion diffusion coefficient Electrolyte
D_{2-}	7.5e-13	$m^2/2$	Anion diffusion coefficient Electrolyte
k	1.0e-13	$m^{2.5}/s/mol^{0.5}$	Interface reaction rate coefficient
U'	Baggetto et al. [4]	$m^{2.5}/s/mol^{0.5}$	Open circuit potential of Li in Si
R_gT	2.409e3	J/mol	Thermal energy per mol
F	9.649e4	C/mol	Faraday's constant

Chapter 6

Studies And Discussion

A simple problem involving a cylinder particle immersed in a cube of electrolyte is simulated with various parameters with both the small deformation models and the finite deformation models. The simulation results are used to highlight the importance of including finite deformation mechanics. Next the same cylinder in electrolyte problem is simulated using XFEM and deviations from the body fitted mesh results are discussed. Finally simulation results from a number of particle in electrolyte simulations run on randomly generated XFEM meshes will be used to highlight the versatility of the new tools.

6.1 Small Versus Finite Deformation

While coupled mechanics-diffusion has received a fair amount of attention in the battery modeling community, most researchers take advantage of small deformation approximations to simplify their models [18, 17, 60, 59, 27, 29, 11, 13, 12, 23]. Small deformation approximation models can be useful in providing scientists and designers with insight into the behavior of electrodes during battery operation, but for materials such as silicon which undergo significant deformation during lithiation small deformation approximations can produce misleading predictions. To highlight the importance of using finite deformation model formulations some example particle in electrolyte problem solutions will be discussed. In all of the example problems silicon material properties

from Table 6.1 are used unless otherwise noted.

Table 6.1: Silicon Material Parameters

Symbol	Value	Units	Description
E	1.124e11	Pa	Young's modulus
ν	0.28	-	Poisson's ratio
Ω	8.190e-6	m^3/mol	Li partial molar volume
D	1.0e-15	m^2/s	Diffusion coefficient
C_{max}	3.663e-5	mol/m^3	Maximum Li concentration
k^s	1.0e-13	$m^{2.5}/\left(mol^{0.5}s\right)$	Surface reaction rate

A uniformly stretched spherical $1\mu m$ radius particle of silicon was simulated with no swelling ($\Omega = 0$) and fixed surface concentration. The simulation results do not provide much physical insight because they remove the swelling coupling, which is critical in modeling lithium absorption into silicon, but they highlight the importance of including deformation in the diffusion equations. The initial and boundary conditions used in the problem are listed in the Table 6.2. The problem was simulated on a mesh of 60 bar elements using small and finite deformation sphere-symmetric formulations.

Table 6.2: Initial & Boundary Conditions (diffusion in stretched sphere)

Initial and Boundary Conditions		
$\frac{C}{C_{\max}}\Big\vert_{t=0} = 0.01$	in	Ω_s
$\mathbf{u} = \mathbf{x}$	in	Ω_s
$\frac{C}{C_{\max}} = 1.0$	on	Γ_s

In Table 6.2 Ω_s represents the interior of the sphere particle and Γ_s represents it's surface. By comparing the concentration profiles produced by the small and finite deformation models in Figure 6.1 it is clear that the small deformation model over pre-

dicts the diffusion rate. In this problem there is no species induced swelling, and thus no pressure coupling. Therefore, the differences in the solutions is purely attributed to the fact that small deformation model has no mechanism for capturing the effects of increasing diffusion distances when the cylinder is stretched. In fact when the same simulation is run with no deformation both models predict the same transport behavior predicted by small deformation model. In Figure 6.1 "Concentration" is the concentration normalized by the maximum concentration.

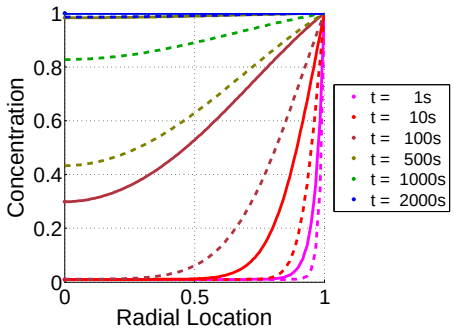

Figure 6.1: Concentration profiles of stretched sphere at various snapshots in time. The small deformation solutions are represented by solid lines and the finite deformation solutions are represented by the dashed lines.

The diffusion in stretched sphere study highlights the importance of considering deformation when modeling diffusion, but neglects the stress coupling effects caused by including specied induced swelling. To investigate the stress coupling effects we again study a $1\mu m$ radius silicon particle, but this time swelling and the Butler-Volmer surface kinetics model is used. This set of simulations is pseudo two phase because the particle is explicitly modeled, but the electrolyte is idealized as fixed and uniform ion concentration and electrolyte electric potential on the particle surface. The initial and boundary conditions used in the pseudo two phase silicon sphere problem are listed in the Table 6.3.

Table 6.3: Initial & Boundary Conditions (pseudo two phase sphere in electrolyte)

Initial and Boundary Conditions		
$\frac{C_s}{C_{s\,\max}}\Big\vert_{t=0} = 0.01$	in	Ω_s
$\mathbf{u} = \mathbf{0}$	at	$\mathbf{x} = \mathbf{0}$
$\phi_s = f(t)$	on	Γ_s
$\frac{C_e}{C_{e\,\max}} = 0.255$	on	Γ_s
$\phi_e = 0.0$	on	Γ_s

In Table 6.2 Ω_s represents the interior of the sphere particle, Γ_s represents the particle surface, and $\mathbf{x} = \mathbf{0}$ represents the particle center. The variables with the underscore "s" are silicon state variables and the variables with the underscore "e" are electrolyte state variables. For example C_s is the neutral lithium concentration within the silicon particle, and C_e is the lithium ion concentration within the electrolyte. To drive the simulation the electric potential of the particle is linearly swept over the open circuit potential in 1000 seconds.

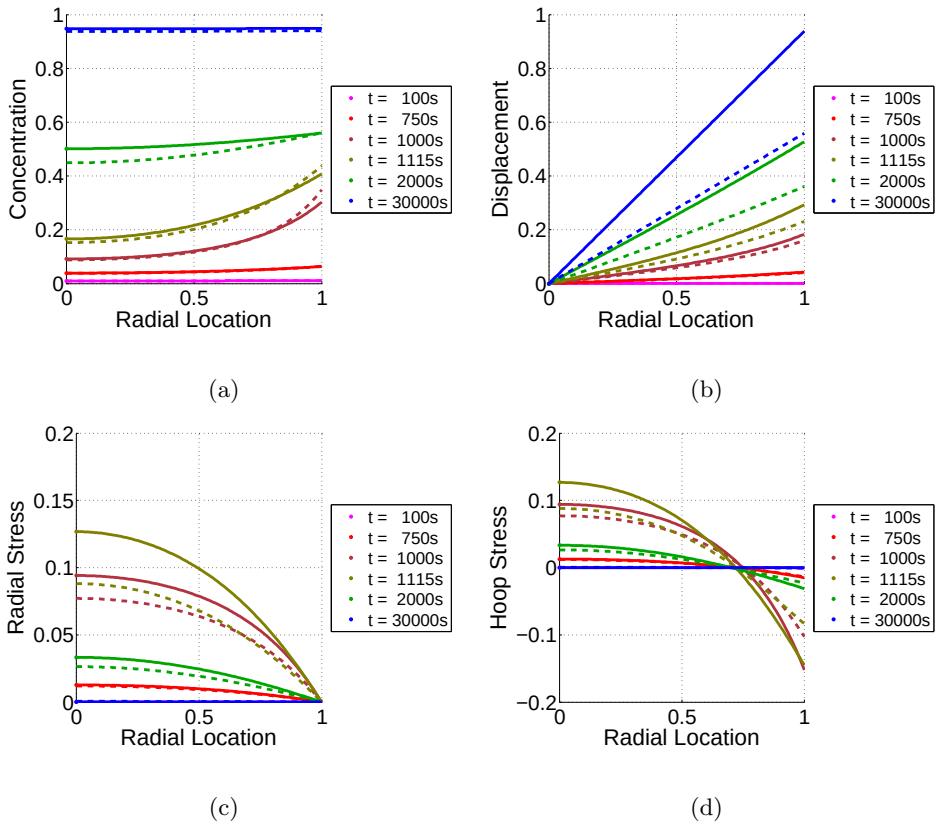

(a) (b)

(c) (d)

Figure 6.2: Pseudo two phase sphere in electrolyte (a) normalized concentration, (b) normalized displacement, (c) normalized radial stress, (c) normalized hoop stress. The small deformation solutions are represented by solid lines and the finite deformation solutions are represented by the dashed lines.

Figure 6.2 shows normalized concentration, normalized displacement, normalized radial stress, and normalized hoop stress profiles at various snapshots in time. There are a number of similarities in the simulation results including similar profile shapes and dffusion rates, but we are more concerned with the differences. By studying Figure 6.2 it can be observed that the small deformation over predicts diffusion rates, swelling, and elastic stresses. The diffusion rate over predictions could cause designers to expect faster charging times. Furthermore, due to swelling inaccurate diffusion predictions cause inaccurate mechanics predictions. It is clear by examining Figures 6.2(b), 6.2(c), and 6.2(d) that there are significant mismatches between the small and finite deforma-

tion models' predictions, but because the small deformation model over predicts the displacements and stresses using the small deformation models would effectively lead to conservative predictions when studying such a simple problem.

To demonstrate where using the small deformation models could be non-conservative we next look at another silicon particle in electrolyte problem, but this time with more interesting geometry and constraints. The problem consists of a cube particle that is anchored to a rigid cylindrical bar which passes through it's center. The problem regions are illustrated on a picture of the finite element mesh in Figure 6.3, and the initial and boundary conditions are listed in Table 6.4.

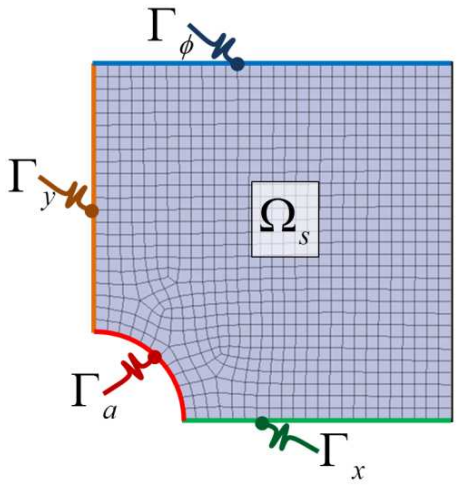

Figure 6.3: Si cube in electrolyte anchored to rod (problem regions on finite element mesh).

Table 6.4: Initial & Boundary Conditions (pseudo two phase cube in electrolyte anchored to rod)

Initial and Boundary Conditions		
$\frac{C_s}{C_{s\,\max}}\Big\vert_{t=0} = 0.01$	in	Ω_s
$\mathbf{u} = \mathbf{0}$	on	Γ_a
$u_y = 0$	on	Γ_x
$u_x = 0$	on	Γ_y
$\phi_s = f(t)$	on	Γ_ϕ
$\frac{C_e}{C_{e\,\max}} = 0.255$	on	Γ_ϕ
$\phi_e = 0.0$	on	Γ_ϕ

As is indicated in Figure 6.3 and Table 6.4 we take advantage of symmetry and only modeled a quarter of the particle. Plane strain-assumptions were used to reduce the problem two dimensions. Pictured below are snapshots of the particle at various times with various field color mapped onto the deformed particle. In the pictures the results are reflected across the symmetry boundaries so the full particle can be viewed.

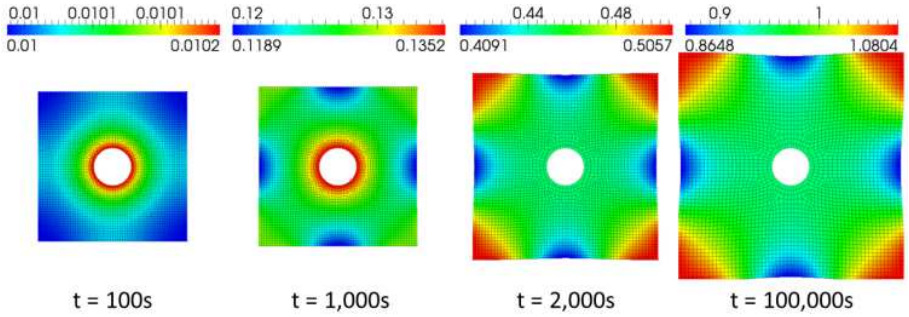

Figure 6.4: Concentration snapshots over time (Small deformation cube anchored to cylinder).

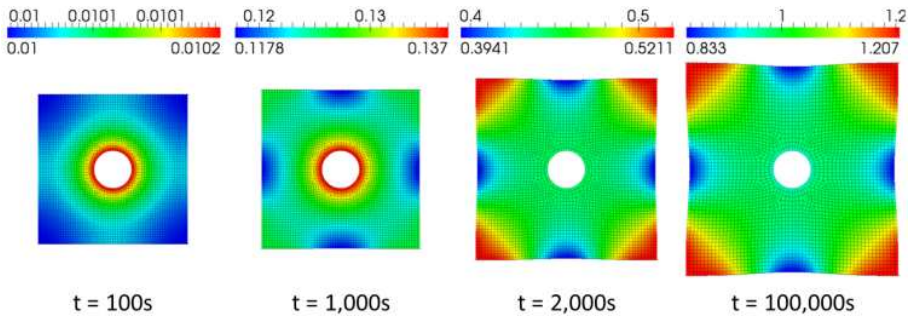

Figure 6.5: Concentration snapshots over time (Finite deformation cube anchored to cylinder).

Starting with a comparing Figures 6.4 and 6.5 it can be observed that both models produce very similar results at early times, when deformation is small, but as time progresses the results slowly step away from each other. At the end of the simulations the range of concentrations predicted by the small deformation model is about 57% of the range predicted by the large deformation model, which will lead to an under-prediction of stresses. The reasons for the deviation are two-fold. First, similar to the previous example, the finite deformation model understands that as the particle swells the transport species has to travel longer distances to diffuse through the particle while the small deformation model has no mechanism accounting for this phenomena. The second reason for the deviation in the concentration state can be attributed to different forms of pressure coupling. Both models use the same hydrostatic pressure coupled chemical potentials, but the pressure terms are computed with different mechanical models. Although the small deformation model in general tends to over predict stresses and thus hydrostatic pressure, it under predicts pressure gradients which drive diffusion. The under prediction of pressure gradients causes an under prediction of pressure coupling which is clear when comparing the concentration fields at the final time step, which is near steady-state.

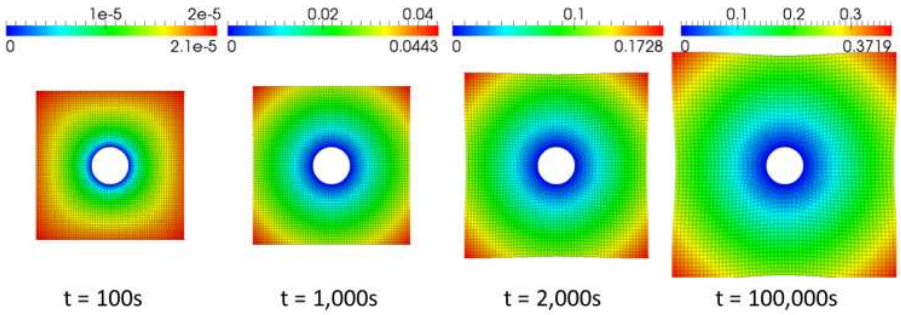

Figure 6.6: Displacement magnitude snapshots over time (Small deformation cube anchored to cylinder).

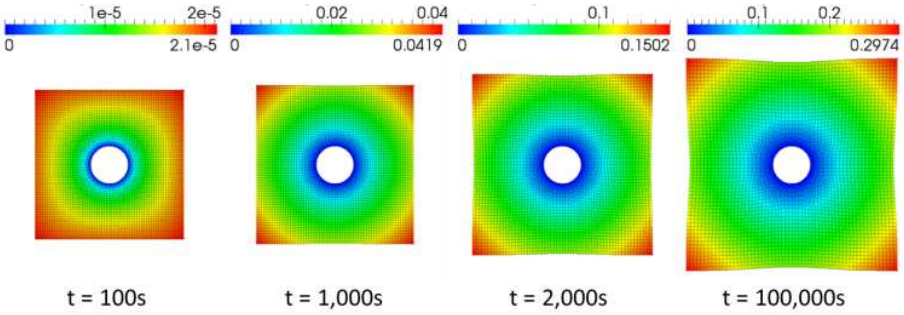

Figure 6.7: Displacement magnitude snapshots over time (Finite deformation cube anchored to cylinder).

Similarly to the previous example problem the displacement responses predicted by small and finite deformation models are very similar at early times when concentrations and swelling are low, but the small deformation model increasingly over predicts the displacement response as swelling increases. Despite the fact that both models predict almost identical surface flux rates and utilization states, the small deformation over predicts the maximum deformation at the end of the simulation by ~25%. This over prediction is significant and on it's own should be motivation enough to switch to a finite deformation model. As the three free state variables used in the models are concentration, displacement, and hydrostatic pressure, hydrostatic pressure plots are shown below to provide a complete picture states predicted by the two models.

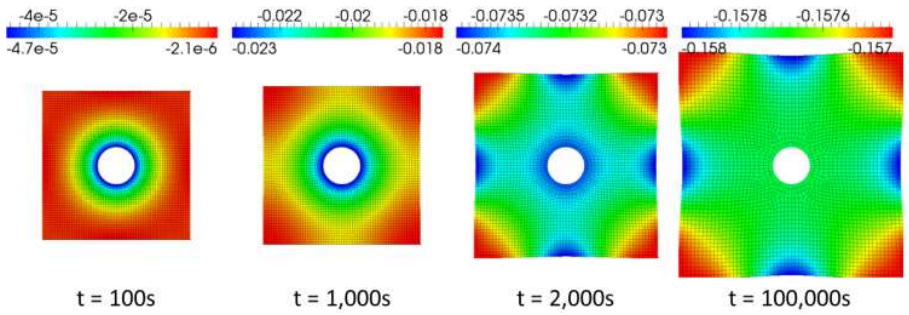

Figure 6.8: Pressure snapshots over time (Small deformation cube anchored to cylinder).

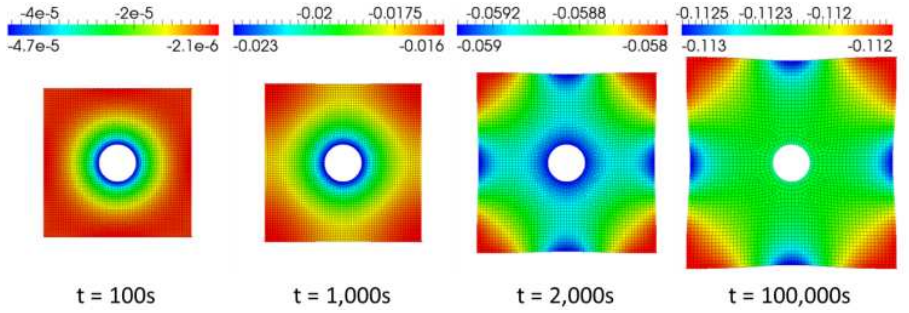

Figure 6.9: Pressure snapshots over time (Finite deformation cube anchored to cylinder).

As was demonstrated in the previous example problem, the small deformation model increasingly over predicts stress magnitudes and thus hydrostatic pressure magnitudes as deformation becomes increasingly significant. This is a trend that can be observed in a wide range mechanics problem involving large deformations, and in general when modeling large deformation mechanics small deformation models can not be counted on to produce accurate predictions. In the current example problem, although the pressure magnitudes predicted by the two models drift away from each other as swelling increases, the pressure distributions are very similar. Therefore, even though the small deformation model should not be counted on to produce accurate predictions, it can be useful in providing insight into the details of the dynamic behavior of intercalation electrodes. Principal stresses are considered next in efforts to find more significant discrepancies in the mechanical predictions of the small and large deformation models.

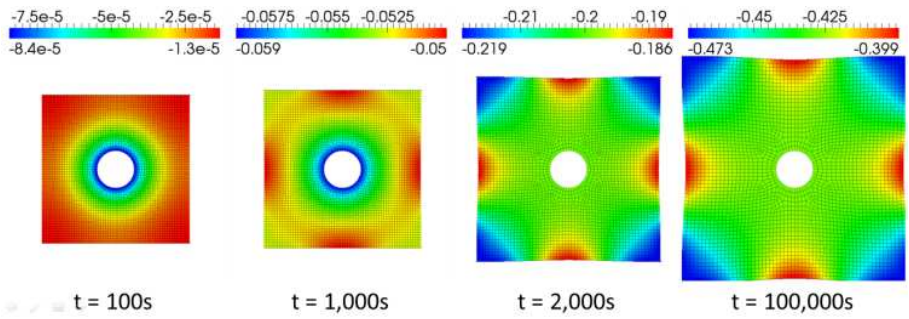

Figure 6.10: 3^{rd} principal stress snapshots over time (Small deformation cube anchored to cylinder).

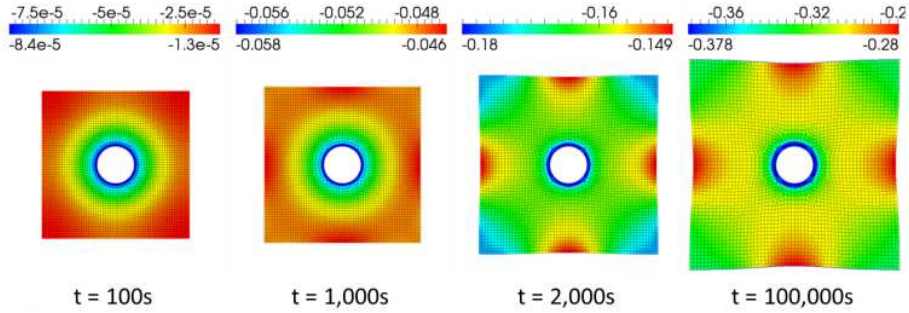

Figure 6.11: 3^{rd} principal stress snapshots over time (Finite deformation cube anchored to cylinder).

The differences in the first two principal stresses predicted by the two models are very similar to the differences in the predicted pressure fields, e.g. magnitude are off but distributions are very similar. However, the third principal stress predictions deviate in magnitude and distribution. This is most clear when comparing the predicted fields on the last time step. The small deformation model predicts that the largest compressive stresses will exist at the corners while the large deformation model predicts that the largest compressive stresses will exist at the center of the particle where it is anchored to a rigid bar. In the example problems we are modeling silicon electrodes. Because silicon is a brittle material it's compressive strength far exceeds it's tensile and shear strength, and it is thus not likely that silicon electrodes will mechanically fail in compression.

Therefore, when considering silicon the mismatches in the third principal stresses are not a major concern. The silicon cube anchored to bar problem demonstrates that even with fairly simple geometries and constraints the small and large deformation models can predict significantly different results. Therefore, when modeling system which undergo significant deformation a proper finite deformation model should be used.

6.2 State of the Art Modeling Capabilities

With all of the tools in place we now have a very powerful tool for studying geometric effects on electrode structures. To demonstrate the utility of the new tools the simulation results of randomly generated micro-structures during voltage controlled lithiation are shown. In the following example problems the particles are grounded and the upper surface of the electrolyte is connected to lithium foil which is swept over the open circuit potential range in 1000s. All of the example problems are run with a 2D plane-strain assumption. Material properties and other simulation parameters used in the following example problems are listed in Table 5.14. Random geometries were created by taking the union of several circles of the phase used to represent silicon who's location and size were determined by a random number generator. Simulation results of the six randomly generated geometries pictured in Figure 6.12 are discussed below.

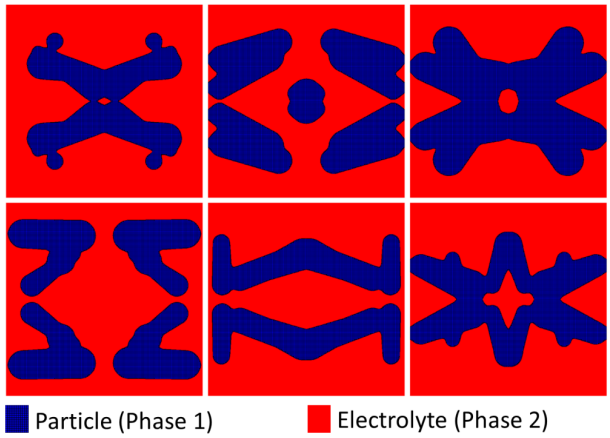

Figure 6.12: Six randomly generated particles in a cube of electrolyte.

Non-dimensional concentration profiles experienced by the first geometry at four snapshots in time are pictured in Figure 6.13.

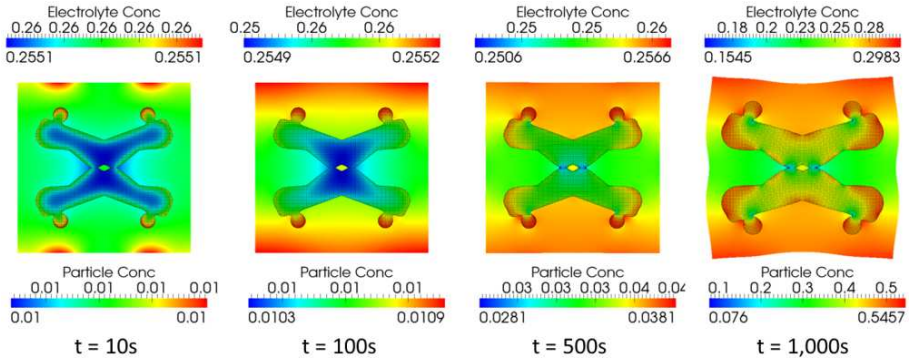

Figure 6.13: Concentration snapshots over time (Random Half-Cell 1).

One of the major shortcomings of previous works was a partial or in come cases a complete lack of mechanical predictive capabilities. As mechanics is one of the major focuses and contributions of the works within, the novel mechanical predictive capabilities are demonstrated below by showing Von-Mises stress predictions at various snapshots in time for various random geometries.

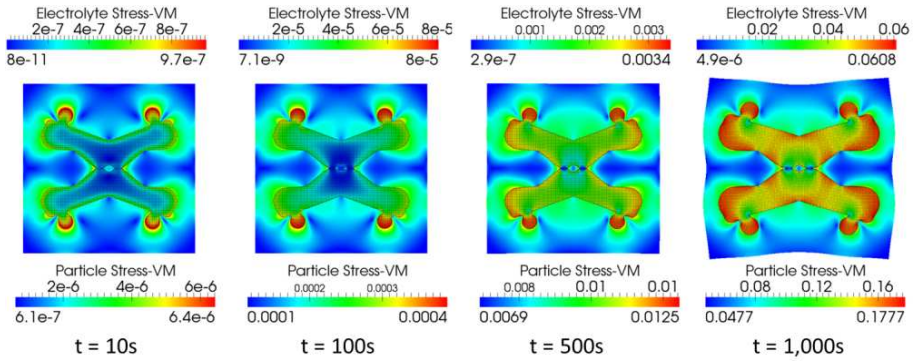

Figure 6.14: Von-Mises stress snapshots over time (Random Half-Cell 1).

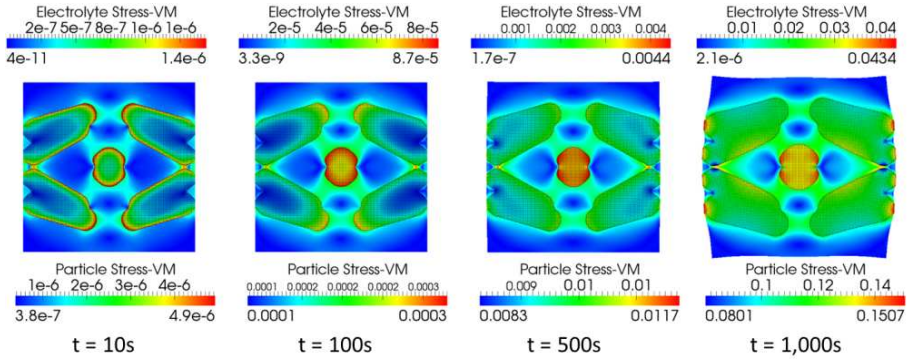

Figure 6.15: Von-Mises stress snapshots over time (Random Half-Cell 2).

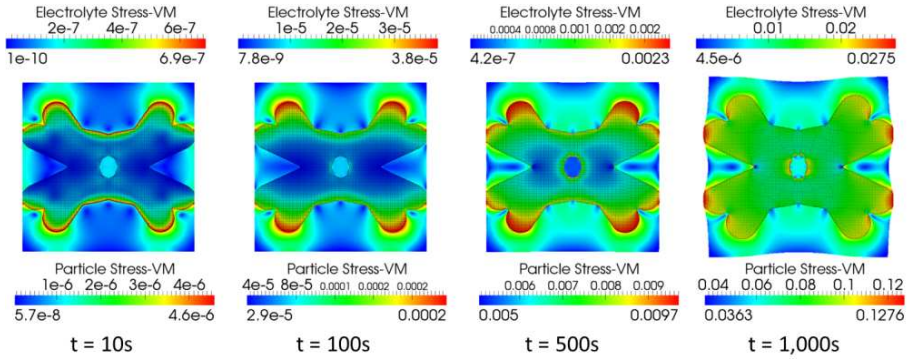

Figure 6.16: Von-Mises stress snapshots over time (Random Half-Cell 3).

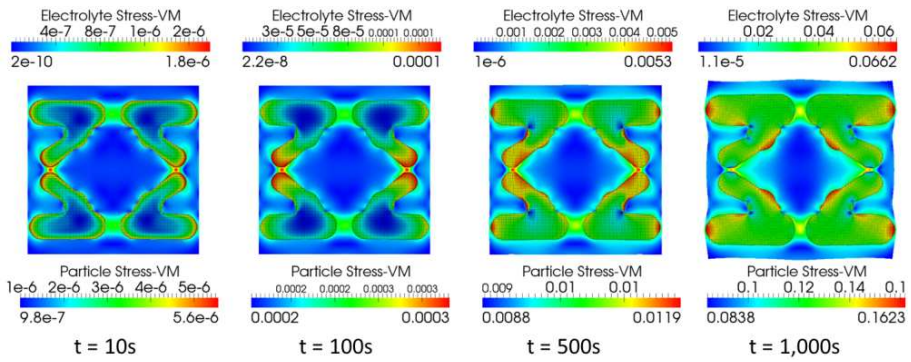

Figure 6.17: Von-Mises stress snapshots over time (Random Half-Cell 4).

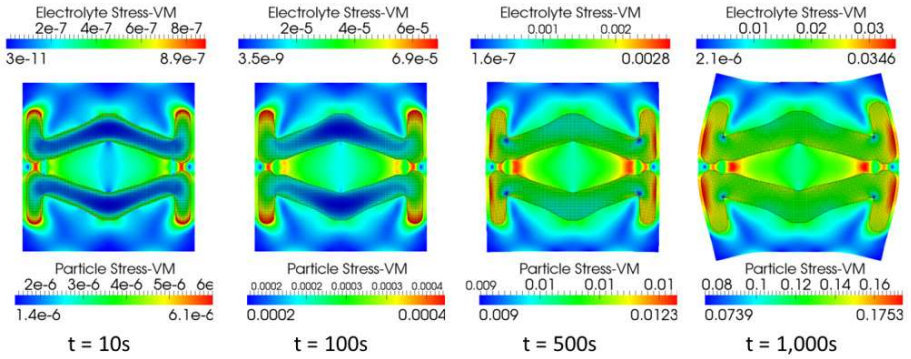

Figure 6.18: Von-Mises stress snapshots over time (Random Half-Cell 5).

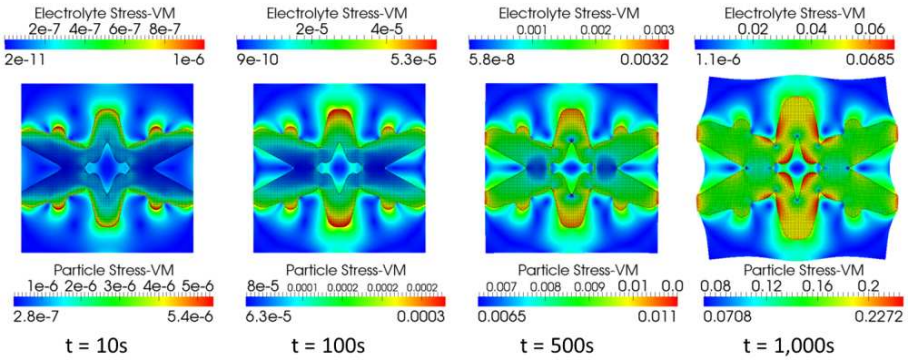

Figure 6.19: Von-Mises stress snapshots over time (Random Half-Cell 6).

With standard meshing tools it would be very difficult to automate the meshing of such complicated shapes. With XFEM, however, all of the shapes can be easily

simulated on a single structured grid. This example demonstrates that XFEM greatly simplifies the use of finite element tools and opens the door for automated geometry studies and topology optimization. In previous studies smooth geometries are simulated. Such simulations provide interesting insight into the coupled mechanics-transport phenomena observed in batteries during operation. However, in most commercial batteries electrodes are agglomerates of electrode host material and a conductive binder impregnated by electrolyte. The electrode particles tend to be somewhat spherical in shape, but they typically have some roughness, corners and edges, which can impact the behavior.

Chapter 7

Future Work And Conclusions

Physical models of some of the primary processes involved in battery operation have been developed including: equilibrium elastic swelling, species transport through electrode particles, electron transport through electrode particles, ion transport through electrolyte, and redox reactions at the electrode particle electrolyte interfaces. This chapter begins with a discussion of some work which could be done in the future to further extend the capabilities and utility of femdoc in Section 7.1. Then in the final Section 7.2 there is discussion of some conclusions that can be drawn from the works presented.

7.1 Future Work

The XFEM implementation of the models described within provide a very powerful tool for studying battery micro-structures. Now that body fitted meshes are no longer needed a single mesh can be used to easily simulate arbitrary electrode geometries. The only things limiting geometries that can be simulated are the grid size and computational power. In our framework the minimum capturable feature size is limited by the size of the elements being used to represent the feature. If there is a desire to model smaller features the mesh grid must be refined, but at the cost of increased computational demand. This cost, however, is common to standard FEM, so we have removed the requirement to have body fitted meshes without adding new limitations.

With such a powerful new numerical experiment/design tool some interesting and novel studies can be performed. For example, level-set fields can be generated from pictures or a CAT scan. This could be an invaluable tool in developing and performing new validation studies, as it allows one to model actual observed geometries instead of idealized geometries. As validation is the major missing piece of the model development documented within, developing and performing validation studies would add great value to the developed models in the form of credibility as well as help advance the battery modeling community by providing new studies that could be used to validate future models.

In topology optimization a material distribution is sought which optimizes some performance criteria while satisfying constraints. The finite element modeling framework has been written with optimization in mind. We have many physical system representations in our framework, but only a few are currently correctly setup to work with our XFEM topology optimization framework. To facilitate reliably using XFEM in the optimization framework a system must continue to be solvable as the optimizer evolves the phase distributions. Unfortunately, it is easy to create phase distributions which result in un-solvable systems when using the current XFEM cell micro-structure framework. XFEM specific pre-conditioners have been implemented to help correct linear system ill conditioning caused narrowly intersecting elements. The pre-conditioners have been demonstrated to be effective on other physical systems implemented in the XFEM framework, but unfortunately seem to have little to no influence on the un-solvable cell micro-structure problems. If the XFEM cell micro-structure framework can be made to reliably solve as phase distributions evolve we will have a very powerful tool to help guide the development new micro-structured cell designs.

State of the art fully coupled species/ion transport-finite deformation elasticity models have been implemented in a FEM/XFEM framework to facilitate numerical studies for both scientific and design purposes. The implemented modeling capabilities

represent an advancement in the battery modeling community, but there are a number of physical phenomena associated with battery operation that have been ignored. Of the ignored phenomena there are a several which involve discrete moving interfaces including: fracture mechanics, solid-electrolyte interface layer (SEI) growth, dendrite growth, and multi-phase diffusion. These phenomena pose significant challenges to people using traditional FEM techniques. A commonly used techniques for modeling discrete moving interfaces with traditional finite elements use an arbitrary Lagrangian-Eulerian (ALE) representation of interfaces. ALE techniques represent moving interfaces as movements of an interface in a body fitted mesh. Moving an interface in a body fitted mesh results in distorted elements, and if elements are distorted to the point of having large aspect ratios they will likely produce very inaccurate predictions. Moving interfaces in body fitted meshes can also lead to inverted elements.

Techniques have been developed to mitigate the shortcomings of ALE techniques, including using extra non-physical state variables to minimize element distortion over the whole mesh and adaptive re-meshing. Both solutions, however, add significant computational overhead and in the second case programmatic complexity. Furthermore, both solutions are limited in their abilities represent significant geometric changes. Where traditional FEM falls short in it's ability to represent arbitrary geometries XFEM shows much promise. XFEM was originally developed for modeling crack propagation [21, 48, 47], but the same framework has since been used for modeling other moving interface phenomena such as a bubble moving through water [14]. Our XFEM implementation currently only involves one static levelset field. Extending our framework to model any of the neglected moving interface phenomena would require the addition of a second levelset field and both levelset fields must be made dynamic. Adding such capabilities would take a significant amount of work, but would greatly increase the predictive capabilities and utility of femdoc.

7.2 Conclusions

Accurate modeling of complicated physical phenomena associated with battery operation requires a detailed understanding mechanisms involved. Via research several of the physical mechanisms involved in battery operation have been identified. The majority of the work within was motivated by desire to develop techniques for using silicon as an anode host material in lithium ion batteries. The major challenges of using silicon as an anode material are associated with the significant volume change caused by lithiation; we have chosen to focus on modeling highly coupled transport and mechanics. As mechanics is a vast field and the mechanics associated with silicon lithiation involves many areas of the field, we further narrowed the focus to highly coupled transport and equilibrium elasticity. Several of the physical mechanisms involved in battery operation have been ignored including: plasticity, fracture mechanics, multi-phase diffusion, solid electrolyte interface layer (SEI) growth, dendrite growth, thermal degradation. As discussed in the previous section our XFEM framework gives an very flexible tool for modeling discrete arbitrary interfaces, which, as an extension of the works within, could be adapted for modeling some of the neglected phenomena that involve moving interfaces.

Mathematical models of coupled "species/ion transport-elastic mechanics" and "host material-electrolyte" interface kinetics have been implemented in a finite element framework with XFEM extensions. The models were thoroughly verified against numerous analytical solutions and published results of other similar numerical models, but there is a glaring lack of model validation. This was due to a lack of published experimental works that adequately demonstrate the phenomena of interest. To add value to the models in the form of credibility a future researcher could work with an experimentalist to develop validation studies.

As many authors only consider linear elasticity, it has been demonstrated that

they are cases in which linear elasticity provides adequate results, but when modeling systems which undergo ∼100% volume change linear elasticity can't be counted on to adequately predict the behavior. Meshing is one of the major challenges of using traditional FEM for modeling complex or varied geometries, so various examples were used demonstrate how our XFEM framework mitigates those challenges. Host material lithiation behavior can be very sensitive to geometry changes, so the author believes that the XFEM capabilities add great utility for researchers interested in finding "optimal" geometries. The works documented within advance the battery community by providing novel modeling capabilities, as well as a clean formalism that can aid in the development future modeling capabilities. It is hoped that the developed tools will enable future researchers gain a deeper insight into physical phenomena and to develop next generation battery technologies.

Bibliography

[1] Abaqus, inc. theory reference. Ansys, Inc. 2004.

[2] Ansys, inc. theory reference. Ansys, Inc. 2004.

[3] Ansys, inc. verification manual for the mechanical apdl application. Ansys, Inc. 2009.

[4] Loic Baggetto, Rogier A. H. Niessen, Fred Roozeboom, and Peter H. L. Notten. High energy density all-solid-state batteries: A challenging concept towards 3d integration. Adv. Funct. Mater., 18:10571066, 2008.

[5] Allen J. Bard and Larry R. Faulkner. Electrochemical Methods. John Wiley and Sons, Inc, 2 edition, 2001.

[6] Klaus-Jurgen Bathe. Finite element procedures. Prentice Hall, 1996.

[7] T. Belytschko and T. Black. Elastic crack growth in finite elements with minimal remeshing. International Journal for Numerical Methods in Engineering, 45(5):601–620, 1999.

[8] Ted Belytschko, Wing K. Liu, and Brian Moran. Nonlinear Finite Elements for Continua and Structures. John Wiley and Sons Ltd., 2000.

[9] A.F. Bower, P.R. Guduru, and V.A. Sethuraman. A finite strain model of stress, diffusion, plastic flow, and electrochemical reactions in a lithium-ion half-cell. Journal of the Mechanics and Physics of Solids, 59(4):804–828, 2011.

[10] Candace K. Chan, Hailin Peng, Gao Liu, Kevin McIlwrath, Xiao Feng Zhang, Robert A. Huggins, and Yi Cui. High-performance lithium battery anodes using silicon nanowires. Nat Nano, 3:31–35, 2008.

[11] Y. T. Cheng and Mark W. Verbrugge. The influence of surface mechanics on diffusion induced stresses within spherical nanoparticles. Journal of Applied Physics, 104(8):083521, 2008.

[12] Y. T. Cheng and Mark W. Verbrugge. Diffusion-induced stress, interfacial charge transfer, and criteria for avoiding crack initiation of electrode particles. Journal of The Electrochemical Society, 157(4):A508–A516, 2010.

[13] Yang-Tse Cheng and Mark W. Verbrugge. Evolution of stress within a spherical insertion electrode particle under potentiostatic and galvanostatic operation. Journal of Power Sources, 190(2):453–460, 2009.

[14] J. Chessa and T. Belytschko. An extended finite element method for two-phase fluids. Journal of Applied Mechanics, 70(1):10–17, 2003.

[15] Shawn A. Chester and Lallit Anand. A coupled theory of fluid permeation and large deformations for elastomeric materials. Journal of the Mechanics and Physics of Solids, 58(11):1879 – 1906, 2010.

[16] Shawn A. Chester and Lallit Anand. A thermo-mechanically coupled theory for fluid permeation in elastomeric materials: Application to thermally responsive gels. Journal of the Mechanics and Physics of Solids, 59(10):1978 – 2006, 2011.

[17] John Christensen and John Newman. A mathematical model of stress generation and fracture in lithium manganese oxide. Journal of the Electrochemical Society, 153(6):1019–1030, 2006.

[18] John Christensen and John Newman. Stress generation and fracture in lithium insertion materials. Journal of Solid State Electrochemistry, 10(5):293–319, 2006.

[19] D. Danilov, R. A. H. Niessen, and P. H. L. Notten. Modeling all-solid-state li-ion batteries. Journal of The Electrochemical Society, 158(3):A215–A222, 2011.

[20] D. Danilov and P.H.L. Notten. Mathematical modelling of ionic transport in the electrolyte of li-ion batteries. Electrochimica Acta, 53(17):5569 – 5578, 2008.

[21] Christophe Daux, Nicolas Mos, John Dolbow, Natarajan Sukumar, and Ted Belytschko. Arbitrary branched and intersecting cracks with the extended finite element method. International Journal for Numerical Methods in Engineering, 48(12):1741–1760, 2000.

[22] Christopher M. DeLuca, Kurt Maute, and Martin L. Dunn. Effects of electrode particle morphology on stress generation in silicon during lithium insertion. Journal of Power Sources, 196(22):9672–9681, 2011.

[23] Rutooj Deshpande, Yang-Tse Cheng, and Mark W. Verbrugge. Modeling diffusion-induced stress in nanowire electrode structures. Journal of Power Sources, 195(15):5081–5088, 2010.

[24] Marc Doyle. Design and Simulation of Lithium Rechargeable Batteries. PhD thesis, University of California, Berkeley, 1995.

[25] A. Gerstenberger and W. A. Wall. An embedded dirichlet formulation for 3d continua. International Journal for Numerical Methods in Engineering, 82(5):537–563, 2010.

[26] Axel Gerstenberger and Wolfgang A. Wall. Enhancement of fixed-grid methods towards complex fluidstructure interaction applications. International Journal for Numerical Methods in Fluids, 57(9):1227–1248, 2008.

[27] Stephanie Golmon, Kurt Maute, and Martin L. Dunn. Numerical modeling of electrochemical-mechanical interactions in lithium polymer batteries. Computers & Structures, 87(23-24):1567–1579, 2009.

[28] Stephanie Golmon, Kurt Maute, and Martin L. Dunn. Multiscale design optimization of lithium ion batteries using adjoint sensitivity analysis. International Journal for Numerical Methods in Engineering, 92(5):475–494, 2012.

[29] Stephanie Golmon, Kurt Maute, Se-Hee Lee, and Martin L. Dunn. Stress generation in silicon particles during lithium insertion. Applied Physics Letters, 97(3), 2010.

[30] Morton E. Gurtin, Eliot Fried, and Anand Lallit. The Mechanics and Thermodynamics of Continua. Cambridge University Press, 2010.

[31] Morton E. Gurtin and Ian A. Murdoch. A continuum theory of elastic material surfaces. Archive for Rational Mechanics and Analysis, 57:291–323, 1975. 10.1007/BF00261375.

[32] Hamed Haftbaradaran, Jun Song, W.A. Curtin, and Huajian Gao. Continuum and atomistic models of strongly coupled diffusion, stress, and solute concentration. Journal of Power Sources, 196(1):361 – 370, 2011.

[33] Gerhard A. Holzapfel. Nonlinear Solid Mechanics: a continuum approach for engineering. John Wiley and Sons Ltd., 2000.

[34] Wei Hong, Xuanhe Zhao, Jinxiong Zhou, and Zhigang Suo. A theory of coupled diffusion and large deformation in polymeric gels. Journal of the Mechanics and Physics of Solids, 56(5):1779 – 1793, 2008.

[35] Hyunjung Kim, Byunghee Han, Jaebum Choo, and Jaephil Cho. Three-dimensional porous silicon particles for use in high-performance lithium secondary batteries. J. Angew. Chem., Int. Ed., 47:10151–10154, 2008.

[36] Dave Makhija and Kurt Maute. Numerical instabilities in level set topology optimization with the extended finite element method. Structural and Multidisciplinary Optimization, submitted.

[37] Matthew T. McDowell, Seok Woo Lee, Ill Ryu, Hui Wu, William D. Nix, Jang Wook Choi, and Yi Cui. Novel size and surface oxide effects in silicon nanowires as lithium battery anodes. Nano Letters, 0(0), 2011.

[38] Ronald E Miller and Vijay B Shenoy. Size-dependent elastic properties of nanosized structural elements. Nanotechnology, 11(3):139–147, 2000.

[39] Nicolas Mos, John Dolbow, and Ted Belytschko. A finite element method for crack growth without remeshing. International Journal for Numerical Methods in Engineering, 46(1):131–150, 1999.

[40] John Newman and Karen E. Thomas. Electrochemical Systems. Wiley-Interscience, 3 edition, 2004.

[41] F. Orsini, A. Du Pasquier, B. Beaudoin, J.M. Tarascon, M. Trentin, N. Langenhuizen, E. De Beer, and P. Notten. In situ scanning electron microscopy (sem) observation of interfaces within plastic lithium batteries. Journal of Power Sources, 76(1):19 – 29, 1998.

[42] A. Ricci and C. Ricciardi. A new finite element approach for studying the effect of surface stress on microstructures. Sensors and Actuators A: Physical, 159(2):141–148, 2010.

[43] C. Ru. Simple geometrical explanation of gurtin-murdoch model of surface elasticity with clarification of its related versions. SCIENCE CHINA Physics, Mechanics & Astronomy, 53:536–544, 2010. 10.1007/s11433-010-0144-8.

[44] H. Sauerland and T.-P. Fries. The extended finite element method for two-phase and free-surface flows: A systematic study. Journal of Computational Physics, 230(9):3369 – 3390, 2011.

[45] P. Sharma, S. Ganti, and N. Bhate. Effect of surfaces on the size-dependent elastic state of nano-inhomogeneities. Applied Physics Letters, 82(4):535–537, 2003.

[46] Taeseup Song, Jianliang Xia, Jin-Hyon Lee, Dong Hyun Lee, Moon-Seok Kwon, Jae-Man Choi, Jian Wu, Seok Kwang Doo, Hyuk Chang, Won Il Park, Dong Sik Zang, Hansu Kim, Yonggang Huang, Keh-Chih Hwang, John A. Rogers, and Ungyu Paik. Arrays of sealed silicon nanotubes as anodes for lithium ion batteries. Nano Letters, 10(5):1710–1716, 2010.

[47] M. Stolarska, D. L. Chopp, N. Mos, and T. Belytschko. Modelling crack growth by level sets in the extended finite element method. International Journal for Numerical Methods in Engineering, 51(8):943–960, 2001.

[48] N. Sukumar, N. Mos, B. Moran, and T. Belytschko. Extended finite element method for three-dimensional crack modelling. International Journal for Numerical Methods in Engineering, 48(11):1549–1570, 2000.

[49] Zhigang Suo, Xuanhe Zhao, and William H. Greene. A nonlinear field theory of deformable dielectrics. Journal of the Mechanics and Physics of Solids, 56(2):467–486, 2008.

[50] J. Svoboda and F.D. Fischer. Vacancy-driven stress relaxation in layers. Acta Materialia, 57(16):4649–4657, 2009.

[51] Laurent Van Miegroet and Pierre Duysinx. Stress concentration minimization of 2d filets using x-fem and level set description. Structural and Multidisciplinary Optimization, 33:425–438, 2007. 10.1007/s00158-006-0091-1.

[52] Peng Wei, Michael Yu Wang, and Xianghua Xing. A study on x-fem in continuum structural optimization using a level set model. Computer-Aided Design, 42(8):708 – 719, 2010. ¡ce:title¿Application-driven Shape Development¡/ce:title¿.

[53] X. Xiao, P. Liu, M.W. Verbrugge, H. Haftbaradaran, and H. Gao. Improved cycling stability of silicon thin film electrodes through patterning for high energy density lithium batteries. Journal of Power Sources, 196(3):1409–1416, 2011.

[54] Zohar Yosibash, Stefan Hartmann, Ulrich Heisserer, Alexander Dster, Ernst Rank, and Mordechai Szanto. Axisymmetric pressure boundary loading for finite deformation analysis using p-fem. Computer Methods in Applied Mechanics and Engineering, 196(7):1261 – 1277, 2007.

[55] Vahur Zadin and Daniel Brandell. Modelling polymer electrolytes for 3d-microbatteries using finite element analysis. Electrochimica Acta, (0):–, 2011.

[56] Vahur Zadin, Daniel Brandell, Heiki Kasemgi, Alvo Aabloo, and John O. Thomas. Finite element modelling of ion transport in the electrolyte of a 3d-microbattery. Solid State Ionics, 192(1):279 – 283, 2011. ¡ce:title¿Proceedings of the 17th International Conference on Solid State Ionics¡/ce:title¿.

[57] Vahur Zadin, Heiki Kasemgi, Alvo Aabloo, and Daniel Brandell. Modelling electrode material utilization in the trench model 3d-microbattery by finite element analysis. Journal of Power Sources, 195(18):6218 – 6224, 2010. ¡ce:title¿Selected Papers Presented at 4th International Conference on Polymer Batteries and Fuel Cells¡/ce:title¿.

[58] Jiaping Zhang, Xuanhe Zhao, Zhigang Suo, and Hanqing Jiang. A finite element method for transient analysis of concurrent large deformation and mass transport in gels. Journal of Applied Physics, 105(9):093522 –093522–9, may 2009.

[59] Xiangchun Zhang, Ann Marie Sastry, and Wei Shyy. Intercalation-induced stress and heat generation within single lithium-ion battery cathode particles. Journal of the Electrochemical Society, 155(7):542–52, 2008.

[60] Xiangchun Zhang, Wei Shyy, and Ann Marie Sastry. Numerical simulation of intercalation-induced stress in li-ion battery electrode particles. Journal of the Electrochemical Society, 154(10):910–916, 2007.

[61] Kejie Zhao, Matt Pharr, Shengqiang Cai, Joost J. Vlassak, and Zhigang Suo. Large plastic deformation in high-capacity lithium-ion batteries caused by charge and discharge. Journal of the American Ceramic Society, 94:s226–s235, 2011.

Chapter 8

Appendix

8.1 Appendix A: Transformation Rules

Table 8.1: Stress Transformation Rules

	$\boldsymbol{\sigma}$	$\mathbf{P}$	$\mathbf{S}$	$\mathbf{P}^e$	$\mathbf{S}^e$
$\boldsymbol{\sigma}$	$\boldsymbol{\sigma}$	$J^{-1}\mathbf{P}\mathbf{F}^T$	$J^{-1}\mathbf{F}\mathbf{S}\mathbf{F}^T$	$J^{-e}\mathbf{P}^e\mathbf{F}^{eT}$	$J^{-e}\mathbf{F}^e\mathbf{S}^e\mathbf{F}^{eT}$
$\mathbf{P}$	$J\boldsymbol{\sigma}\mathbf{F}^{-T}$	$\mathbf{P}$	$\mathbf{F}\mathbf{S}$	$J^C\mathbf{P}^e\mathbf{F}^{-CT}$	$J^C\mathbf{F}^e\mathbf{S}^e\mathbf{F}^{-CT}$
$\mathbf{S}$	$J\mathbf{F}^{-1}\boldsymbol{\sigma}\mathbf{F}^{-T}$	$\mathbf{F}^{-1}\mathbf{P}$	$\mathbf{S}$	$J^C\mathbf{F}^{-1}\mathbf{P}^e\mathbf{F}^{-CT}$	$J^C\mathbf{F}^{-C}\mathbf{P}^e\mathbf{F}^{-CT}$
$\mathbf{P}^e$	$J^e\boldsymbol{\sigma}\mathbf{F}^{-eT}$	$J^{-C}\mathbf{P}\mathbf{F}^{CT}$	$J^{-C}\mathbf{F}\mathbf{S}\mathbf{F}^{CT}$	$\mathbf{P}^e$	$\mathbf{F}^e\mathbf{S}^e$
$\mathbf{S}^e$	$J^e\mathbf{F}^{-e}\boldsymbol{\sigma}\mathbf{F}^{-eT}$	$J^{-C}\mathbf{F}^{-e}\mathbf{P}\mathbf{F}^{CT}$	$J^{-C}\mathbf{F}^C\mathbf{S}\mathbf{F}^{CT}$	$\mathbf{F}^{-e}\mathbf{P}^e$	$\mathbf{S}^e$

Table 8.2: Other Transformation Rules

$\nabla^0 = \mathbf{F}^T\nabla$
$C = \det(\mathbf{F})\, c$
$\mathbf{J} = \det(\mathbf{F})\, \mathbf{F}^{-1}\mathbf{j}$

8.2 Appendix B: Nonlinear Elastic Models

The Saint-Venant Kirchhoff model [8, 33]

$$\Psi(E_{ij}) = \mu_0 (E_{ij}E_{ji}) + \frac{\lambda_0}{2}(E_{ii})^2 \tag{8.1}$$

$$\Psi\left(C_{ij}\right)=\frac{\mu_0}{4}\left(C_{ij}C_{ji}-2C_{ii}+3\right)+\frac{\lambda_0}{8}(C_{ii}-3)^2 \tag{8.2}$$

$$S_{ij}=2\mu_0 E_{ij}+\lambda_0 E_{kk}\delta_{ij} \tag{8.3}$$

$$S_{ij}=\mu_0\left(C_{ij}-\delta_{ij}\right)+\frac{\lambda_0}{2}\left(C_{kk}-3\right)\delta_{ij} \tag{8.4}$$

The Neo-Hookean material model of Belytchko et al. [8]

$$\Psi=\tfrac{\mu_0}{2}\left(I_1-3\right)-\mu_0\ln\left(J\right)+\tfrac{1}{2}\lambda_0\ln\left(J\right)^2 \tag{8.5}$$

$$\Rightarrow S_{ij}=\mu_0\delta_{ij}+\left(-\mu_0+\lambda_0\cdot\ln\left(J\right)\right)C_{ij}^{-1} \tag{8.6}$$

The Neo-Hookean material model of ANSYS [2]

$$\Psi=\tfrac{\mu_0}{2}\left(\bar{I}_1-3\right)+\tfrac{\kappa_0}{2}(J-1)^2 \tag{8.7}$$

$$\Rightarrow S_{ij}=\mu_0 J^{-2/3}\delta_{ij}+\left(-\tfrac{\mu_0}{3}I_1J^{-2/3}+\kappa_0\left(J^2-J\right)\right)C_{ij}^{-1} \tag{8.8}$$

The Mooney-Rivlin material model [6, 1]

$$\Psi=C_1\left(\bar{I}_1-3\right)+C_2\left(\bar{I}_2-3\right)+\tfrac{\kappa_0}{2}(J-1)^2 \tag{8.9}$$

$$\Rightarrow S_{ij}=2\left[\begin{array}{l}\left(C_1J^{-2/3}+C_2I_1J^{-4/3}\right)\delta_{ij}-C_2J^{-4/3}C_{ij}+\\ \left(\tfrac{-1}{3}\left(C_1I_1J^{-2/3}+2C_2I_2J^{-4/3}\right)+\tfrac{\kappa_0}{2}\left(J^2-J\right)\right)C_{ij}^{-1}\end{array}\right] \tag{8.10}$$

where

$$\mu_0=2\left(C_1+C_2\right) \tag{8.11}$$

The Arruda-Boyce material model [2]

$$\Psi=\mu_0\sum_{i=1}^{5}\frac{C_i}{\lambda_m^{2i-2}}\left(\bar{I}_1^i-3^i\right)+\tfrac{\kappa_0}{2}\left(\frac{J^2-1}{2}-\ln\left(J\right)\right) \tag{8.12}$$

$$\Rightarrow S_{ij}=\gamma J^{-2/3}\delta_{ij}+\left(\tfrac{-1}{3}\gamma I_1J^{-2/3}+\tfrac{\kappa_0}{2}\left(J^2-1\right)\right)C_{ij}^{-1} \tag{8.13}$$

where

$$\gamma=2\mu_0\sum_{i=1}^{5}\frac{iC_i}{\lambda_m^{2i-2}}\bar{I}_1^{i-1} \tag{8.14}$$

and

$$C_i=\left[\begin{array}{ccccc}\frac{1}{2} & \frac{1}{20} & \frac{11}{1050} & \frac{19}{7000} & \frac{519}{637350}\end{array}\right] \tag{8.15}$$

The Gent material model [2]

$$\Psi = \frac{-\mu_0}{2} J_m \ln\left(1 - \frac{\bar{I}_1 - 3}{J_m}\right) + \frac{\kappa_0}{2}\left(\frac{J^2 - 1}{2} - \ln(J)\right) \tag{8.16}$$

$$\Rightarrow S_{ij} = \gamma J^{-2/3}\delta_{ij} + \left(\frac{-1}{3}\gamma I_1 J^{-2/3} + \frac{\kappa_0}{2}\left(J^2 - 1\right)\right) C_{ij}^{-1} \tag{8.17}$$

where

$$\gamma = \frac{\mu_0 J_m}{J_m + 3 - \bar{I}_1} \tag{8.18}$$

8.3 Appendix C: Chemical Potential Functions

Simple Uncoupled Chemical Potential

$$\mu_c = \mu_{c0} + R_g T \ln(c) \tag{8.19}$$

Simple Stress Coupled Chemical Potential

$$\mu_c = \mu_{c0} + R_g T \ln(c) - \Omega \sigma_h \tag{8.20}$$

Haftbaradaran Stress Coupled Chemical Potential [32]

$$\mu_c = \mu_{c0} + R_g T \ln\left(\frac{c/c_{\max}}{1 + c/c_{\max}}\right) - \Omega \sigma_h + R_g T \ln\left(\frac{\gamma_s}{\gamma_v}\right) \tag{8.21}$$

Flory-Huggins Incompressible Stress Coupled Chemical Potential [34]

$$\mu = R_g T \left[\ln\left(\frac{\Omega C}{1 + \Omega C}\right) + \frac{1}{1 + \Omega C} + \frac{\chi}{(1 + \Omega C)^2}\right] - \Omega p_o \tag{8.22}$$

8.4 Appendix D: Symbols

Table 8.3: Material Properties and Constants

Symbol	Typical Units	Description
$\underline{\mathbf{C}}$	Pa	4th order elasticity tensor
E	Pa	Young's modulus
λ_0	Pa	Lamé's first parameter
μ_0	Pa	Shear modulus
λ_{mab}	-	Arruda-Boyce stretch limiting parameter
λ_{mg}	-	Gent stretch limiting parameter
$\tau_{\mathbf{0}}$	N/m	Initial surface stress tensor
$\mathbf{K^s}$	N/m	4th order surface elasticity tensor
τ_0	N/m	Initial surface stress constant (sphere-symmetric)
κ^s	N/m	Surface elasticity constant (sphere-symmetric)
$\boldsymbol{\omega}$	m^3/mol	2^{nd} order stretch constitutive tensor
ω	m^3/mol	Isotropic stretch coefficient
Ω	m^3/mol	Partial molar volume
D	m^2/s	Diffusion coefficient
c_{max}	mol/m^3	Maximum concentration
k^s	$m^{2.5}/\left(mol^{0.5}s\right)$	Surface reaction rate
z	-	Ion valence number
k	S/m	Electrical conductivity
T	K	Absolute temperature
R_g	$J/\left(Kmol\right)$	Ideal gas constant
μ_{c0}	J/mol	Initial chemical/electrochemical potential
F	C/mol	Faraday's constant

$\alpha_a \& \alpha_c$	-	Transfer coefficients

Table 8.4: Variables

Symbol	Typical Units	Description
t	s	Time
$\mathbf{x}$	m	Coordinate vector
$\mathbf{X}$	m	Material coordinate vector
$\mathbf{n}$	-	Surface normal vector
$\mathbf{n}_0$	-	Material surface normal vector
$\mathbf{u}$	m	Displacement vector
$\mathbf{v}$	m	Velocity vector
∇	1/m	Gradient operator
∇^0	1/m	Material gradient operator
$\mathbf{H}$	-	Displacement gradient tensor
$\mathbf{F}$	-	Deformation gradient tensor
$\mathbf{F}^C$	-	Species/Ion swelling deformation gradient tensor
$\mathbf{F}^e$	-	Elastic deformation gradient tensor
J	-	Deformation gradient determinant
J^C	-	Species/Ion swelling deformation gradient determinant
J^e	-	Elastic deformation gradient determinant
$\mathbf{C}$	-	Right Cauchy-Green deformation tensor
$\mathbf{C}^e$	-	Elastic right Cauchy-Green deformation tensor
$\boldsymbol{\sigma}$	Pa	Cauchy stress tensor
σ_h	Pa	Hydrostatic stress
p_i	Pa	Indeterminant pressure
$\mathbf{P}$	Pa	Nominal stress tensor

$\mathbf{P}^e$	Pa	Elastic nominal stress tensor
$\mathbf{S}$	Pa	PK2 stress tensor
$\mathbf{S}^e$	Pa	Elastic PK2 stress tensor
c	mol/m^3	Species/Ion concentration
C	mol/m^3	Nominal species/ion concentration
$\mathbf{j}$	$mol/m^2/s$	Species/Ion flux
$\mathbf{J}$	$mol/m^2/s$	Species/Ion nominal flux
μ_c	J/mol	Chemical/Electrochemical potential
ϕ	V	Electric potential
$\mathbf{i}$	V/m	Electric field vector
$\mathbf{I}$	V/m	Nominal electric field vector